

APPLICATIONS OF THE OPTO-FLUIDIC RING RESONATOR FOR  
DNA METHYLATION ANALYSIS AND MICROFLUIDIC LASER  
DEVELOPMENT

---

A Thesis presented to the Faculty of the Graduate School  
University of Missouri

---

In Partial Fulfillment  
Of the Requirements for the Degree

Doctor of Philosophy

---

by

JONATHAN DANIEL SUTER

Dr. Xudong Fan, Thesis Supervisor

DECEMBER 2010

The undersigned, appointed by the Dean of the Graduate School, have examined the dissertation entitled

APPLICATIONS OF THE OPTO-FLUIDIC RING RESONATOR FOR DNA  
METHYLATION ANALYSIS AND MICROFLUIDIC LASER DEVELOPMENT

Presented by Jonathan Daniel Suter

A candidate for the degree of Doctor of Philosophy

And hereby certify that in their opinion it is worthy of acceptance.

---

Xudong Fan, Ph.D., Department of Biological Engineering

---

John A. Viator, Ph.D., Department of Biological Engineering

---

Sheila A. Grant, Ph.D., Department of Biological Engineering

---

Huidong Shi, Ph.D., Department of Pathology and Anatomical Science

## ACKNOWLEDGMENTS

I gratefully acknowledge the guidance of my principle advisor, Dr. Xudong (Sherman) Fan, whose high standards of excellence have shaped every professional asset that I possess today. His drive and vision have taught me to always expect more from myself.

I also must acknowledge the support provided by the NIH Biodetectives Training Grant, which gave me a measure of financial security during my doctoral research.

The work described herein could never have been completed without the expertise of Drs. Charles Caldwell and Huidong Shi, who advised us on the DNA methylation project, and Dr. Ian White, who helped us with the microfabrication of our dye lasers.

I also appreciate the efforts of my doctoral committee – Drs. Huidong Shi, Sheila Grant and John Viator – all of whom have given me useful advice over these past five years and have been miraculously generous with their schedules.

I would like to thank all of my fellow students who have worked with me in Dr. Fan's lab, both in the University of Missouri and the University of Michigan: Dr. Hongying Zhu, Daniel Howard, Hesam Oveys, Jay Cupps, Yuze Sun, Chung-Sheih Wu, John Gohring, Jing Liu, Dr. Maung Kyaw Khaing Oo, Dr. Yunbo Guo, Wonsuk Lee, Hao Li, Karthik Reddy, and Chia Chang.

On a personal note, I would like to thank my parents, Michael and Cheryl Suter, and my wife Kristin, who have supported me financially and psychologically every step of the way.

# TABLE OF CONTENTS

ACKNOWLEDGMENTS .....	ii
LIST OF FIGURES .....	vii
LIST OF TABLES .....	xiii
LIST OF ABBREVIATIONS.....	xiv
ABSTRACT.....	xvi
Chapter	
1. INTRODUCTION TO RING RESONATOR SENSORS.....	1
1.1 Introduction to ring resonators.....	1
1.2 Ring resonator sensing principle.....	2
1.2.1 Evanescent sensing .....	2
1.2.2 Analyte surface density .....	5
1.2.3 WGM sensing modes.....	6
1.2.3.1 Scattering and transmission modes.....	6
1.2.3.2 Absorption mode.....	8
1.3 Current examples of ring resonator sensors.....	8
1.3.1 Solid dielectric microsphere .....	8
1.3.2 Microdroplet .....	14
1.3.3 Cylinder and microcapillary .....	16
1.3.4 Planar ring resonator .....	23
1.3.5 Microtoroid .....	28
1.3.6 Microfiber loop .....	31
1.4 Selection of the OFRR for sensing applications .....	34

2. THERMAL CHARACTERIZATION OF THE OFRR .....	37
2.1 Motivation for thermal characterization .....	37
2.2 Impact of thermal effects in the OFRR.....	42
2.3 Experimental methods .....	45
2.3.1 Materials and fabrication .....	45
2.3.2 Thermo-optic characterization.....	47
2.4 Results.....	50
2.5 Theoretical model .....	54
2.6 Conclusions.....	57
3. FUNDAMENTAL DNA DETECTION WITH THE OFRR .....	59
3.1 Background and introduction.....	59
3.2 Sensor platform.....	60
3.3 Experimental methods .....	62
3.3.1 Materials .....	62
3.3.2 Sensor fabrication .....	64
3.3.3 BRIS measurement .....	65
3.3.4 Experimental protocol.....	65
3.4 Results.....	68
3.5 Conclusions.....	77
4. METHYLATED DNA ANALYSIS WITH THE OFRR .....	79
4.1 Motivation for DNA methylation analysis .....	79
4.2 Experimental methods .....	83
4.2.1 Materials .....	83
4.2.2 Sensor fabrication .....	87

4.2.3	Experimental protocol.....	88
4.3	Results.....	89
4.4	Conclusions.....	93
5.	INTRODUCTION TO RING RESONATOR-BASED MICROFLUIDIC LASERS.....	94
5.1	Background of microfluidic lasers.....	94
5.2	Current examples of ring resonator-based microfluidic lasers .....	96
5.2.1	Solid dielectric microspheres.....	96
5.2.2	Microdroplets.....	97
5.2.3	Cylinder and microcapillary .....	100
5.2.4	Planar ring resonators .....	103
5.2.5	Microfiber loops.....	103
6.	PDMS PACKAGING OF OFRR-BASED MICROFLUIDIC LASERS .....	106
6.1	Motivation for packaging.....	106
6.2	Experimental methods .....	107
6.2.1	Materials and fabrication .....	107
6.2.2	Experimental protocol.....	109
6.3	Results.....	110
6.4	Conclusions.....	116
7.	PDMS-BASED MICROFLUIDIC LASERS WITH NOVEL OUTCOUPLING .....	118
7.1	Motivation and need for novel outcoupling.....	118
7.2	Experimental methods .....	120
7.2.1	Materials and fabrication .....	120
7.2.2	Experimental protocol.....	122

7.3 Verification of output.....	124
7.4 Results.....	125
7.5 Conclusions.....	127
8. SUMMARY .....	130
REFERENCES .....	132
VITA.....	155

## LIST OF FIGURES

Figure	Page
1.1 Schematic of a thick-walled ring resonator with whispering gallery modes (a) and a thin-walled ring resonator with circulating waveguide modes (b). .....	3
1.2 Transmission spectrum showing resonant wavelength shift ( $\Delta\lambda$ ) tracking by identifying the minimum (a). Intensity shift measurement method showing half of a resonant linewidth (b). Reprinted with permission from Chao and Guo (2006). .....	7
1.3 Schematic of a microsphere and fiber taper showing relative mode orientations (a). Microsphere schematic showing molecule immobilization and field intensity (b). Reprinted with permission from Topolancik and Vollmer (2007). .....	9
1.4 Sensorgram showing specific binding of BSA-biotin and streptavidin to a microsphere ring resonator. Reprinted with permission from Barrios et al. (2008). .....	11
1.5 Droplet under oil positioned on a silica sphere (a) and on an ultrahydrophobic surface in air (a). Reprinted with permission from Hossein-Zaddeh and Vahala (2006); Dorrer and Rule (2006). .....	15
1.6 Schematic of a capillary pulling station using CO <sub>2</sub> laser heating. ....	17
1.7 Coupled capillaries with co-resonant WGMs tuned by the 1 <sup>st</sup> resonator. Reprinted with permission from Shopova et al. (2009). .....	18
1.8 A rolled-up InGaAs/GaAs microtube. Reprinted with permission from Kipp et al. (2006). .....	20
1.9 Liquid ring resonator optical sensor (LRROS). Reprinted with permission from Sumetsky et al. (2007) .....	21

1.10 High order evanescent mode profile (a) and non-evanescent interference mode profile (b) for thick-walled capillaries (32 $\mu\text{m}$ ). Reprinted with permission from Ling and Guo (2007).....	22
1.11 SOI slot waveguide (a), liquid waveguide resonator in PDMS (b), silica elevated disks (c), and thin silicon planar ring resonator (d). Reprinted with permission from Almeida et al. (2004); Li et al. (2007); Robinson et al. (2008); Ghulinyan et al. (2008).....	24
1.12 Proposed flow channels for planar waveguides with straight-though output coupling (a) and add/drop output couplers (b). Reprinted with permission from Nitkowski et al. (2005); De Vos et al. (2007).....	26
1.13 Side view (a) and top view (b) of a PMMA annular bragg grating on $\text{SiO}_2$ . Reprinted with permission from Scheuer et al. (2005).....	27
1.14 Silica microtoroid $\sim 120 \mu\text{m}$ in diameter with Q-factor of $1 \times 10^8$ . Reprinted with permission from Armani et al. (2003).....	29
1.15 A coiled multi-loop resonator (a), double loop microfiber resonator (b), and microknot resonator (c). Reprinted with permission from Tong et al. (2003); Sumetsky (2004).....	31
1.16 Conceptual illustration of the OFRR sensor, showing the relationship between photonics and fluidics made possible by this geometry.....	35
2.1 (a) Schematic of proposed two-dimensional OFRR sensor array. (b) Cross-sectional view of an OFRR sensor. ....	39
2.2 Intensity distribution of the second order radial WGMs for two different fused silica wall thicknesses shows that the wall needs to be sufficiently thin to expose the evanescent field to the core. Dashed lines show the interior and exterior surfaces of the OFRR. Refractive index: $n_1=1.33$ , $n_2=1.45$ , $n_3=1.0$ .....	40
2.3 (a) Experimental setup. Aluminum foil covering provides a degree of thermal isolation. A Kanthal wire heating filament coils about the OFRR. Thermocouple is positioned within 1 mm of the coupling region defined by the fiber taper. Vertical line represents coupling fiber. (b) Photograph of the setup with OFRR and taper in place. ....	47

2.4 (a) A resonant mode shifts by $\Delta\lambda$ when the refractive index of the core changes.	
(b) Refractive index sensitivity measurement using diluted ethanol in water (concentrations shown in figure) in a thin walled fused silica capillary with OD of 100 $\mu\text{m}$ . Baseline measurement is pure water. (c) Computed refractive indices versus spectral shift, where the slope is equal to refractive index sensitivity. Sensitivity in this example is 3.6 nm/RIU, corresponding to a wall thickness of 4.3 mm. ....	49
2.5 Example temperature step data for thin-walled aluminosilicate OFRR. Y-axis represents change from lowest mode position. ....	50
2.6 Comparative results for four different OFRRs: thick-walled aluminosilicate ( $\blacktriangledown$ ), thin-walled aluminosilicate ( $\bullet$ ), thick-walled fused silica ( $\blacksquare$ ), and thin-walled fused silica ( $\blacktriangle$ ), where slope of fitted lines indicates spectral shift per degree parameter ( $\Delta\lambda/\Delta T$ ). Thick-walled OFRRs have wall thickness of approximately 8 $\mu\text{m}$ , thin-walled OFRRs have wall thickness of approximately 4 $\mu\text{m}$ . ....	51
2.7 Simulation of spectral response to temperature change for 100 $\mu\text{m}$ OD thick-walled ( $\blacklozenge$ ) and thin-walled ( $\blackstar$ ) aluminosilicate, thick-walled ( $\blacktriangle$ ) and thin-walled ( $\bullet$ ) fused silica, and zero-sensitivity fused silica ( $\blacktriangleright$ ) and aluminosilicate ( $\blacksquare$ ) OFRRs using reported thermal expansion coefficient, $\alpha$ , and experimentally determined thermo-optic coefficient, $k$ . The values of the constants used are listed in Table 2.1. ....	56
3.1 (A) Cross-sectional diagram of an individual OFRR sensor. (B) Side view of the experimental setup. ....	61
3.2 BRIS of 6.8 nm/RIU for the OFRR. Inset: WGM spectral shift when the RI changes in the core. ....	66
3.3 Sensorgram for OFRR surface activation and 25-mer complementary target DNA detection. a: initial baseline; b: 3-APS modification; c: buffer rinses with 3x SSC; d: amine-modified probe DNA incubation; e: target DNA incubation. ....	67
3.4 Net WGM shift for various DNA strand lengths (A) and for various mismatches at the same 10 $\mu\text{M}$ concentration (B). Hybridizations performed at 25° C in 3 x SSC buffer. Displayed standard deviations are 0.45 pm, 0.32 pm, and 1.77 pm for 25-, 50-, and 100-mers, respectively (A), and 1.6 pm, 2.41 pm, and 0.45 pm for 2-base, 1-base, and complimentary target (B). ....	70
3.5 Normalized net WGM shift as a function of the fractional composition of the complementary target DNA. DNA mixtures contain 25-mer complementary DNA and 5-base-mismatched 25-mer DNA. Total concentration: 10 $\mu\text{M}$ . ....	72

3.6 (A) Kinetic data showing binding curves for DNA target that is (1) 100% complementary; (2) 2-base mismatch; (3) 5-base mismatch; (4) completely mismatch. (B) Triangles: Rate constants extracted from (A) using a Langmurian model. Solid curve: exponential fit. DNA concentration: 10 mM. ...	73
3.7 Target DNA titration curve using 25-mer strands. Solid line: Michaelis-Menton curve fit using $K_d = 2.9$ nM and $\delta\lambda_{\max} = 5.1$ pm. Insert shows net shift from 10 pM target using a 37 nm/RIU OFRR.....	75
3.8 Theoretical WGM spectral shift as a function of the molecule density on the OFRR interior surface for various lengths of DNA. The BRIS is chosen to be 6.8 nm/RIU. ....	76
4.1 (a) Experimental setup for OFRR. Inset shows biomolecule immobilization on the interior capillary wall. (b) Representation of methylated DNA strands binding to methyl binding proteins. (c) Representation of methylated DNA strands binding to immobilized antibodies inside the OFRR. ....	83
4.2 Sensorgram showing DNA detection with MBD-2 (a) and anti-5mC (b). For (a) steps are: PBS buffer rinse <b>1</b> , MBD-2 protein immobilization <b>2</b> , and capture of 10 $\mu$ M 30-mer dsDNA with 5 methylcytosines <b>3</b> . For (b) steps are: PBS buffer rinse <b>1</b> , protein G immobilization <b>2</b> , antibody immobilization <b>3</b> , and capture of 10 $\mu$ M ssDNA with 5 methylcytosines <b>4</b> . Inset shows resolvable shift resulting from 5 nM methylated ssDNA.....	89
4.3 Titration curves for MBD-2 experiments including 5-methyl dsDNA (circular data points), 5-methyl ssDNA (square data points), and a negative control containing no methylcytosines (triangular data points). The fitted curve yields a $K_d$ value of 15 nM for dsDNA. The ssDNA data cannot be discriminated from the negative control. ....	90
4.4 (a) Sensorgram for immobilization of 10 $\mu$ M dsDNA with 5 methylcytosines with anti-5mC showing very small net shift. Steps: PBS buffer rinse <b>1</b> , protein G immobilization <b>2</b> , antibody immobilization <b>3</b> , and 10 $\mu$ M ssDNA capture <b>4</b> . (b) Titration curves for anti-5mC experiments using 10 $\mu$ M, 5-methyl ssDNA. The fitted curve yields a $K_d$ of 36 nM for the antibody-based approach. ....	91
4.5 (a) Net resonance wavelength shift values for 10 $\mu$ M DNA with variable methylation states after binding to immobilized MBD-2 proteins. DNA samples were either fully methylated dsDNA (left bars), hemi-methylated dsDNA (middle bars), or methylated ssDNA (right bars). (b) Net resonance wavelength shift values for 10 $\mu$ M ssDNA with variable methylation states after binding to immobilized 5-mC antibodies. ....	92
5.1 Broadband R6G lasing from a PDMS fluid planar ring. Reprinted with permission from Li et al. (2007) .....	95

5.2 Red lasing signal from Rhodamine 590-doped ethanol droplets near the top of the aperture (a), much farther down (b), and with the green scattering signal from pump laser (c). Reprinted with permission from Qian et al. (1986).....	98
5.3 Schematic of microdroplet laser tuning with mechanical deflection (a). Laser spectrum dependence on droplet diameter. Reprinted with permission from Saito et al. (2008).....	99
5.4 Capillary with axial silica rod and ethanol filled fluid cavity with R6G (a) and a photograph of WGM emission (b). Reprinted with permission from Moon et al. (2000).....	101
5.5 Microfluidic laser from 450 $\mu\text{m}$ microknot immersed in an R6G solution. Reprinted with permission from Jiang et al. (2007) .....	104
6.1 (A) Conceptual illustration of the glass based OFRR embedded in a low index polymer. The laser emission can be directionally coupled out through a tapered optical fiber or a fiber prism for easy light delivery. $q$ is the fiber prism angle. (B). The OFRR formed by filling the circular void with high index gain medium. (C) Conceptual illustration of the polymer embedded OFRR array with different laser emission spectra.....	108
6.2 Fabrication process of PDMS-embedded OFRRs for the angle-polished fiber method (a) and the fiber-taper method (b).....	108
6.3 PDMS-embedded OFRR showing optical and fluidic input ports. Top structure is PDMS reservoir and bottom structure is acrylic holder for fiber prism. ....	109
6.4 (a). Top: R6G WGM lasing spectrum collected with a fiber prism. The inset shows the picture of a fiber prism. Middle: Emission from the fiber prism vs. excitation intensity. Threshold is estimated to be $0.7 \mu\text{J}/\text{mm}^2$ . Bottom: Photograph of three color simultaneous emission out of the fiber ends when three parallel OFRRs are filled with Coumarin 504 (left, $\lambda_{\text{peak}}=480 \text{ nm}$ ), R6G (middle, $\lambda_{\text{peak}}=600 \text{ nm}$ ), and LDS 722 (right, $\lambda_{\text{peak}}=730 \text{ nm}$ ). A long-pass filter is used to remove the excitation light. (b) Top: R6G WGM lasingspectrum collected with a tapered fiber. Middle: Emission from the taper vs. excitation intensity. Threshold is estimated to be $0.5 \mu\text{J}/\text{mm}^2$ . Bottom: Photograph of R6G laser emission from the end of a tapered fiber .....	111
6.5 Spectrum of the OFRR laser when Coumarin 504 (1 mM) and R6G (1 mM) mixture is flowed through the OFRR. Excitation wavelength: 450 nm. Laser emission is out-coupled by a fiber prism. ....	113

6.6 Radial distributions for (a) 1 <sup>st</sup> order (b) 2 <sup>nd</sup> order (c) and 3 <sup>rd</sup> order modes. Intrinsic Q-factor for each exceeds 10 <sup>7</sup> . OD = 75 μm, wall thickness = 5 μm, n <sub>1</sub> = 1.626, n <sub>2</sub> = 1.45, n <sub>3</sub> = 1.41. Dashed lines are the OFRR inner and outer surface. ....	115
6.7 WGM resonance displaying a Q-factor of 2.6x10 <sup>6</sup> . Tunable diode laser wavelength is 780 nm. ....	115
6.8 WGM lasing emission from a bare PDMS channel using 0.5 mM R6G. Excitation wavelength is 540 nm. ....	116
7.1 Schematic and corresponding image of single side-coupled OFRR laser (a), two side-coupled OFRR lasers (b), and a spiral OFRR (c). All the ring resonators are filled with dye in TEG whereas the waveguides are filled only with TEG. The magnified region in (a) shows the separation of the OFRR and the waveguide by a 2 μm PDMS gap. ....	120
7.2 Laser interferometric images of a side-coupled ring (a) and a spiral ring (b). A microscope image of a waveguide cross-section shows wall straightness (c). A blow-up of the spiral ring image in (b) highlights the waveguide stub (d).....	122
7.3 Demonstration of outcoupling of the OFRR laser emission into a TEG filled liquid waveguide. (a) Photograph of the OFRR and the waveguide during laser operation. Inset illustrates the experimental setup. (b) Alignment schematic of a collection fiber at the end of the waveguide. (c) Spectra with the collection fiber in and out of alignment. ....	123
7.4 Concomitant lasing emission spectra collected from the waveguide for the dual ring configuration in which 2 mM R6G (a) and 2 mM LDS 722 (b) are injected into each ring, respectively. Both rings are simultaneously pumped. The spectra recorded for each pump intensity are vertically shifted for clarity. (c) and (d) are the corresponding laser emission intensity (at the wavelength marked by black vertical line in (a) and (b)) as a function of the pump energy density. The lasing threshold is 3.7 μJ/mm <sup>2</sup> and 4.0 μJ/mm <sup>2</sup> for R6G and LDS 722, respectively. ....	125
7.5 (a) Photograph of the spiral OFRR and the waveguide during laser operation. Inset shows the PDMS slab and pump beam orientation. (b) The corresponding laser emission spectra collected through the waveguide at different pump energy densities. Curves are vertically shifted for clarity. Inset is the corresponding laser emission intensity (at the wavelength marked by black vertical line) as a function of the pump energy density. The estimated lasing threshold is 25.9 μJ/mm <sup>2</sup> . ....	128
7.6 A single spectrum emitted from a spiral ring structure showing best recorded multi-mode structure. ....	128

## LIST OF TABLES

Table	Page
1.1 Ring resonator characteristics and performance benchmarks.....	34
2.1 Derivation of $\kappa$ from experimental results.....	53
3.1 WGM shift and surface coverage data for various DNA samples.....	67
5. 1 Comparison of lasing threshold and lasing mode for various types of optofluidic ring resonators .....	105

## LIST OF ABBREVIATIONS

- BRIS** – Bulk refractive index sensitivity
- BSA** – bovine serum albumin
- CW** – continuous wave
- DMA** – dimethyl adipimidate
- DMP** – dimethyl pimelimidate
- DNA** – deoxyribonucleic acid
- dsDNA** – double-stranded DNA
- FRET** – fluorescence resonant energy transfer
- HF** – Hydrofluoric acid
- ID** – Inner diameter
- LOD** – limit of detection
- MBD** – methyl binding protein
- OD** – Outer diameter
- OFRR** – Optofluidic ring resonator
- OPO** – optical parametric oscillator
- PDMS** – polydimethyl siloxane
- QD** – quantum dot
- Q* factor** – Quality factor
- RI** – Refractive index
- RIE** – Reactive ion etching
- RIU** – Refractive index unit
- R6G** – Rhodamine 6G
- SMF** – single mode fiber
- SOI** – silicon-on-insulator

**SPR** – Surface plasmon resonance

**ssDNA** – single-stranded DNA

**TE** – transverse electric

**TEG** – tetraethylene glycol

**TM** – transverse magnetic

**WGM** – Whispering gallery mode

**3-APS** – 3-aminopropyltrimethoxysilane

APPLICATIONS OF THE OPTO-FLUIDIC RING RESONATOR FOR  
DNA METHYLATION ANALYSIS AND MICROFLUIDIC LASER  
DEVELOPMENT

Jonathan D. Suter

Dr. Xudong Fan, Dissertation Supervisor

ABSTRACT

For several decades, optical ring resonators have played an important role in the field of telecommunications. Within only the past decade however, ring resonators have been applied for the purposes of biological and chemical detection by means of refractometric signal transduction. The advantage of ring resonator-based sensing is that, unlike fluorescence detection, it is label-free and can yield quantitative data. This document presents the fundamental operation of the versatile opto-fluidic ring resonator (OFRR) and explores its applications in DNA methylation analysis. Using affinity assays based on anti-5-methyl cytosine antibodies as well as the methyl binding protein MBD-2, it is shown that the OFRR is a promising tool for biomedical research that can discriminate the extent of DNA methylation.

As a part of evolving this and other devices towards a practical laboratory and clinical tool, it is important to consider methods for integrating optical functionality onto a compact chip. Towards this end, we also investigate the ability of PDMS-based ring resonators to provide tunable on-chip microfluidic lasers. This idea is explored by looking at two different ring geometries. Very low lasing thresholds are demonstrated.

# CHAPTER 1

## INTRODUCTION TO RING RESONATOR SENSORS

### 1.1 Introduction to ring resonators

Ring resonators are fascinating both for their geometric simplicity and for their ability to efficiently confine optical energy within small mode volumes. In the past couple of decades, optical ring resonators have been employed in many applications, including cavity QED [1, 2], solid-state microlasers [3, 4], nonlinear optics (Raman [5], hyper-Raman [6], Brillouin scattering [7], and four wave mixing [6]), electro-optic modulators [8], optical signal processing (such as filters [9], dispersion compensation [10], and slow light generation [11]), optical frequency combs [12], optical gyroscopes [13], opto-mechanics (including strain [14], radiation pressure [15], and ultrasound sensing [16]), and frequency stabilization [17].

Recently, incorporation of ring resonators with fluidics has come under intensive investigation. Such integration belongs to a newly defined area called optofluidics [18-20], which describes optical systems fabricated with fluids, crafted to enable manipulation of photonics on the micro-scale and build additional functionality into chip-based microfluidics. Optofluidic ring resonators, broadly speaking, are optical devices in which the ring resonator and fluidic systems are combined to produce synergistic functionality that could not otherwise be achieved. The fluidic handling structures involved with such a system may be externally fashioned or may be inherent to the ring resonator geometry.

Optofluidic ring resonators open the door for a number of very exciting applications, among which the most important and most intensively investigated are sensing and microfluidic lasers. Ring resonator sensors include those based on RI detection [21-24], light-absorption [25], fluorescence [26], Raman scattering [27], and cavity-enhanced surface enhanced Raman spectroscopy [28]. With regard to microfluidic lasers, optofluidics provide the benefit of small sample volume, easy sample delivery, large spectral coverage and tunability, and high Q-factor. Microfluidic lasers have been demonstrated using both microdroplets and solid resonators that rely on external fluid as a gain medium. These lasers require the use of a dyes, quantum dots (QDs) or a Raman-signal-generating substances.

## **1.2. Ring resonator sensing principle**

### **1.2.1. Evanescent sensing**

The basic optical phenomenon that allows ring resonators to function is the circular resonant mode, which relies on total internal reflection to circulate light at resonant wavelengths. In a ring resonator, there exist three types of these modes that can be utilized for various applications, the whispering gallery mode (WGM), the circulating waveguide mode, and certain special high-order modes that will be discussed later.

The difference between the WGM and the circulating waveguide mode is that the WGM is guided by the total internal reflection at the outer boundary of the ring resonator, whereas the circulating waveguide mode is confined by the total internal reflection at both the outer and inner boundary (Fig. 1.1 (a) and (b)). The former case occurs in a

microsphere, microdroplet, microdisk, and thick-walled capillary ring resonator, whereas the latter one is represented by a ring-shaped waveguide and thin-walled capillary ring resonators.

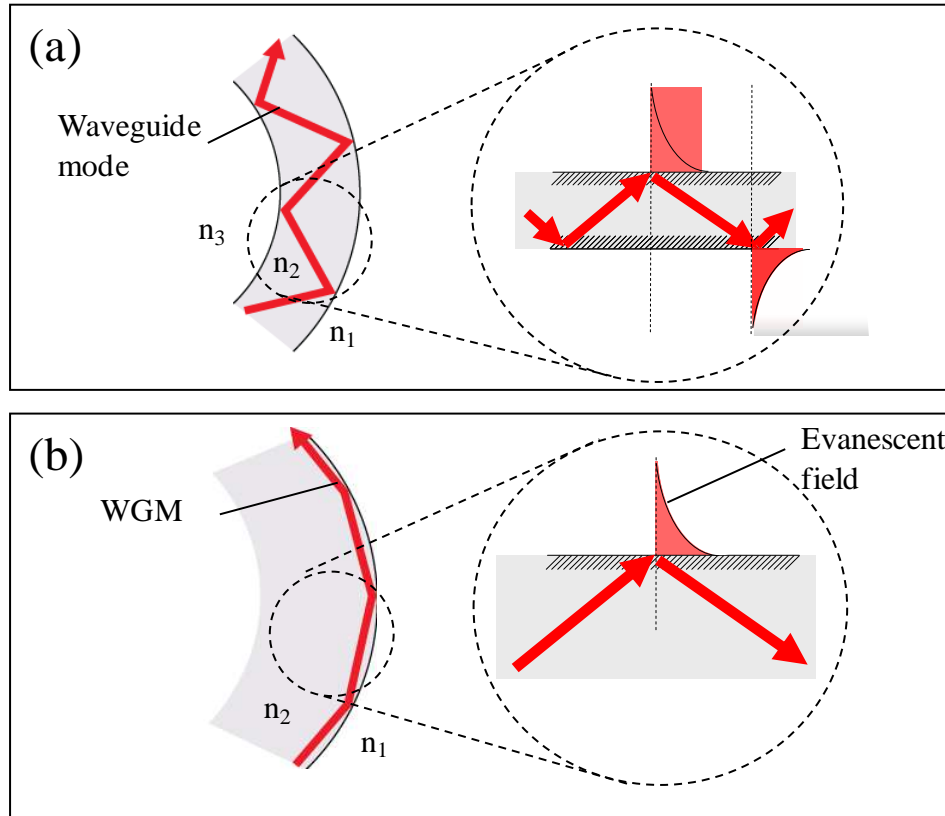


**Figure 1.1.** Schematic of a thick-walled ring resonator with whispering gallery modes (a) and a thin-walled ring resonator with circulating waveguide modes (b).

All ring resonator sensing approaches utilize the evanescent field created by the WGM as a transduction mechanism. The evanescent field created by the WGM typically projects about 100 nm from the ring into the adjacent media [29]. This means that the sensors are limited to interrogation of fluid volumes very near to the surface only, however this can be used to a real advantage.

Refractometric and absorption based sensing belong to so-called “label-free” detection, in which no fluorescent label on analytes is used [30], enabling detection of native unmodified analytes. While some label-free ring resonator sensors use optical absorption (the imaginary part of the complex RI) for sensing, most optical label-free ring resonators are categorized as refractometers, directly detecting changes in the RI (the real part of the complex RI) in the media overlapping the WGM.

Refractometric sensing relies on changing the effective refractive index encountered by the WGM,  $n_{eff}$ . The resonant condition governing WGMs is defined, in general, by the following relationship [31]:

$$2 \cdot \pi \cdot n_{eff} \cdot r = m \cdot \lambda \quad (1.1)$$

where  $r$  is the radius of the ring resonator,  $\lambda$  is the resonant wavelength value, and  $m$  is an integer. The WGM spectral position shifts, when  $n_{eff}$  is altered due to the bulk RI change, in which the RI change occurs in the region longer than the evanescent decay length (which is about 100 nm), or molecular attached to the ring resonator surface, in which the RI change occurs in a distance much shorter than the evanescent field decay length. Thus, by monitoring the WGM spectral position in real time, it is possible to acquire the kinetic and quantitative information regarding molecular interaction.

In RI sensing (and absorption sensing as well), the fraction of the WGM that interacts with the analyte is important. To take into this fractional interaction effect, Eq. (1.1) can be approximately rewritten as [32]:

$$2\pi r \cdot [n_1\eta_1 + n_2\eta_2 + n_3\eta_3] \approx m \cdot \lambda \quad (1.2)$$

where  $\eta_1$ ,  $\eta_2$  and  $\eta_3$ , the fractions of the WGM present outside the resonator, in the resonator material, and inside the resonator core (if applicable), respectively.  $n_1$ ,  $n_2$ , and  $n_3$  are the corresponding RIs. From Eq. (1.2), the bulk refractive index sensitivity (BRIS),  $S$ , can be deduced [33]:

$$S = \left( \frac{\delta\lambda}{\delta n_1} \right) \approx \frac{\lambda}{n_2} \eta_1 \quad (1.3)$$

where we assume that the RI sensing occurs near the outer surface of ring resonator. For the sensing near the inner surface,  $\eta_1$  can simply be replaced with  $\eta_3$ . BRIS values for several different ring resonators are presented in Table 1.1.

### 1.2.2. Analyte surface density

For detection of molecules attached to the ring resonator surface, Eq. (1.3) is no long valid. Vollmer et al. developed a theoretical analysis using the first order perturbation theory to relate the WGM spectral shift,  $\delta\lambda$ , (*i.e.*, sensing signal) to the molecular density on the microsphere surface,  $\sigma_p$  [34, 35]:

$$\frac{\delta\lambda}{\lambda} = \frac{\sigma_p \alpha_{ex}}{\varepsilon_o (n_s^2 - n_b^2) r} \quad (1.4)$$

where  $\varepsilon_0$  is the vacuum permittivity, and  $n_s$  and  $n_b$  are the RI for the sphere and buffer solutions.  $\alpha_{ex}$  is excess polarizability for molecules in water. Recently, another more practical relationship has been established between the BRIS,  $S$ , and molecular surface density [32]:

$$\frac{\delta\lambda}{\lambda} = \sigma_p \alpha_{ex} \frac{2\pi\sqrt{n_2^2 - n_3^2}}{\epsilon_0 \lambda^2} \frac{n_2}{n_3^2} S \quad (1.5)$$

in which  $\delta\lambda$  is the WGM wavelength shift,  $\epsilon_0$  is the vacuum permittivity,  $S$  is the BRIS, and  $n_2$  and  $n_3$  are the RI for the ring resonator and buffer solution. Using Eq. (1.5), it is possible to predict the ring resonator sensing performance for bio/chemical molecules using a simple BRIS characterization.

### 1.2.3. WGM sensing modes

#### 1.2.3.1. Scattering and transmission modes

Experimentally, monitoring the WGM can be done by either collecting scattered light or observing the transmission spectrum of a waveguide coupled to the resonator. Two methods are commonly employed to extract the WGM spectral position [35]. The first method is to scan across a range of wavelengths that includes the resonant position and track the value of the transmission minimum (Fig. 1.2(a)). The drawback of this method is that tunable light sources can be quite expensive and the data analysis is complicated. The second way is to use a fixed wavelength set at the steepest point of the slope on a resonance edge. As the WGM shifts, the transmitted intensity at this wavelength varies rapidly (Fig. 1.2(b)). This method can provide a much more sensitive RI detection method than dip tracking, but only when the measured shifts are very small. When the WGM shifts more than a quarter of a linewidth, the intensity response becomes extremely non-linear and ceases to be useful.

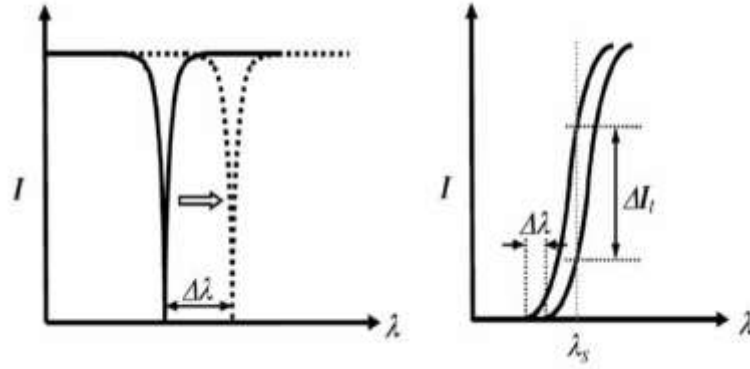


**Figure 1.2.** Transmission spectrum showing resonant wavelength shift ( $\Delta\lambda$ ) tracking by identifying the minimum (a). Intensity shift measurement method showing half of a resonant linewidth (b). Reprinted with permission from Chao and Guo (2006).

While tracking WGM shifts in real time, the spectral resolution will be limited by noises presented in the sensor system, in particular, thermally induced noise and nonspecific binding. Various methods have been proposed to reduce thermal fluctuations [36-39]. These involve modifying the optical cavity in order to cancel out all thermal effects. When the temperature of the ring changes, the refractive properties of both the resonator and surrounding fluid change, and thermal expansion changes the ring radius. Both thermo-optic and thermal expansion effects lead to WGM noise, however they can be used to compensate for one another. The thermo-optic effect in fluids tends to cause negative (or blue) WGM shifts in response to a temperature increase, while thermal expansion and thermo-optic effects in silica cause positive (or red) WGM shifts. Therefore, if the fractional light intensities in the ring and in the evanescent field are balanced perfectly, then in theory the ring should be insensitive to temperature fluctuations. Furthermore, a reference channel can also be implemented along with the sensing channel to cancel out the common-mode noise such as thermally induced noise

and nonspecific bindings.

### **1.2.3.2. Absorption mode**

In addition to refractometric sensing, absorption can be a useful tool. This method leverages the absorptive properties of certain analytes that can manifest themselves by reducing the Q-factor of the cavity [25, 40, 41] or by changing the intensity of the resonant dips observed from the coupling fiber or waveguide [42]. In the former case, the decrease in Q-factor is simply caused by additional losses to absorption, which are dependent on the absorption coefficients, of a given molecular species at a given wavelength. In the latter case, dip depths change in response to changes in the coupling efficiency between resonator and waveguide.

## **1.3. Current examples of ring resonator sensors**

### **1.3.1. Solid dielectric microsphere**

Solid dielectric microspheres serve as excellent optical ring resonators. They can be made out of optically transparent materials such as fused silica [21, 31, 33, 43-45], chalcogenides [46], or even polymers like polystyrene [47-49]. Among different types of microspheres, the fused silica based microsphere is particularly attractive, as it provides extremely high Q-factors. A Q-factor as high as  $10^9$  has been reported when the fused silica microsphere is in air [31]. When immersed in water, the microsphere has a Q-factor in excess of  $10^7$  [21, 45], which results in high spectral resolution and hence low LOD. Additionally, bioconjugation procedures for silica surfaces have been well developed for covalent attachment, which can easily be adapted for fused silica

microsphere based biosensing.

Fabrication of microspheres is usually accomplished by melting the tip of an optical fiber. Using a flame or CO<sub>2</sub> laser, the tip of a fiber is allowed to bead under its own surface tension, typically to around 100 μm in diameter [34, 50]. In this way, it is left on its fiber stem and can be easily manipulated (Fig. 1.3(a)). Also, commercially available silica microspheres can be annealed to achieve optical quality [51].

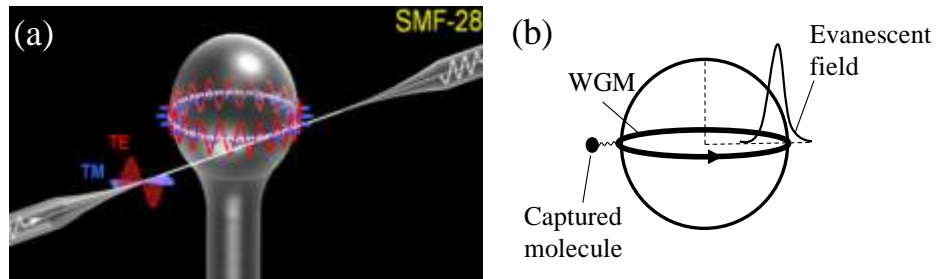


**Figure 1.3.** Schematic of a microsphere and fiber taper showing relative mode orientations (a). Microsphere schematic showing molecule immobilization and field intensity (b). Reprinted with permission from Topolancik and Vollmer (2007).

Fused silica microspheres have been employed in both refractometric sensing and biological sensing applications. Fig. 1.3(b) shows how immobilized molecules interact with the WGM at the equator where evanescent intensity is high. Once fabricated the spheres can be inserted into fluidic chambers or aligned with the input and collection optics. For refractometric sensing, a BRIS of approximately 30 nm/RIU with a detection limit of  $3 \times 10^{-7}$  RIU was achieved [21]. For biological sensing, the surface of the microsphere is first coated with a layer of biorecognition molecules, such as single-stranded DNA [21, 53], antibodies [54], aptamers [55], and peptides [43].

Specific biosensing applications have included several works on protein detection [32, 34, 45, 56]. In 2002, a 300  $\mu\text{m}$  microsphere was used to investigate bovine serum albumin (BSA) adsorption as well as the interaction between streptavidin and a BSA-biotin conjugate. Fig. 1.4 shows the sensorgram resulting from streptavidin binding to biotin on the sphere surface [34]. A positive net WGM shift was observed, indicating higher biomass loading on the sphere surface. A further study with BSA using similar adsorption techniques showed that detection of only a few protein molecules was possible [45]. In 2007, one further BSA effort was published, focusing on the difference in microsphere sensitivity using different polarizations [56]. Specifically, the ratio of WGM shift of TE and TM modes was used to determine the extent of BSA's polarizability anisotropy. Fig. 1.3(a) shows the relative orientation of TE and TM modes within a microsphere. As an extension of this protein work, it is possible to monitor enzymes by monitoring the cleaving of protein molecules. This was demonstrated using a BSA-trypsin model in which trypsin cleaves a part of BSA originally on the WGM [43]. As a result, a negative shift in the WGM spectral position was observed. Clinically relevant biomolecules have also been detected with the microsphere. For example, thrombin it plays an important role in the process of blood coagulation. The detection of thrombin levels has many potential applications including therapies for cardiovascular diseases like atherosclerosis and surgical procedures [57]. Using a aptamer coated microsphere, thrombin in buffer was detected with a LOD of around 1 NIH unit/mL, or roughly 6 nM [55].

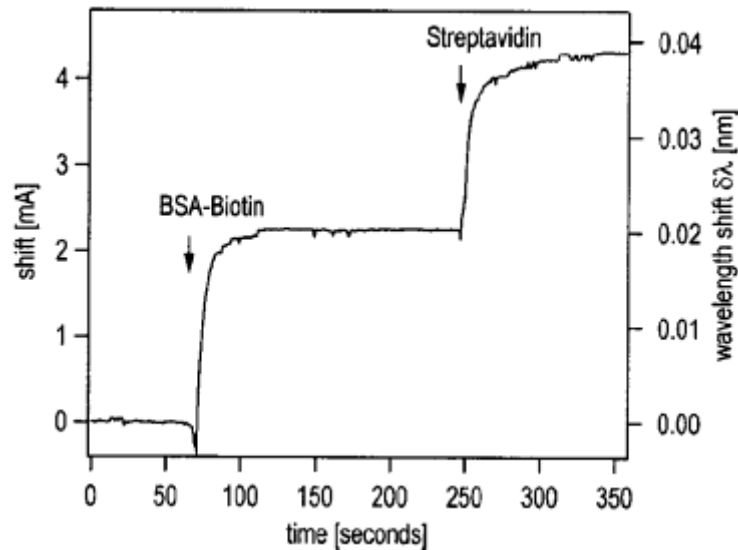


**Figure 1.4.** Sensorgram showing specific binding of BSA-biotin and streptavidin to a microsphere ring resonator. Reprinted with permission from Barrios et al. (2008).

One further BSA experiment that is worthy of note was conducted by Francois and Himmelhaus (2009) using dye-doped microsphere lasers. In this particular study, polystyrene microspheres with Nile Red dopant were deposited on a glass slide and lased using a pulsed excitation source. The lasing spectrum from WGMs was tracked as reagents were flowed over the spheres. BSA deposition was monitored and analyzed in terms of adsorption kinetics [58].

DNA detection is also of keen interest for a number of purposes. Typically, detection is accomplished by attracting the target DNA molecule via complementary strand hybridization. Vollmer, et al. was able to detect as little as  $6 \text{ pg/mm}^2$  11-base target strands and to differentiate single-base mismatched DNA from complementary one [33]. The results further demonstrated the detection of single-base-mismatched DNA. Another effort used much smaller,  $7.5 \text{ }\mu\text{m}$  silica microspheres coated with dye-labeled DNA

probes [53]. The dye, tetramethyl rhodamine, was excited from an external source, and its fluorescence was coupled into the WGMs in the spheres and was then collected through a free space collection system to indicate the WGM spectral position. Hybridization between the probe and complementary target DNA strands, then, caused a shift in the characteristic WGM peaks within the fluorescence spectrum. The DNA targets were 5  $\mu\text{M}$  using lengths between 10 and 40 nucleotides. Similar experiments were also carried out with polystyrene beads with diameters between 1.5 and 20  $\mu\text{m}$  impregnated with Nile Red dye to assay solutions of both BSA and the polyelectrolytes poly(allylamine hydrochloride) and poly(sodium 4-styrenesulfonate) [59]. A LOD of roughly 213  $\text{pg}/\text{mm}^2$  was achieved. Despite the relatively low spectral resolution (because of relatively low Q-factors), this method provides an easy method for monitoring the WGM spectral position without any sophisticated in/out coupling systems (such as fiber tapers, prism, etc.), which may open a door for in-vivo and remote in-vitro WGM sensing [59, 60].

Larger analytes have been investigated with microsphere biosensors, specifically with whole cell bacteria and virus particles. E. Coli was immobilized on a microsphere surface by starting with a poly-L-lysine coating [61]. In addition to monitoring the WGM shift through a coupled optical fiber, the surface of the sphere was monitored by a microscope in order to ascertain surface densities. It was discovered that the LOD of this approach was  $10^2$  bacteria/ $\text{mm}^2$ , corresponding to approximately 44 total cells on the microsphere. Very recently, single viral particle detection has been achieved using 50  $\mu\text{m}$  silica microspheres using 10 fM of Influenza A virions [62]. A defining characteristic of single particle adsorption was presented, showing step-wise shifts from individual viral

particles. This is in sharp contrast to typical adsorption curves in lower-sensitivity systems where discrete WGM shifts are impossible to resolve. Interestingly, the sizes of these steps are not uniform, which is caused by the difference in sensitivity as particles bind closer or farther away from the “equator” of the WGM where the optical energy density is the highest.

There have been many theoretical works that have been developed to characterize the microsphere’s performance as a sensor for biological analytes [61, 63]. These include theoretical models such as Eq. (1.5), which relate the WGM shift to surface densities of molecules on a microsphere surface [33]. Such work has also been extended to the case of virus particles and cells whose sizes are larger than the WGM evanescent decay length. The work by Keng et al. (2007) explored the ability of the microsphere to study Brownian motion in microparticles [63], which is an important phenomenon to understand in order to interpret results from biosensing experiments. From monitoring diffusion processes, particle sizes can also be inferred. Such works are applicable to chemical as well as biological sensing.

Some important chemical sensing examples include the detection of mercury ions in water down to 50 ppb [50], polar crystals (pentacene and terrylene) [64] and even for the removal of silica monolayers from the sphere using HF [65]. The removal of 4 pm of silica (0.4 fmoles of silica) from the sphere caused a detectable shift in the WGM, indicating that sub-monolayer thickness changes can be detected. This was an important demonstration of the microsphere’s ability to detect molecules smaller than those typically targeted in biomolecular assays.

To this point, the microsphere has been discussed as a refractometer used for tracking WGMs. Since microspheres have very high Q-factors, the WGM spectral linewidth (instead of spectral shift) can also be used to generate sensing signal. This is particularly useful when detecting the optical absorption (the imaginary part of the complex refractive index) and hence the concentration of the analyte present in the WGM field, since molecules, such as dyes, will cause a degradation of the measured Q-factor [40].

Although the microsphere ring resonator has demonstrated highly sensitive detection, mass-production and integration with microfluidics for efficient sample delivery continues to be very challenging. In order for microspheres to be practical beyond the research laboratory, these issues must be addressed more conveniently in future work.

### **1.3.2. Microdroplet**

Geometrically, a microdroplet is nearly identical to a solid microsphere discussed in the previous section. However, the microdroplet is very unique in that it serves dual functions of microfluidics and of a ring resonator. In contrast to a solid microsphere, the predominant electric field of the WGM that forms along the microdroplet surface lies inside the microdroplet, resulting in a large light-analyte interaction that can be explored for many applications (such as in sensing and microfluidic lasers).

Microdroplets of water [66], methanol [67], and ethanol [68] can be formed by an aerosol generator [69], or in oil [70, 71] (Fig. 1.5(a)), on an ultrahydrophobic surface [27,

71-74] (Fig. 1.5(b)), or levitated by electrodes [75, 76] or optical tweezers [77]. Many of these control mechanisms are also useful for microdroplet lasers. The size of the microdroplet can be as small as a few micrometers, which corresponds to a total fluidic volume on the order of pico-liters. Such a small volume is highly desirable in the development of biosensors with low sample consumption and in fundamental research such as single molecule detection [78]. The tuning of the droplet size has been demonstrated using the electrowetting method [71, 74, 79].

Microdroplets offer the best surface quality of any ring resonators available, resulting in negligible surface scattering induced loss. Consequently, the Q-factor of a microdroplet is mainly determined by the optical absorption of the solvent. Within the visible spectrum, water, methanol, and ethanol absorption is very low ( $\sim 0.001 \text{ cm}^{-1}$ ) [80], resulting in a Q-factor of up to  $1 \times 10^8$ .

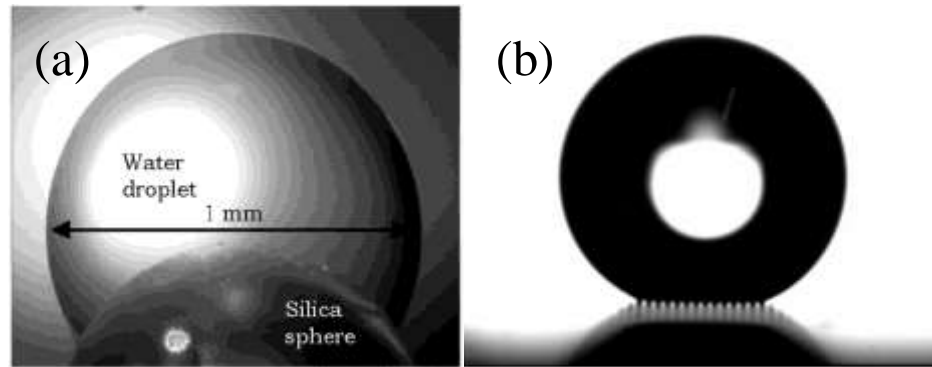


**Figure 1.5.** Droplet under oil positioned on a silica sphere (a) and on an ultrahydrophobic surface in air (a). Reprinted with permission from Hossein-Zadeh and Vahala (2006); Dorrer and Rule (2006).

Despite these merits, microdroplets suffer from difficult integration into practically viable devices. Excitation of the WGM through waveguiding structures such

as tapers and prisms is very challenging. Furthermore, the time-dependence of resonance in an evaporating droplet is a significant practical limitation [71] (although immersion in oil helps prevent evaporation, the system becomes more complicated). To date, only a very few refractometric sensing or label-free biosensing applications have been demonstrated on microdroplets, leaving this area an attractive field for further exploration. One of these applications involves detection of single *E. Coli* cells in a PBS buffer droplet doped with R6G [81]. WGM peaks from the R6G emission are suppressed upon adding cells due to absorption and scattering effects. This procedure is label-free despite the use of dyes because the cells are not actually tagged with them.

Most of the applications of droplets have been in fluorescence-based sensing [82] and microfluidic lasers, which will be discussed in detail in the following chapters.

### **1.3.3. Cylinder and microcapillary**

Cylindrically-shaped ring resonators may be created out of a solid post, such as a segment of an optical fiber, or a hollow capillary. The former configuration can be used in exactly the same manner as the solid microsphere in biochemical sensing that has been discussed earlier, where an extrinsic microfluidic chamber or channel is required to deliver samples to the ring resonator. In contrast, the hollow capillary configuration differs from the solid cylinder ring resonator drastically, as it serves both as a resonator and as a microfluidic channel that conducts sample fluid. Furthermore, the capillary based ring resonator relies on the evanescent field on or near the inner surface (rather than the outer surface) of the capillary.

In order to obtain a sufficient electric field of the WGM near the capillary inner wall, the wall thickness of the capillary needs to be only a few micrometers [23, 32, 83]. These thin-walled capillaries are almost exclusively fabricated out of silica glass starting with a large capillary perform [23, 83]. Under intense heat from a torch or CO<sub>2</sub> laser the glass is softened until it can be easily pulled to very small dimensions. An example of such a method is shown in Fig. 1.6. This process is similar to the manufacture of microspheres, except that in the microsphere case the glass is heated until it completely liquefies whereas in capillary fabrication, relatively low heat and high pulling speed are needed to ensure that the capillary does not collapse and that the original aspect ratio (wall thickness vs. outer diameter) remains the same. In the end, the capillary will be on the order of 10-100  $\mu\text{m}$  in diameter with a thickness as thin as 1-2  $\mu\text{m}$ . If needed, the wall is etched thinner with hydrofluoric acid.

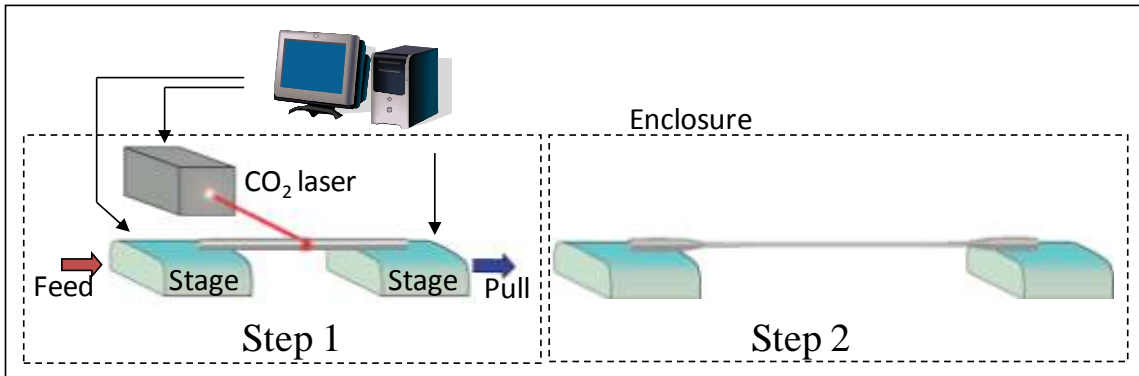


**Figure 1.6.** Schematic of a capillary pulling station using CO<sub>2</sub> laser heating.

When the WGMs become sensitive to the RI of the interior fluid, the configuration can be utilized as a sensor for biological and chemical analytes [28, 55, 84-89]. This type of sensor has demonstrated BRIS benchmarks of 51.9 nm/RIU with thin-

walled capillaries [90] (in fact, according to unpublished results over 100 nm/RIU has been achieved) and can provide Q-factors of over  $10^7$  [85], leading to a LOD on the order of  $10^{-6}$ - $10^{-7}$  RIU [85]. A dual capillary scheme called the optofluidic coupled ring resonator (OCRR) has been explored for a RI LOD estimated at around  $1 \times 10^{-9}$  [84] (Fig. 1.7). In this case, two parallel capillaries are coupled to each other and interference between co-resonant WGMs create split modes that shift relative to one another based on the RI of the fluid inside the capillaries [91].

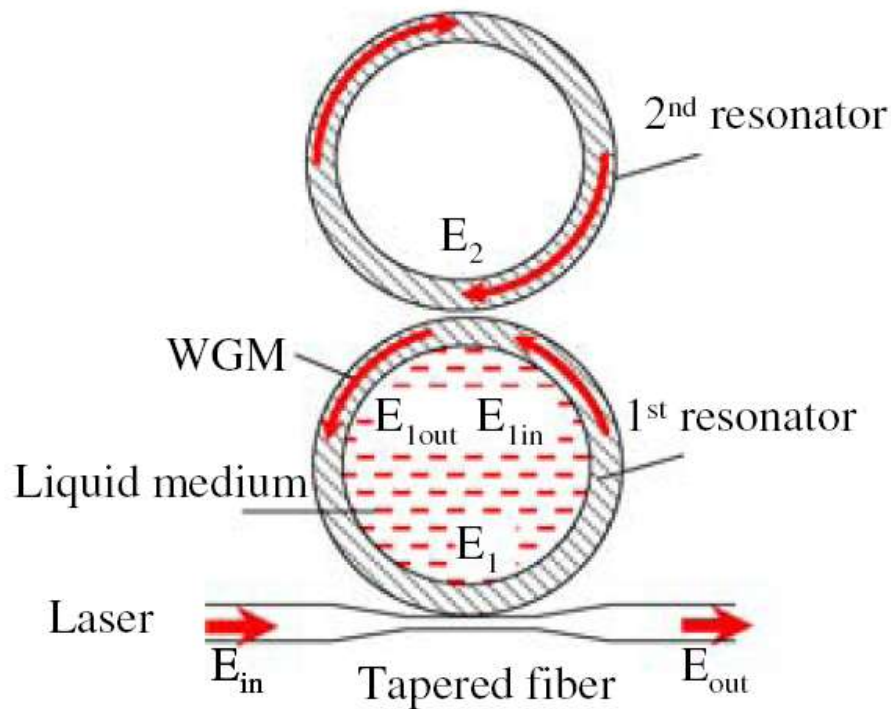


**Figure 1.7.** Coupled capillaries with co-resonant WGMs tuned by the 1<sup>st</sup> resonator. Reprinted with permission from Shopova et al. (2009).

The microcapillary ring resonator has been demonstrated for a wide variety of biosensing purposes. Biorecognition molecules are first coated on the interior surface of

the capillary and then the fluid sample is flowed through the capillary using a mechanical pump, capillary force, or electro-osmosis. As will be described in the coming pages, the thin-walled capillary is able to detect single-stranded DNA molecules at concentrations down to 10 pM and discriminate a single mismatched nucleotide [92]. It can also detect streptavidin down to 100 pM using a peptide-binding phage [86]. Rapid and sensitive virus detection has also been presented. M13 viral particles down to  $2.3 \times 10^3$  pfu/mL were detected in only five to ten minutes [88]. Given the small sample volume used in this experiment, only a few tens of viral particles are detected.

In each of these sensing applications it can be quite useful to be able to estimate the amount of material immobilized on the sensor surface. Eq. (1.5), shows how surface density of molecules is related to the WGM shift [32] and is described in detail above. The same model has been used to determine the surface density of BSA protein layers in a capillary [32].

Another microcapillary design uses microtubes that are composed of rolled up semiconductor materials [22, 94-98]. By growing very thin alternating layers (sub-micron) of materials with induced strain at the interface, the material can be caused to roll up into a tube ranging from 2 to 5 microns in outer diameter (Fig. 1.8). These layers have been created with InGaAs and GaAs, which have a lattice mismatch that naturally places strain on the interface [93, 95, 97]. However, Si/SiO<sub>x</sub> layers have also been recently demonstrated [22, 98]. When the layer underneath them is etched away, this strain causes the rolling effect. After rolling, the tube is annealed at very high temperature (around 850°C for Si/SiO<sub>x</sub> [98]) and can then be used as a cylindrical ring resonator. These

resonators have shown BRIS values of up to 62 nm/RIU [22] and Q-factors around  $3 \times 10^4$  [93]. While these tubes are much better suited for on-chip integration, their performance is limited by this low Q-factor, caused by irregularities in the tube wall.

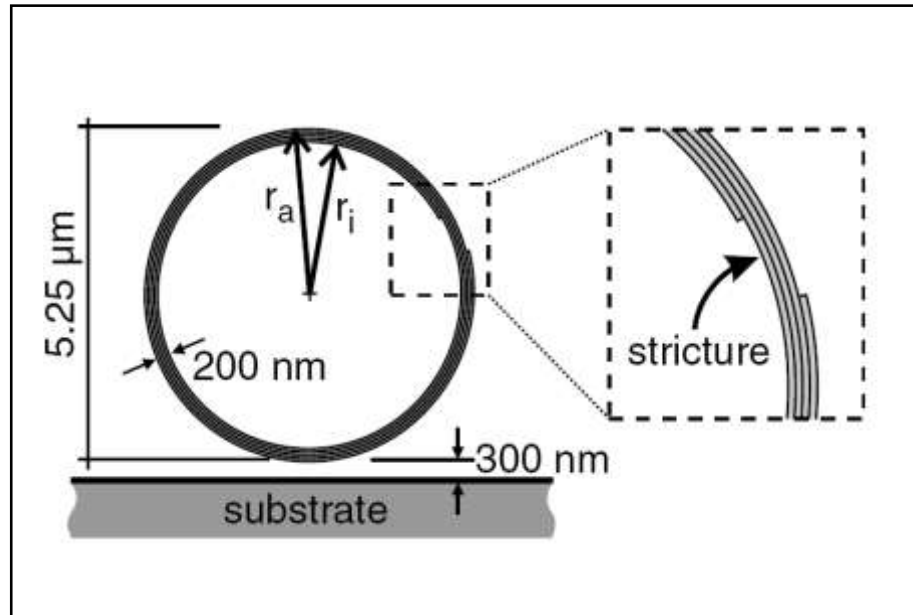


**Figure 1.8.** A rolled-up InGaAs/GaAs microtube. Reprinted with permission from Kipp et al. (2006).

So far in this section we have discussed evanescent label-free detection using thin-walled silica capillaries and rolled tubes. Next we will discuss two special cases of capillary ring resonators which are able to push the WGM into the sample fluid inside the capillary core. In the first case, the majority of the electric field may also be pushed into the fluid by simply etching the wall thickness to extremely small dimensions. In such a case, the pre-etched capillary must be embedded within a very low RI polymer for support. This was successfully accomplished by embedding the glass capillary in a polymer with RI = 1.384 and etching the wall with HF until the optical resonances in the glass disappeared [99]. This configuration has been named the liquid ring resonator

optical sensor (LRROS) (Fig. 1.9). Running a fluid through the core with RI greater than that of the polymer, ultra-high sensitivity refractometric measurements could be made. BRIS was observed to be 800 nm/RIU. While this is one of the best sensitivities available from ring resonator sensors, the need to use solvents with RI greater than the RI of the encasing polymer is one of its limitations. Furthermore the biosensing applications of this type of microcapillary have yet to be explored.

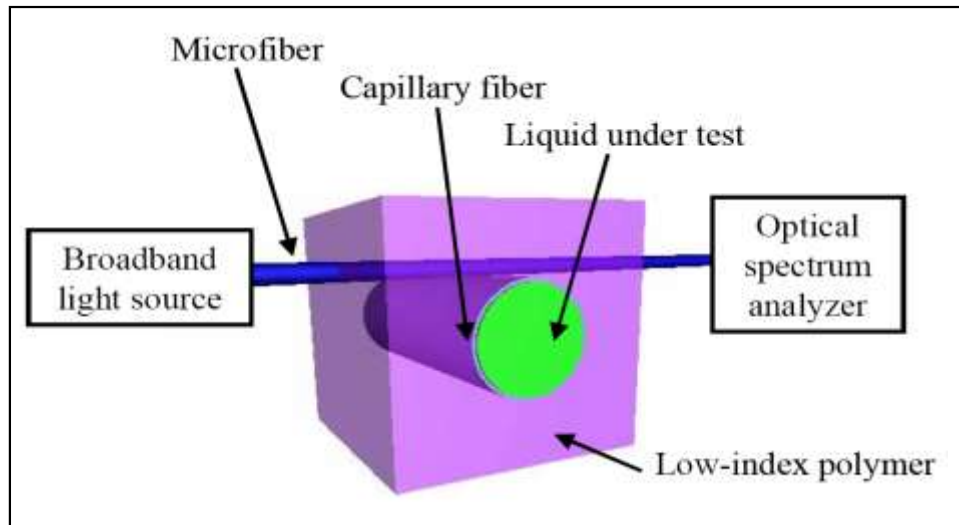


**Figure 1.9.** Liquid ring resonator optical sensor (LRROS). Reprinted with permission from Sumetsky et al. (2007).

Extreme thinning of the wall is an interesting approach, but it is not necessarily required in order to push WGM energy into the capillary core. In the second case, with a wall 32  $\mu\text{m}$  thick, low order WGMs are completely confined within the wall and only the WGMs of higher order can be utilized for sensing [100]. This phenomenon of sensing using thicker walls (32  $\mu\text{m}$ ) has been investigated looking at two types of modes, both having very high radial order numbers. The first of these has evanescent field decaying into the core, but the majority of the WGM intensity remains within the wall (Fig

1.10(a)). The BRIS of this configuration is capable of reaching approximately 100 nm/RIU. The second type of mode is of an even higher radial order number and arises from positive interference between reflected and refracted beams incident upon the wall/core interface, as discussed in earlier. The majority of this non-evanescent mode's field intensity energy lies within the core (but not on the interior surface) (Fig. 1.10(b)), enabling BRIS up to 600 nm/RIU with a Q-factor of  $2 \times 10^4$ . This mode has very high BRIS, but it cannot be used for biosensing where an evanescent field is needed. In the case of biosensing, the bulk RI may play too much of a role in the resultant optical signal. As a result, it becomes difficult to differentiate the actual specific binding occurring on the interior surface from the interfering analytes flowing through the capillary that do not bind to the surface, if this type of mode were used for biomolecule binding detection.

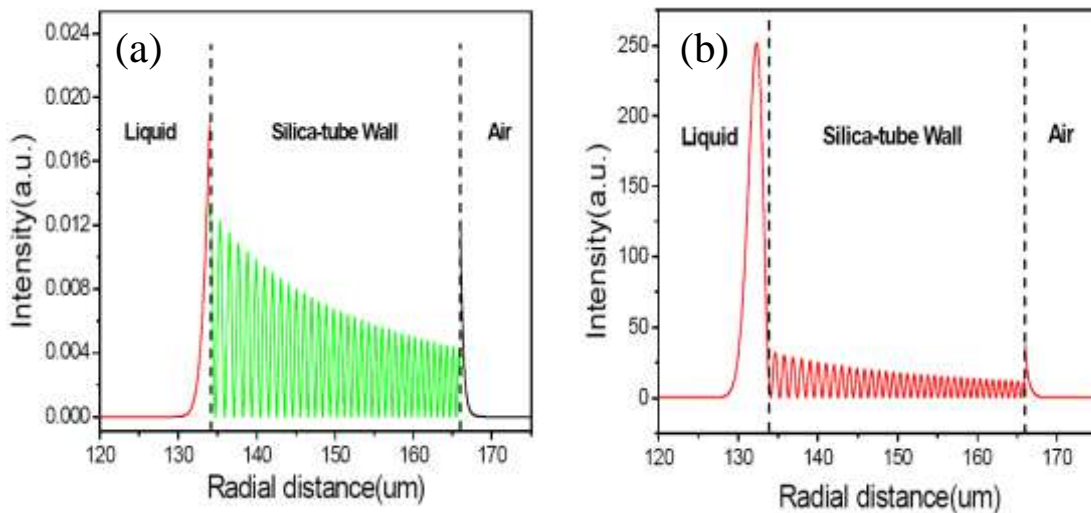


**Figure 1.10.** High order evanescent mode profile (a) and non-evanescent interference mode profile (b) for thick-walled capillaries (32  $\mu\text{m}$ ). Reprinted with permission from Ling and Guo (2007).

All of the capillary based ring resonators discussed above share the same fluidic

integration advantages. As a consequence, they are highly compatible with column based analytical chemistry technologies and can be employed to develop novel capillary electrophoresis [87] or micro-gas chromatography [101-103] with real-time, sensitive, on-column detection capability. In the electrophoresis study, glycerol was used in order to establish the proof of concept and flow was controlled by means of electro-osmotic flow [87]. In the gas chromatography study, the inside of a capillary was coated with a vapor sensitive polymer, which interacts with transmitted gas species. Separation and detection of various vapors have been demonstrated with a sub-nanogram LOD.

#### **1.3.4. Planar ring resonator**

Microfabrication techniques have advanced to the point where top-down construction of micro- and nano-sized structural features is a routine task. Soft lithography techniques enable fabrication of features below 100 nm using photomask-based replica molding [104], and down to 2 nm with imprinting technologies using PDMS on molds made using chemical vapor deposition [105]. E-beam lithography, focused ion beam, and related technologies have also paved the way for construction on the sub-wavelength scale. This has enabled chip-based ring resonator structures, which are excellent candidates for biological and chemical sensing.

Planar ring resonators, as they may be called, are a category of optical cavities that are manufactured using any combination of layer deposition and removal phases on top of a semiconductor substrate. A common subset of these devices is SOI, or silicon-on-insulator, ring resonators, in which silicon structures are fabricated on a layer of

insulating material, commonly SiO<sub>2</sub> [106-116] (Fig. 1.11(a) and (b)). Polymer ring structures [49, 117, 118], polyimide [119], sapphire [120], and silicon nitride (SiON) [121] have also been used. Notable exceptions also exist, for instance using high RI fluids in channels fabricated with soft lithography [122] (Fig. 1.11(b)).

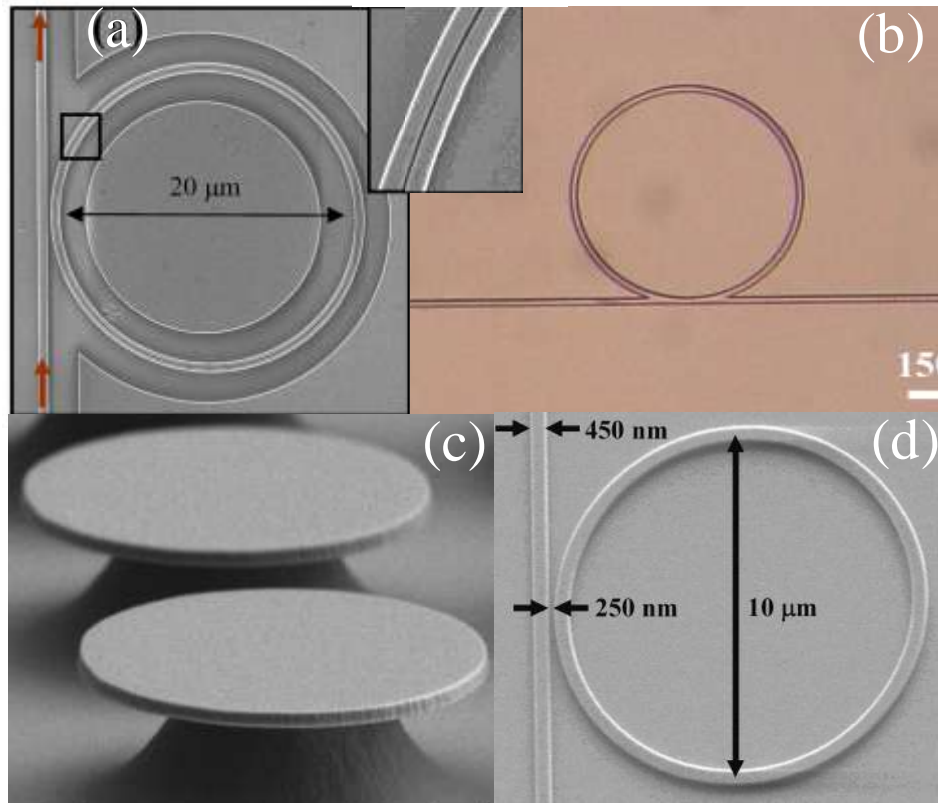


**Figure 1.11.** SOI slot waveguide (a), liquid waveguide resonator in PDMS (b), silica elevated disks (c), and thin silicon planar ring resonator (d). Reprinted with permission from Almeida et al. (2004); Li et al. (2007); Robinson et al. (2008); and Ghulinyan et al. (2008).

One of the greatest benefits to using planar ring resonator sensors concerns packaging and reproducibility. Once templates and protocols for manufacture have been optimized, rings can be duplicated to very high tolerances. This is not always true of other ring resonator platforms. Once fabricated on-chip, sensors require an effective

fluidics handling system. Often, the solution to this entails building a flow channel on top of the ring and controlling fluid flow via a peristaltic pump, syringe pump or other method [107, 125]. Flow chambers are frequently constructed using PDMS-based soft lithography techniques (such as those proposed in Fig. 1.12). These PDMS layers can then be plasma-treated and bonded to the ring substrate.

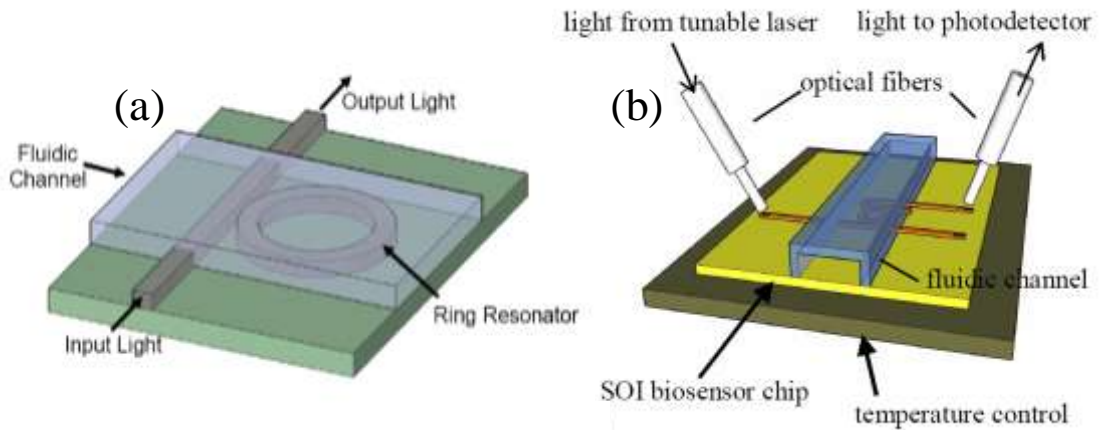


**Figure 1.12.** Proposed flow channels for planar waveguides with straight-through output coupling (a) and add/drop output couplers (b). Reprinted with permission from Nitkowski et al. (2008); De Vos et al. (2007).

Planar ring resonators have shown excellent BRIS performance – in the range of 100-200 nm/RIU [125] - but their Q-factors tend to suffer from surface roughness problems [126, 127]. An SOI ring 200  $\mu\text{m}$  in diameter with a waveguide width of 450 nm yields a Q-factor of  $1.2 \times 10^5$  in air [25]. This is among the best such values demonstrated for planar ring resonators. The use of different materials can lead to slightly better performance than this, however. For example, sapphire discs have shown Q-factors up to  $4.5 \times 10^5$  [120]. Despite low Q-factor, planar rings have been a popular ring resonator configuration due to the fact that they can be reproducibly manufactured and

easily integrated into chip-based processes.

Both disc [128] (Fig. 1.11(c)) and circular ring-shaped planar waveguides [129] (Fig. 1.11(d)) have been proposed for biological sensing of pathogens. In order to decrease the footprint of the ring while maintaining a large interaction area, folded and spiral SOI shapes are also possible [106]. Streptavidin-biotin affinity has been used as a proof of concept in a few setups because of their well-known binding affinities for each other [125, 129]. A LOD of  $250 \text{ pg/mm}^2$  for streptavidin binding to a polystyrene ring covered with biotin has been demonstrated [117]. With a folded ring SOI cavity, streptavidin detection down to  $3 \text{ pg/mm}^2$  [106]. This value represents mass loading of protein on the sensor surface. LOD for the bulk concentration of streptavidin has also been reported down to  $10 \text{ ng/mL}$ , corresponding to roughly  $150 \text{ pM}$  [107].

A good example of how planar rings can be integrated into functional systems has been published, using an array of  $100 \text{ }\mu\text{m}$  rings packed into a very small area [130]. The waveguides collecting signal from each ring were U-shaped, which allows the sensors to be placed side-by-side. Each ring was fabricated out of hydrex glass that was demonstrated with several different biomolecules, including antibodies, DNA, bacterial cells, and proteins.

In 2004, a very unique solution to optical confinement in low RI was proposed in which a configuration called the “slot waveguide” was utilized [131] (Fig. 1.11(a)). The device is composed of two concentric planar rings which are separated by a distance of between  $40$  and  $200 \text{ nm}$  [112, 123, 131-137]. The exact spacing required depends entirely upon the wavelength of light being used. This unique mode of confinement

relies on solutions to Maxwell's Equations in which the electric field of the optical mode undergoes a large discontinuity. If the two concentric waveguides are close enough together to interact, then the majority of the field intensity must exist within the low-index gap [131]. The slot waveguide has been demonstrated for RI detection of different chemicals, including cyclohexane and isopropanol and has been proposed for other biological or chemical sensing purposes [133]. It has also been demonstrated for the detection of BSA and anti-BSA antibodies with LODs of 16 and 28  $\text{pg}/\text{mm}^2$ , respectively [132]. A polymer ring was recently used for detecting glucose with a BRIS close to 200  $\text{nm}/\text{RIU}$  [138]. The LOD for glucose was estimated to be approximately 200  $\mu\text{M}$ .

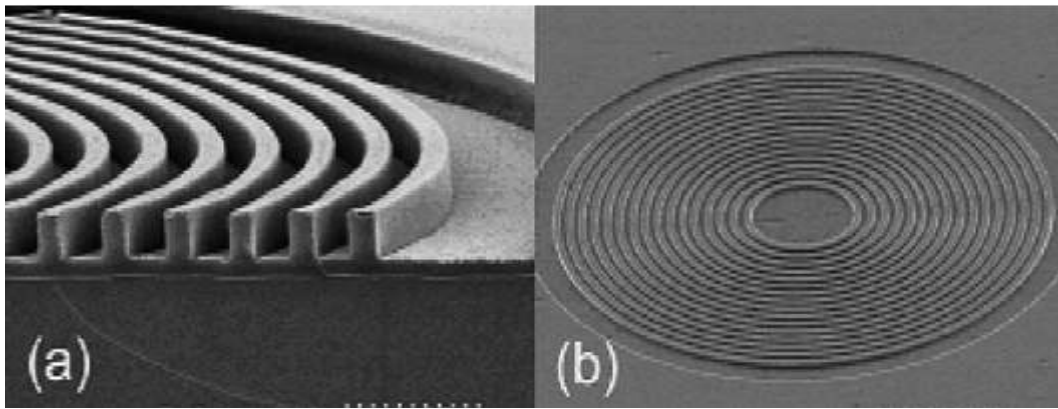


**Figure 1.13.** Side view (a) and top view (b) of a PMMA annular Bragg grating on  $\text{SiO}_2$ . Reprinted with permission from Scheuer et al. (2005).

The annular Bragg resonator and onion-like resonator are unique ring resonators which are non-WGM based [139, 140] (Fig. 1.13). Using concentric rings of alternating RI materials, an omnidirectional Bragg grating is created. Introducing a defect, then, creates a ring-shaped Bragg resonator capable of Q-factors on the order of  $1 \times 10^3$  and BRIS approaching 400  $\text{nm}/\text{RIU}$  [139]. The majority of optical field intensity is then

concentrated in the defect, where light-matter interaction takes place. These structures have been used to detect RI changes down to  $5 \times 10^{-4}$  [141].

Similar to microspheres, planar ring resonators can also be employed for optical absorption measurement [25]. A 200  $\mu\text{m}$  diameter planar ring was used to detect N-methylaniline by measuring the Q-factor changes due to absorption. This chemical, which absorbs strongly near 1500 nm, was used to demonstrate that ring resonators can measure absorbance with accuracy similar to that of commercial spectrophotometers.

### **1.3.5. Microtoroid**

The first microtoroid was proposed in 2001 and was essentially a bottled segment of a silica fiber [142]. This effort produced a resonator with a Q-factor of  $10^7$  and was aimed at reducing the number of supported modes within the resonator compared with the microsphere platform. The contemporary microtoroid on-chip, however, consists of an etched elevated disk which has smoothed edges and an even smaller mode volume [143]. Typically, microtoroids are fabricated by photolithographically depositing circular  $\text{SiO}_2$  pads on a silicon substrate. Then, the silicon is etched out from underneath until the circular pad is suspended in air by a thin pedestal. The surface of the disk is then irradiated with a  $\text{CO}_2$  laser, causing the edges to bead into the desired toroid shape [144] as shown in Fig. 1.14.

The microtoroid on-chip has gained a lot of attention over the last few years due to the greatly advanced Q-factor it offers over the previously explored elevated disk platform [12, 38, 39, 41, 143-149] due to the significant reduction in scattering loss

resulting from the surface roughness. In fact, Q-factors up to  $2 \times 10^8$  in water have been reported [38].

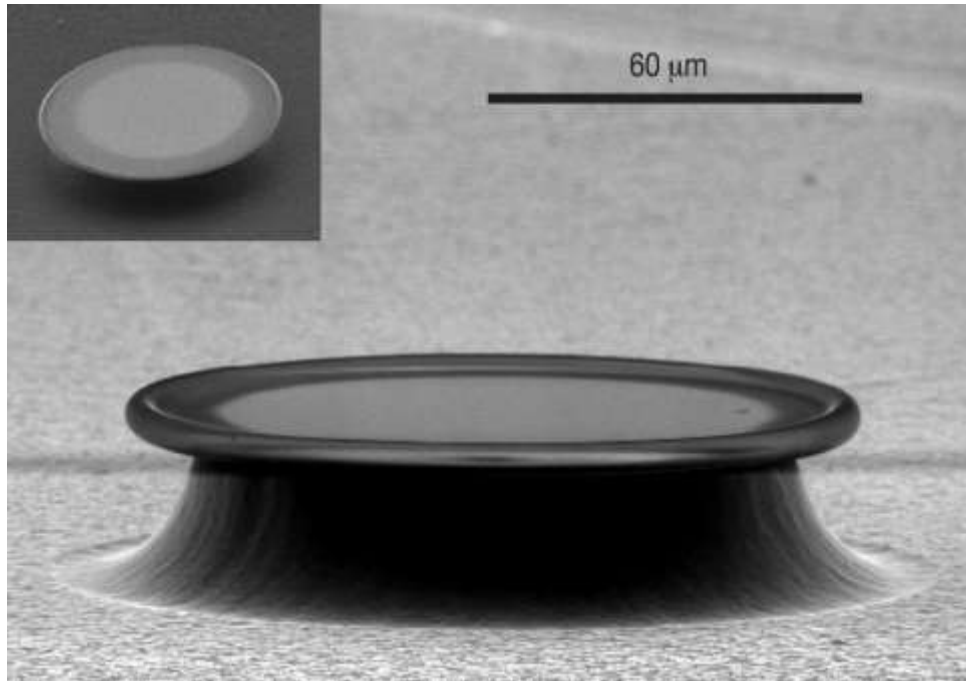


**Figure 1.14.** Silica microtoroid  $\sim 120 \mu\text{m}$  in diameter with Q-factor of  $1 \times 10^8$ . Reprinted with permission from Armani et al. (2003).

It is also possible to fabricate the toroids out of PDMS molds [145, 149]. The molded polymer toroid resonators, being only as smooth as the original PDMS mold, were only able to achieve Q-factors up to  $3 \times 10^5$  [145], however this methodology allows the use of more cost-effective materials and does not require clean-room facilities. By comparison, the Q-factor achieved by these molded toroids is still competitive to, or better than, the Q-factors achievable with normal elevated disk resonators.

These resonators have been demonstrated as sensors for heavy water [41] and interleukin-2 in serum [38]. In the former case, the difference in optical absorption between heavy water and normal water is observed based on its impact on the Q-factor of

the cavity [41]. In the latter case, raw WGM mode shifts are tracked in order to observe interleukin binding to immobilized antibodies [38]. This work claims single-molecule detection based on an additional WGM shift enhancement from thermo-optics effects. If the Q-factor of the cavity is extraordinarily high (over  $10^8$ , in this case), the power within the cavity is sufficient to actually cause immobilized molecules to heat up. This heating will cause additional changes to the RI of the toroid. The thermo-optic coefficient of silica is positive, which means that increased temperature increases the resonant wavelength of the WGM, thus adding to the shift from the adsorbed molecule.

Regarding microfluidics, microtoroids suffer from similar problems to microspheres and planar ring resonators in that the fluid handling components must be individually fabricated and integrated. In the case where a fiber taper is used to couple to the WGMs, alignment is very delicate as optimal coupling will take place only at the exact “equator” of the toroid, where the WGM field energy is concentrated. The movement of fluid around this coupling system risks disturbing the alignment and corrupting the data. Another limitation is that analytes must bind to this same equator region in order to generate a large WGM response. If the binding takes place elsewhere closer to the hub, the WGM will be less sensitive, or even completely insensitive, to it [38]. Given the relatively small area of the high-sensitivity region on the toroid compared with its entire surface area, detection of ultra-low concentrations may be restricted.

### 1.3.6. Microfiber loop

Tapered silica optical fibers have often been used as in- and out-coupling waveguides for microspheres [33, 34], microtoroids [38, 41, 144] and microcapillaries [83, 90]. When pulled under heat to very small diameter, they are increasingly flexible and may be bent into extremely small radii of curvature without breaking. It has been shown, therefore, that they can easily be manipulated into microscale loops that act as ring resonators as shown in Fig. 1.15 [24, 150-161].

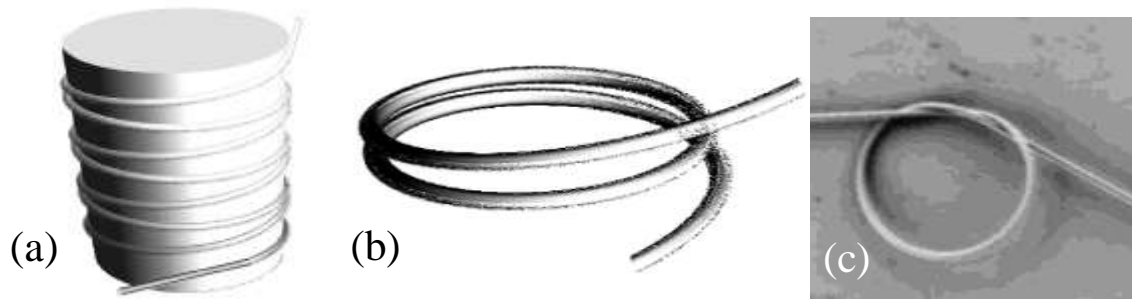


**Figure 1.15.** A coiled multi-loop resonator (a), double loop microfiber resonator (b), and microknot resonator (c). Reprinted with permission from Tong et al. (2003); Sumetsky (2004).

The very first demonstration of an optical-fiber-based ring resonator was in 1982, using a fiber 3 meters in length [162]. This fiber resonator was relatively weakly guiding and required a coupler of substantial dimensions, necessitating its immense size. Seven years later, an optical fiber was tapered down to  $8.5\ \mu\text{m}$  with a flame and arranged in a 2 mm loop [163]. By bringing the fiber into close enough proximity to itself, the loop was able to approximate a ring resonator. Contemporary microfiber resonators exhibit the benefits of stronger guiding due to high RI contrast and self-coupling [151]. It is now possible for a fiber loop to support moderately good Q-factors (on the order of  $1 \times 10^5$ ) at

diameters below 200  $\mu\text{m}$  [158], even down to 15  $\mu\text{m}$  [150]. At this size scale, the loops are well suited for compact integrated evanescent sensing. One method for this involves wrapping a 2.5  $\mu\text{m}$  fiber around a template rod (as in Fig. 1.15(a)) and embedding the whole assembly in polymer. This system has been employed with BRIS values as large as 40 nm/RIU, which is comparable to that of microsphere [154]. The use of an embedding polymer reduces somewhat the light-matter interaction that allows the ultra-high BRIS systems mentioned above.

Q-factors up to  $1 \times 10^6$  have been predicted for two-loop structures [151] (Fig. 1.15(b)). Due to the very small size of the fibers themselves (sub-micron in many cases) evanescent exposure to the surrounding media is quite extensive and thus the BRIS can be very high, up to 700 nm/RIU [155] with RI LODs predicted close to  $1 \times 10^{-7}$  RIU [156]. This excellent resolution makes them one of the more promising RI sensing platforms available today. Nonetheless, there has been little exploration of applications for RI sensing using microfiber loops. As a relatively new platform, there is much room for future investigation into this area.

In addition to the loop configuration, microfibers have also been arranged into microknots [150, 158, 160, 164] (Fig. 1.15(c)). The primary advantage of the microknot is that its assembly is much more stable compared to a loop held together by electrostatic and van der Waals forces [164]. Once drawn into a knot, the fiber will not accidentally straighten, even if drawn into a very tight radius. The best reported Q-factor for such a structure is  $5.7 \times 10^4$  in air [164], which is not as good as some other loop configurations because the self-coupling area where the fiber is twisted around itself is not conducive to

the highest efficiency coupling.

For microfluidic integration, fiber loops work excellently when embedded, because the alignment of the loops relative to each other is secured and they can be fashioned into a convenient tube-like geometry. Using a removable rod, the fiber is coiled and coated with a layer of ultra-low RI polymer like Teflon AF (RI = 1.29) [152, 153, 157]. The low RI of the Teflon helps to confine the WGM within the fiber while providing stability for the coil positions. Once the Teflon is cured, the rod can be removed and evanescent field of the fiber will extend into the resultant hollow core.

However, given the performance of such a configuration, there seems to be very little advantage of using it over microcapillaries. For outcoupling of the optical signal, however, the embedded fiber loop is superior as the delivery fiber is integrated into the ring itself.

As a review, Table 1.1 relates the significant performance parameters for each ring resonator platform discussed in this section as well as the LODs for some important analytes. While BRIS and Q-factor vary significantly between different configurations, the RI LOD (not published for all configurations) can be a good basis for comparison.

**Table 1.1.** Ring resonator characteristics and performance benchmarks

Platform	RI LOD	Q-factor	BRIS ( <sup>nm</sup> /RIU)	Analyte (LOD) – REF
Microsphere	$3 \times 10^{-7}$	$8 \times 10^9$	30	Virus InfA (10 fM) - [165]
Microdroplet	NA	$1.15 \times 10^5$	NA	NA
Toroid	NA	$2 \times 10^8$	NA	Heavy water (1 ppm) – [41]
Microcapillary	$5 \times 10^{-6}$	$1 \times 10^7$	37	DNA (10 pM) – [92]
Planar Ring	$1.8 \times 10^{-5}$	$4.5 \times 10^5$	141	Streptavidin (3pg/mm <sup>2</sup> ) – [106]
Slotted Planar Ring	$1 \times 10^{-4}$	$2.7 \times 10^4$	490	Acetylene gas (100%) – [123]
Microfiber Loop	$1 \times 10^{-7}$	$1 \times 10^6$	700	Isopropanol (1.5% v/v) – [154]
LRROS	$1 \times 10^{-6}$	$\sim 1.5 \times 10^4$	800	NA

#### 1.4. Selection of the OFRR for sensing applications

In the subsequent chapters, the opto-fluidic ring resonator (OFRR) is used to demonstrate detection of DNA hybridization and DNA methylation. As mentioned briefly in Section 1.3.3, cylindrical ring resonator geometries have shown compelling advantages for handling fluidics, simplifying the process of refractometric sensing.

As shown in Fig. 1.16, the OFRR has the distinct advantage of being able to effectively couple light through its outer wall, and simultaneously handle fluidics in the hollow core.

While the other ring resonator geometries described in Section 1.3 yield very interesting results and show incredible creativity, they all have a significant weakness in

common. Namely, the integration of fluidics for sample delivery is much more complicated [83]. For all other structures, construction of fluidic cells is a critical design consideration. Whereas the OFRR is inherently suited for delivering fluidics. In our experiments we can connect either end of the capillary to polymer tubing and control the flowrates with external pumps. This method is effective at conserving sample volume and ensures that it will be delivered directly to the sensing region.

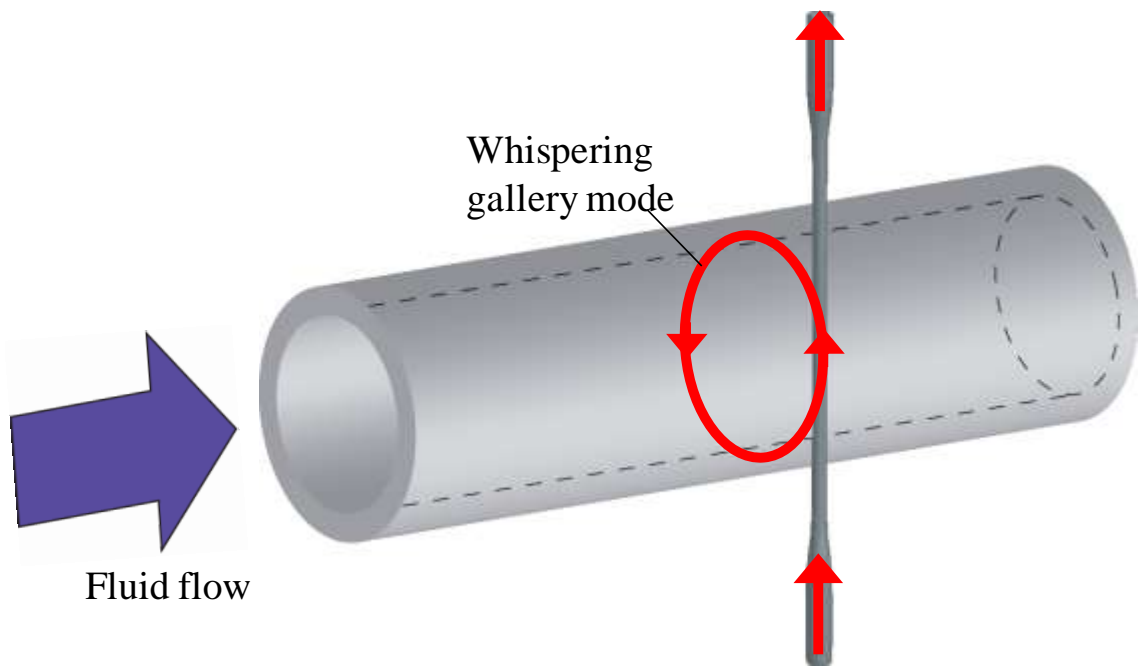


**Figure 1.16.** Conceptual illustration of the OFRR sensor, showing the relationship between photonics and fluidics made possible by this geometry.

The fundamental operating mechanism behind ring resonators has been thoroughly described in Section 1.2. In the coming pages however, design concerns and applications of OFRR will be discussed. As the reader will observe, the engineering

problems faced when tailoring the OFRR sensor to a particular use require very specific and individualized solutions.

## CHAPTER 2

### THERMAL CHARACTERIZATION OF THE OFRR

#### 2.1. Motivation for thermal characterization

In this chapter, we investigate experimentally and theoretically the temperature dependence of the OFRR to establish a noise baseline, which will enable us to implement a temperature stabilization mechanism to reduce the thermally induced noise and to improve the sensor detection limit. Thermal noise is one of the most significant limitations on the spectral resolution of the OFRR, so being able to model its effect is a critical first step in understanding how to reduce it.

Our studies involve analysis of the thermo-optic and thermomechanical effects of fused silica and aluminosilicate glass as they impact OFRR performance. Both thick-walled and thin-walled OFRRs are investigated to elucidate the contribution of water in the core to the thermal response of the OFRRs. Theoretical calculations based on Mie theory are used to verify the experimental observations.

Ring resonator sensors have been heavily investigated for sensing applications in recent years [21, 33, 34, 43, 50, 55]. They can quickly deliver quantitative and kinetic information without the complication of fluorescent labeling. Due to the label-free operating mechanism, they are simple to employ and can be relatively low cost.

Figure 2.1 illustrates the concept of the capillary based OFRR sensor array [Fig. 2.1(a)] and its sensing mechanism [Fig. 2.1(b)]. The capillary has an outer diameter of 50–100  $\mu\text{m}$  and a wall thickness of  $\sim 3\text{--}5$   $\mu\text{m}$ . The cross section of the capillary forms a

ring resonator that supports the circulation of photons in the form of whispering gallery modes (WGM), as shown in Fig. 2.1(b). Using thin-walled capillaries (i.e., a few micrometers), significant evanescent exposure can be produced in the interior of the OFRR, as illustrated in Fig. 2.2, which can be utilized for biological–chemical sensing when aqueous analytes are conducted through the capillary core. The circulation of the light enables repetitive light–analyte interaction, thus resulting in an effective sensing length much longer than the OFRR circumference. Such strong light–analyte interaction significantly improves sensor detection limit, which, together with submillimeter dimensions and the excellent fluid handling capabilities of the capillary, makes the OFRR a promising candidate for integration with advanced microfluidic techniques onto an arrayed lab-on-a-chip sensing system.

In addition to sensor development, the OFRR can also be used in capillary electrophoresis and chromatography. Compared with current capillary technology, the OFRR adds the function of on-capillary detection that permits sensitive, noninvasive, and quantitative measurement of analytes flowing in the core in real time. This on-capillary detection capability will be useful to extract flow profile information in capillary-based separation techniques.

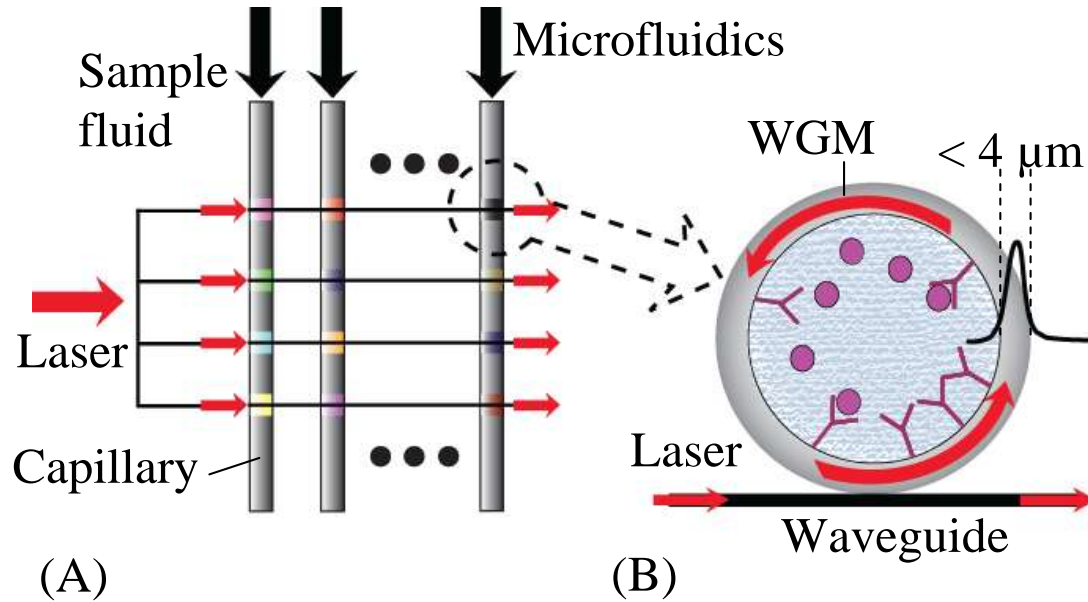


**Figure 2.1.** (a) Schematic of proposed two-dimensional OFRR sensor array. (b) Cross-sectional view of an OFRR sensor.

Measurements with the OFRR can be made using the effective refractive index change induced by the binding of analyte to the interior surface or by changes in the bulk solution in the core, which is manifested as a shift in the WGM spectral position [34, 83, 85]. Currently, OFRRs have been manufactured successfully, and the refractive index sensitivity has been characterized [83, 85]. A refractive index sensitivity of 51.9 nm/RIU (refractive index units) has been demonstrated for OFRRs [90]. This is of the same order as demonstrations for microsphere ring resonators [21]. Thus it is anticipated that OFRRs will have a detection limit similar to that of conventional microsphere-based sensors, which have shown a potential refractive index detection limit as low as  $10^{-7}$  RIU and a protein detection limit of 1–10  $\text{pg}/\text{mm}^2$  [21, 33, 43].

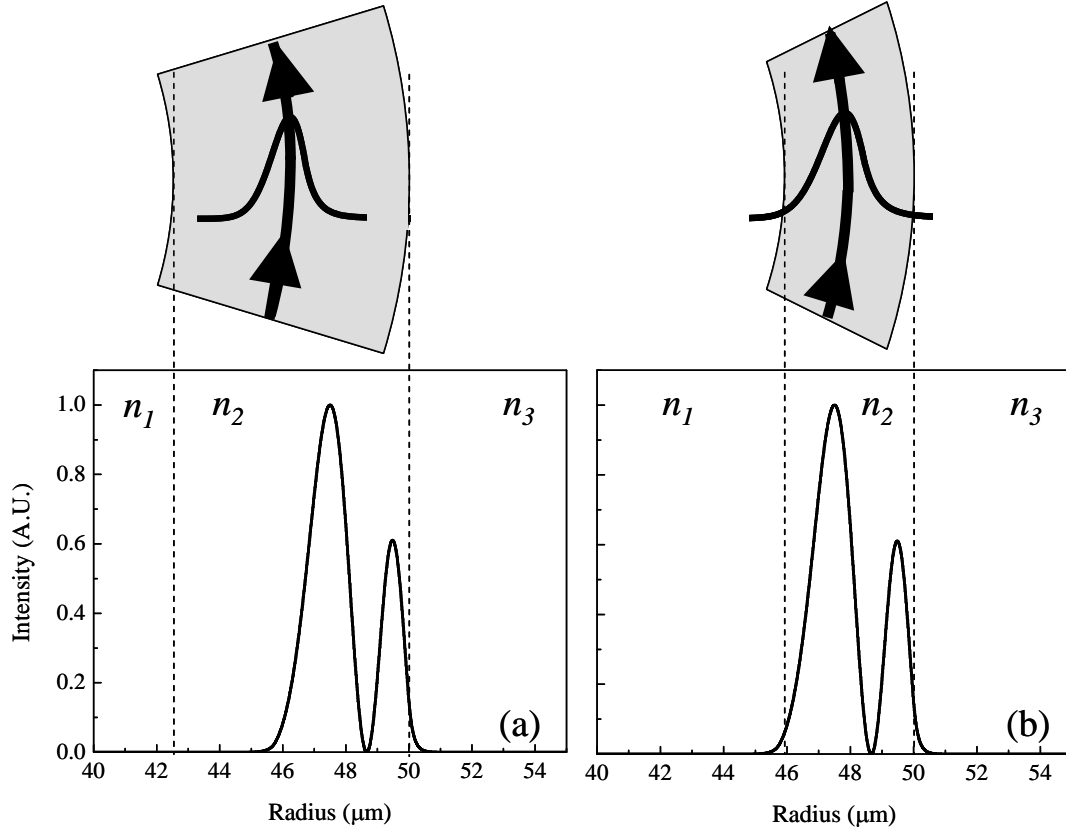


**Figure 2.2.** Intensity distribution of the second order radial WGMs for two different fused silica wall thicknesses shows that the wall needs to be sufficiently thin to expose the evanescent field to the core. Dashed lines show the interior and exterior surfaces of the OFRR. Refractive index:  $n_1=1.33$ ,  $n_2=1.45$ ,  $n_3=1.0$ .

Unfortunately, this potential is limited by the thermal noise. As with other types of label-free optical sensors, the sensing signal is inevitably convoluted by thermal effects. Thermal fluctuations produce changes in the refractive properties of both the OFRR material and the liquid solution and will also lead to changes in the OFRR size due to thermal expansion, both of which generate undesirable spectral variations in the WGM. The resulting spectral changes are added to the sensing signal as a noise term. In fact, in the case of the OFRR, thermal noise is by far the dominant term, and thus without

thermal control, this term is essentially the noise baseline. The two coefficients that define the magnitude of the noise term are the thermo-optic coefficient and the thermal expansion coefficient, which produce noise by affecting the resonant condition of the device. Furthermore, we assume that the core has the same optical properties as water, because for sensor development the buffer solution conducted in the OFRR is mainly composed of water [166, 167]. With filters as well as sensors, however, this tuning effect must be precisely controlled to prevent signal corruption. A degree of thermal noise is present in these devices that is determined by characteristic thermal sensitivity and limited by the degree of temperature control available. Therefore detailed thermal characterization of the OFRR is needed to establish the noise baseline as a foundation for further improvements. Furthermore, for many lab-on-a-chip applications, *in situ* temperature monitoring is highly desirable. A well-calibrated OFRR can also function as a sensitive thermometer capable of measuring the temperature along the OFRR.

In this chapter, we conduct both experimental and theoretical investigations to elucidate the thermal expansion and thermo-optic effects present in two commonly used capillary materials, fused silica and aluminosilicate glass. In particular, we study thick-walled and thin-walled OFRRs, where in the latter case, the thermo-optic contribution from water in the liquid core plays a significant role in the thermal response of the OFRR. Our experimental results are in good agreement with the theoretical analysis.

## 2.2. Impact of thermal effects in the OFRR

The contributions from thermal expansion and thermo-optic effects to the WGM shift can be understood in the framework of the resonant condition expressed in Eq. (1.1) in the previous chapter [21].

For a given WGM mode, the temperature-induced wavelength shift  $\Delta\lambda$  can directly be obtained from Eq. (1.1):

$$\frac{\Delta\lambda}{\lambda} = \frac{\delta r}{\delta T} \frac{1}{r} \Delta T + \frac{\delta n_{\text{eff}}}{\delta T} \frac{1}{n_{\text{eff}}} \Delta T \quad (2.1).$$

Note that the mode number denotations ( $m$  and  $l$ ) on the resonant wavelength are ignored for simplicity. The first term on the right side of Eq. (2.1) accounts for the OFRR thermal expansion effect and can be obtained from

$$\frac{\delta r}{\delta T} \frac{1}{r} = \alpha \quad (2.2)$$

where  $\alpha$  is the linear thermal expansion coefficient (in units of  $\text{K}^{-1}$ ). The temperature-induced effective refractive index change is described by the second term on the right side of Eq. (2.1). Similar to a three layer waveguide [168, 169],  $n_{\text{eff}}$  describes the WGM radial distribution among the core, the OFRR wall, and the air outside the OFRR, and thus has the following general formula:

$$n_{\text{eff}} = f(n_{\text{air}}, n_{\text{core}}, n_{\text{wall}}, t) \quad (2.3)$$

where  $t$  is the OFRR wall thickness, and  $n_{\text{core}}$ ,  $n_{\text{wall}}$ , and  $n_{\text{air}}$  are the refractive indices of the core, the OFRR glass material, and the air outside the OFRR, respectively. Furthermore, we assume that the core has the same optical properties as water, as for

sensor development, the buffer solution conducted in the OFRR is mainly composed of water. The variation of the effective refractive index with respect to temperature can be written as

$$\frac{\delta n_{eff}}{\delta T} = \kappa_{air} \frac{\delta n_{eff}}{\delta n_{air}} + \kappa_{core} \frac{\delta n_{eff}}{\delta n_{core}} + \kappa_{wall} \frac{\delta n_{eff}}{\delta n_{wall}} + \alpha_{wall} \frac{\delta n_{eff}}{\delta t} \quad (2.4)$$

where

$$\kappa_{air(core,wall)} = \frac{\delta n_{air(core,wall)}}{\delta T} \quad (2.5).$$

is the thermo-optic coefficient for air (core, wall).  $\alpha_{wall}$  is the linear thermal expansion coefficient for the wall as defined in Eq. (2.2). The first three terms on the right side of Eq. (2.4) take into account the thermo-optic effect of air, the OFRR wall, and the core, while the last term describes the effective refractive index change due to transverse expansion of the OFRR wall.

Equation (2.4) can further be simplified by applying some logical assumptions, which will provide physical insight into the OFRR response to temperature variations. First, as with an optical waveguide, a predominant portion of the light resides in the OFRR wall [168, 169]. Therefore we have

$$\begin{aligned} \frac{\delta n_{eff}}{\delta n_{core}} &\sim o(1) & \frac{\delta n_{eff}}{\delta n_{air}} &\sim o(1) \\ & & & \\ \frac{\delta n_{eff}}{\delta n_{wall}} &\sim O(1) & \frac{\delta n_{eff}}{\delta t} &\sim o(1) \end{aligned} \quad (2.6)$$

meaning that the effective refractive index is mainly determined by the refractive index of the wall and that  $\delta n_{\text{eff}}/\delta n_{\text{air}}$ ,  $\delta n_{\text{eff}}/\delta n_{\text{core}}$ , and  $\delta n_{\text{eff}}/\delta t$  are small in comparison to  $\delta n_{\text{eff}}/\delta n_{\text{wall}}$ , as changes in the air–core refractive index or the wall thickness will not significantly affect the effective refractive index. Furthermore, considering the relatively small thermo-optic coefficient of air ( $\kappa_{\text{air}} \sim 10^{-6} \text{ K}^{-1}$  at room temperature [170]), and the small linear thermal expansion coefficient for fused silica and aluminosilicate glass (of the order of  $10^{-6}$  and  $10^{-7} \text{ K}^{-1}$ , respectively [171]), the terms  $\kappa_{\text{air}}(\delta n_{\text{eff}}/\delta n_{\text{air}})$  and  $\alpha_{\text{wall}}(\delta n_{\text{eff}}/\delta t)$  can be ignored. As for the term  $\kappa_{\text{core}}(\delta n_{\text{eff}}/\delta n_{\text{core}})$ , we evaluate its contribution under the following two conditions. For thick-walled OFRRs, the fraction of the light in the core approaches zero [168, 169], so  $\delta n_{\text{eff}}/\delta n_{\text{core}}$ , and hence  $\kappa_{\text{core}}(\delta n_{\text{eff}}/\delta n_{\text{core}})$ , can be neglected. However, for the OFRRs used in our sensor development, the wall is sufficiently thin so that the amount of the light present in the core is no longer negligible. More importantly, because the thermo-optic coefficient for water is much larger than that of the wall [ $\kappa_{\text{water}} \sim -10^{-4} \text{ K}^{-1}$  versus  $\kappa_{\text{wall}} \sim 10^{-5} \text{ K}^{-1}$  [171, 172]], the term  $\kappa_{\text{core}}(\delta n_{\text{eff}}/\delta n_{\text{core}})$  must be taken into account, as it becomes comparable to  $\kappa_{\text{wall}}(\delta n_{\text{eff}}/\delta n_{\text{wall}})$  in magnitude. In fact, as discussed later, the thermo-optic effect of water contributes significantly to the WGM behavior under the thin-wall condition. After the above simplifications, Eq. (2.1) becomes

$$\frac{\Delta\lambda}{\lambda} = \alpha\Delta T + \frac{\delta n_{\text{eff}}}{\delta n_{\text{wall}}} \frac{\kappa_{\text{wall}}}{n_{\text{eff}}} \Delta T \quad (2.7)$$

for thick-walled OFRRs and

$$\frac{\Delta\lambda}{\lambda} = \alpha\Delta T + \frac{\delta n_{eff}}{\delta n_{wall}} \frac{\kappa_{wall}}{n_{eff}} \Delta T + \frac{\delta n_{eff}}{\delta n_{core}} \frac{\kappa_{core}}{n_{eff}} \Delta T \quad (2.8)$$

for thin-walled OFRRs.

To summarize, for the thick-walled OFRRs, the main sensing noise is from the combination of the thermal expansion and the thermo-optic effect of the OFRR wall material. For the thin-walled OFRR case, the thermo-optic effect of the water conducted in the core is a factor. It is important to point out that because water has a negative thermo-optic coefficient, the contribution from water mitigates the sensing noise induced by the other two effects, as shown later.

## 2.3. Experimental methods

### 2.3.1. Materials and fabrication

OFRRs are manufactured to two different specifications using two materials, fused-silica and aluminosilicate glass. These materials are purchased as capillaries with inner diameters (IDs) of 0.9 mm and outer diameters (ODs) of 1.2 mm from Sutter Instruments. The capillaries are then pulled under intense heat to reach an OD of approximately 100  $\mu\text{m}$ . The pulled OFRRs have a wall thickness of 8–10  $\mu\text{m}$ , which is thick enough that the evanescent field has negligible penetration into the core. To produce thin-walled OFRRs, the wall thicknesses must be 5  $\mu\text{m}$  or less such that the fraction of light in the core is large enough for sufficient sensing capability. Low concentrations of hydrofluoric acid solution (<10% volume-to-volume ratio) are

conducted through the thick-walled OFRR so that the inner surface can be etched to achieve this optimal thickness.

Thermal effects are measured using the setup shown in Fig. 2.3(a), which is designed to minimize convective and radiative thermal interactions between the OFRR system and the ambient environment. It is made of a horizontally aligned isolating tube wrapped in aluminum foil. A length of Kanthal heating filament is coiled against the inside and connected to a power supply. Temperature can be adjusted easily and accurately by raising or lowering the voltage across the heating filament. To monitor temperature in the OFRR, a thermocouple wire (Cole–Parmer) is inserted into one end of the OFRR and brought within 1 mm of the coupling region where the WGM is launched.

Figure 2.3(b) shows a photograph of the complete system. An optical fiber taper of a diameter of approximately 4  $\mu\text{m}$  is placed against the OFRR through a vertical slit cut in the isolating chamber and couples the light from a 1550 nm tunable diode laser into the OFRR. The laser scans across a spectral range of approximately 100 pm at a rate of 1–2 Hz, and a photodetector is used to monitor the light at the terminal end of the optical fiber. When the laser wavelength is on resonance with the WGM, the light is tapped into the OFRR and leaves a spectral dip at the fiber taper output, which is used to reveal the WGM spectral position [83]. The whole measurement system is controlled by a computer, and the WGM spectral position is recorded for post-analysis.

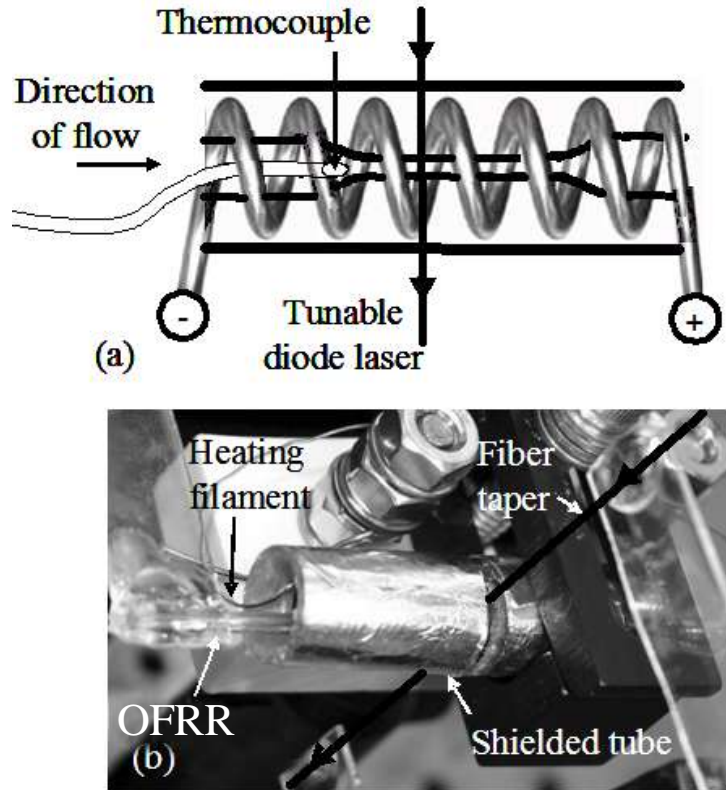


**Figure 2.3.** (a) Experimental setup. Aluminum foil covering provides a degree of thermal isolation. A Kanthal wire heating filament coils about the OFRR. Thermocouple is positioned within 1 mm of the coupling region defined by the fiber taper. Vertical line represents coupling fiber. (b) Photograph of the setup with OFRR and taper in place.

### 2.3.2. Thermo-optic characterization

To characterize the wall material properties without the influence of the liquid core, thick-walled OFRRs with a negligible amount of light in the core are employed first. The information obtained with the thick-walled OFRRs can be used to estimate thermo-optic coefficients for the two glasses, based on the simplifying assumption that the thermal behavior of the external and internal media has no effect on the WGM. Once derived, this parameter is then used for the characterization of the thin-walled OFRRs.

When gathering data on thin-walled OFRRs it is necessary to know the wall thicknesses. As mentioned, wall thickness is a crucial parameter that governs how much light is present in the core. While wall thickness can easily be determined with a microscope for thick-walled OFRRs, it is difficult to be precise with this method when the wall is just a few micrometers thick. Although scanning electron microscope imaging of the OFRR cross section can provide very accurate information about the wall thickness, it is time consuming and not suitable for daily OFRR characterization. We have developed a quick and cost-effective approach to get an accurate assessment of the wall thickness by measuring the refractive index sensitivity. This method requires passing various concentrations of ethanol solution through the OFRR. The changing refractive index of the core solution, due to the ethanol, shifts the WGM spectral position, as shown in Fig. 2.4(a). Collecting shift data allows assembly of a sensorgram like that shown in Fig. 2.4(b). This sensorgram is used to compose the line in Fig. 2.4(c), from which the OFRR sensitivity can be derived. Using a model based on Mie theory, the wall thickness can be deduced for a given refractive index sensitivity and OFRR OD. In addition, detailed analysis of the OFRR sensitivity has revealed that it is the second radial WGM that is used in our experiment [83].

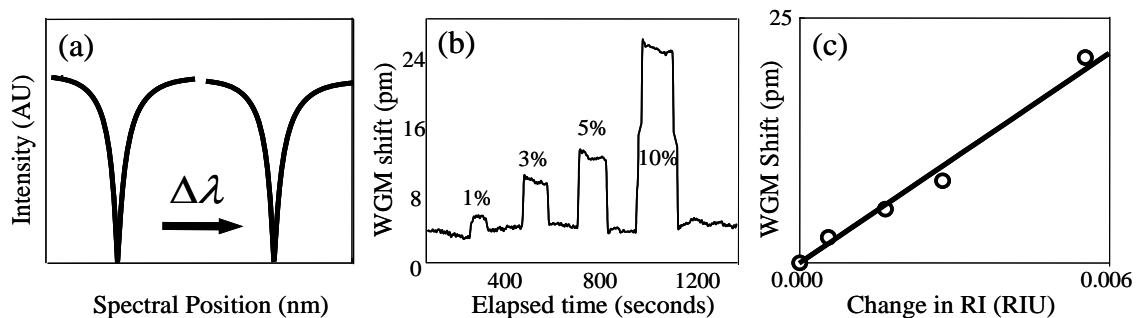


**Figure 2.4.** (a) A resonant mode shifts by  $\Delta\lambda$  when the refractive index of the core changes. (b) Refractive index sensitivity measurement using diluted ethanol in water (concentrations shown in figure) in a thin walled fused silica capillary with OD of 100  $\mu\text{m}$ . Baseline measurement is pure water. (c) Computed refractive indices versus spectral shift, where the slope is equal to refractive index sensitivity. Sensitivity in this example is 3.6 nm/RIU, corresponding to a wall thickness of 4.3  $\mu\text{m}$ .

For thermal characterization of OFRRs, they are inserted into the isolating chamber, and the temperature is incrementally increased by applying voltage across the heating filament. At each voltage step, the voltage is held constant until the temperature stabilizes to within  $\pm 0.1$  K. During data capture, the core of the capillary is filled with de-ionized water. Figure 2.5 is the resulting temperature-step graph, showing the absolute WGM shift above the baseline position over time. At each step, the temperature reading from the probe is indicated, and it can be seen that prior to each subsequent voltage step the spectral shift rate is virtually zero. These data are then used to plot temperature change versus WGM shift, the slope of which is the temperature-sensitivity constant for the resonant modes,  $\Delta\lambda/\Delta T$ .

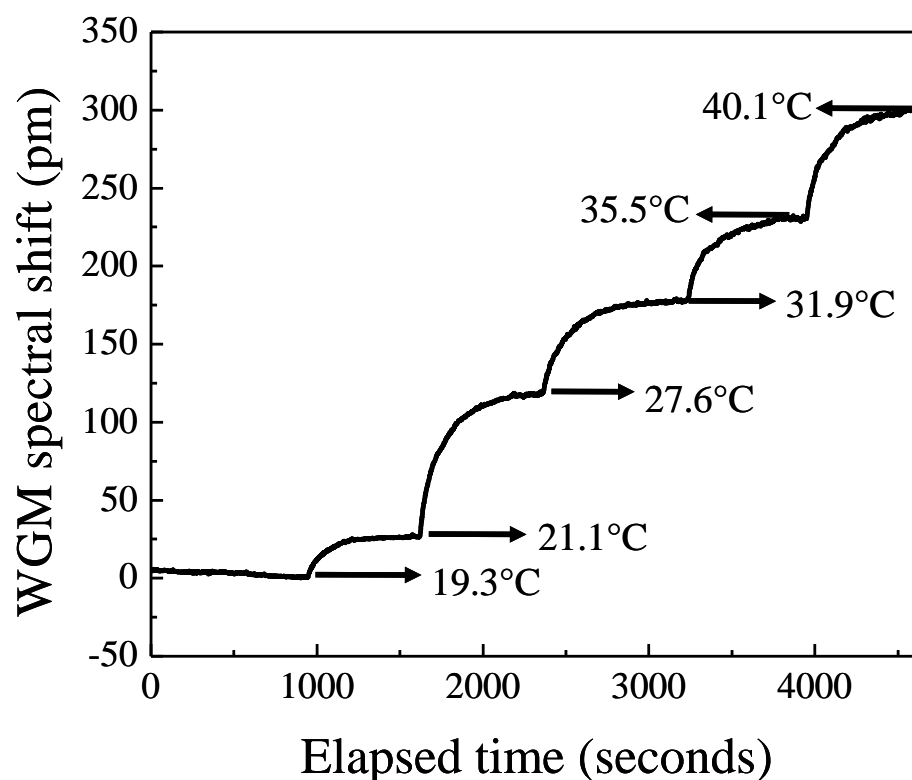


**Figure 2.5.** Example temperature step data for thin-walled aluminosilicate OFRR. Y-axis represents change from lowest mode position.

## 2.4. Results

The results of our temperature-sensitivity studies are presented in Fig. 2.6. Data are shown for fused-silica and aluminosilicate glass materials. Thick- and thinwalled cases for each material are also presented. The wall thicknesses for the OFRRs presented in Fig. 2.6 are 8 and 3.9  $\mu\text{m}$  for the thick- and thin-walled aluminosilicate, respectively, and 8 and 4.3  $\mu\text{m}$  for the thick- and thin-walled fused silica, respectively. The slopes of the lines presented in Fig. 2.6 are equivalent to the thermal sensitivity coefficients for the

OFRRs ( $\Delta\lambda/\Delta T$ ), which can be related to the thermal expansion and thermo-optic coefficients by Eqs. (2.7) and (2.8).

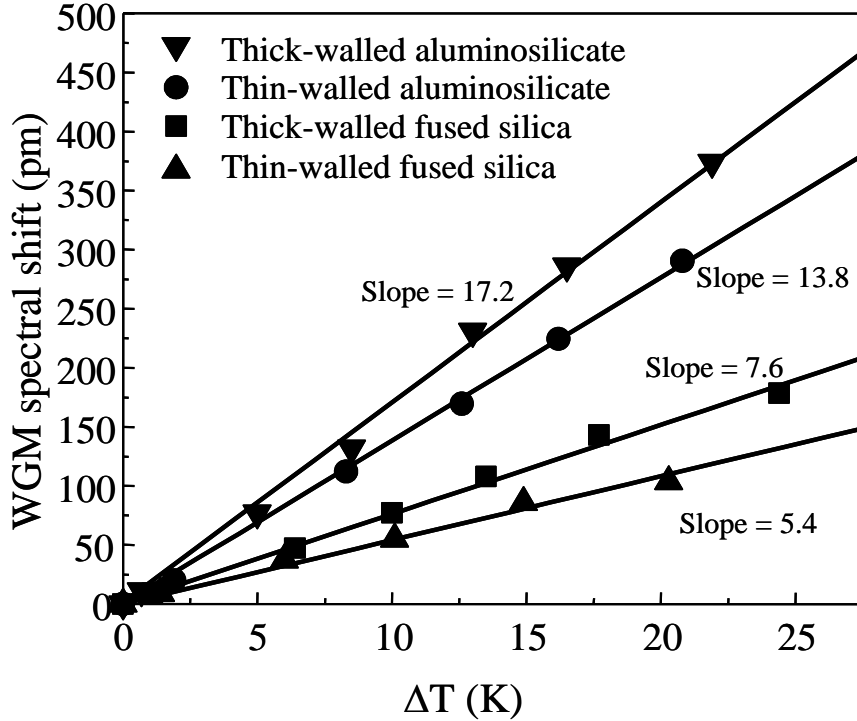


**Figure 2.6.** Comparative results for four different OFRRs: thick-walled aluminosilicate ( $\blacktriangledown$ ), thin-walled aluminosilicate ( $\bullet$ ), thick-walled fused silica ( $\blacksquare$ ), and thin-walled fused silica ( $\blacktriangle$ ), where slope of fitted lines indicates spectral shift per degree parameter ( $\Delta\lambda/\Delta T$ ). Thick-walled OFRRs have wall thickness of approximately 8  $\mu\text{m}$ , thin-walled OFRRs have wall thickness of approximately 4  $\mu\text{m}$ .

It is obvious that the slopes for aluminosilicate OFRRs are significantly higher than those for fused silica, since the thermal expansion coefficient for aluminosilicate ( $\sim 10^{-6} \text{ K}^{-1}$ ) is, in fact, an order of magnitude larger than that of fused silica ( $\sim 10^{-7} \text{ K}^{-1}$ ) [171]. This discrepancy is sufficient to counteract the aluminosilicate's lower  $\kappa$  and produce an overall higher sensitivity. Slopes for both materials, however, are observed to

decrease with thinner walls. This is because for the thin-walled OFRRs, the thermo-optic effect of the water in the core affects the  $\Delta\lambda/\Delta T$  due to an increased fraction of the light in the core. Because water has a negative  $\kappa$ , the net effect is a smaller  $\Delta\lambda/\Delta T$ .

Values for the thermo-optic coefficient for fused silica and aluminosilicate in the literature vary considerably [171, 173, 174], which is due to chemical composition, degree of crystallinity, fabrication processes, and handling of the materials used in each particular study. Typical values, however, are  $\sim 1 \times 10^{-5} \text{ K}^{-1}$  for fused silica and aluminosilicate glass. Using Eq. (2.7) and the thick-walled results, we are able to deduce the thermo-optic coefficients for fused silica and aluminosilicate glass, as presented in Table 2.1. In the process of calculating  $\kappa$ , the refractive indices of 1.55 and 1.45 are used for aluminosilicate and fused silica at 1550 nm, respectively [175]. Furthermore, we have assumed that  $\delta n_{\text{eff}}/\delta n_{\text{wall}} = 1$ , since for thick-walled OFRRs, a predominant portion of light is within the wall; therefore the effective refractive index is essentially equivalent to the refractive index of the wall. Presented in Table 2.1, our deduced thermo-optic coefficients are on the correct order of magnitude compared with values reported previously [171, 173, 174]. Comparing the thermal expansion and thermo-optic coefficients listed in Table 2.1, we can see that in aluminosilicate OFRRs, thermomechanic and thermo-optic effects make a comparable contribution to the OFRR thermal response, whereas in fused silica, the thermo-optic effect is the dominant factor.

**Table 2.1.** Derivation of  $\kappa$  from experimental results

OFRR type	$\alpha^a$	$\frac{\Delta\lambda}{\Delta T}^b$	Calculated $\kappa = \frac{dn}{dT}$
Thick aluminosilicate	$4.6 \times 10^{-6} \text{ K}^{-1}$	$17.2 \text{ pm K}^{-1}$	$1 \times 10^{-5} \text{ K}^{-1}$
Thick fused silica	$5 \times 10^{-7} \text{ K}^{-1}$	$7.6 \text{ pm K}^{-1}$	$6.4 \times 10^{-6} \text{ K}^{-1}$

<sup>a</sup>Values provided by manufacturer

<sup>b</sup>Values derived from Fig. 2.6

As mentioned, the thin-wall effect in OFRR sensor serves to reduce the overall temperature sensitivity due to a decreased effective  $\kappa$  from the contribution of water. We have analyzed this phenomenon using a calculation tool developed in-house. The tool uses Mie theory to describe the radial distribution of the WGM [176]:

$$E_{m,l}(r) = \begin{cases} AJ_m(k_0^{(l)} n_1 r) & (r \leq r_1) \\ BJ_m(k_0^{(l)} n_2 r) + CH_m^{(1)}(k_0^{(l)} n_2 r) & (r_1 \leq r \leq r_2) \\ DH_m^{(1)}(k_0^{(l)} n_3 r) & (r \geq r_2) \end{cases} \quad (2.9)$$

where  $J_m$  and  $H_m^{(1)}$  are the  $m$ th Bessel function and the  $m$ th Hankel function of the first kind, respectively. The refractive indices of the core, wall, and the surrounding medium are described by  $n_1$ ,  $n_2$ , and  $n_3$ . The terms  $r_1$  and  $r_2$  represent the inner and outer radius of the OFRR, respectively, and  $k_0^{(l)}$  is the amplitude of the wave vector in vacuum for the  $l$ th order radial WGM. Given an OD, ID, refractive index for the glass, core, and surrounding environment, and the angular momentum term, the tool can compute the spectral position of the WGM of any radial mode.

To analyze the shift in spectral position with temperature change, the model is designed to incrementally adjust the outer and inner radii for thermal expansion while also incrementally modifying the refractive indices of the glass, liquid core, and air surroundings. The incremental adjustments are based on the values of  $\alpha$ ,  $\kappa$ , and an assumed temperature step.

## 2.5. Theoretical model

Figure 2.7 presents a model of the predicted  $\Delta\lambda/\Delta T$  values for both thick- and thin-walled OFRRs with fused silica and aluminosilicate glass, where  $\Delta\lambda/\Delta T$ , as before, is equivalent to the slope of the plotted lines. The power of this analytical tool is that it allows us to corroborate our data based on the similarity of predicted and observed wall thicknesses. In the calculations, the values of  $\kappa$  and  $\alpha$  presented in Table 2.1 are used. The values of the refractive indices used are 1.0 for the air outside the OFRR, 1.45 for fused silica, 1.55 for aluminosilicate glass, and 1.33 for the liquid core (primarily composed of water). The value of  $\kappa$  for water is  $\sim 1.0 \times 10^{-4} \text{ K}^{-1}$  [172]. For the thick- and thin-walled cases, 7.5 and 3.5  $\mu\text{m}$  walls are used, respectively. The OFRR OD is kept at 100  $\mu\text{m}$  for all cases. According to Fig. 2.7, the slopes are 17 and 16  $\text{pm K}^{-1}$  for thick- and thin-walled aluminosilicate, respectively, and 8.3 and 6.3  $\text{pm K}^{-1}$  for thick- and thin-walled fused silica, respectively. We observe, however, that the simulation predicts a greater reduction in temperature sensitivity for fused-silica devices than aluminosilicate devices. This is because of the difference in the refractive index of the two materials. The aluminosilicate glass, having a higher refractive index, confines light within the glass to a

much greater extent. The fractional intensity of light in the core is of the order of  $1 \times 10^{-5}$  for aluminosilicate, as compared with  $1 \times 10^{-3}$  for fused silica. For this reason, the  $\kappa$  of water contributes less to the effective refractive index of the aluminosilicate OFRRs.

The horizontal line in Fig. 2.7 shows an extreme case where the wall thickness has been reduced until the thermo-optic effect of water completely compensates for the thermal expansion and the thermo-optic effect of the OFRR glass wall. Because of the different  $\alpha$ 's and  $\kappa$ 's for each wall material, the wall thicknesses required to satisfy this condition are different. At this point, the OFRR has the least susceptibility to the temperature fluctuations. As light confinement is greater in aluminosilicate, a thinner wall is needed. The wall thicknesses required are  $1.7 \mu\text{m}$  for aluminosilicate and  $2.6 \mu\text{m}$  for fused silica.

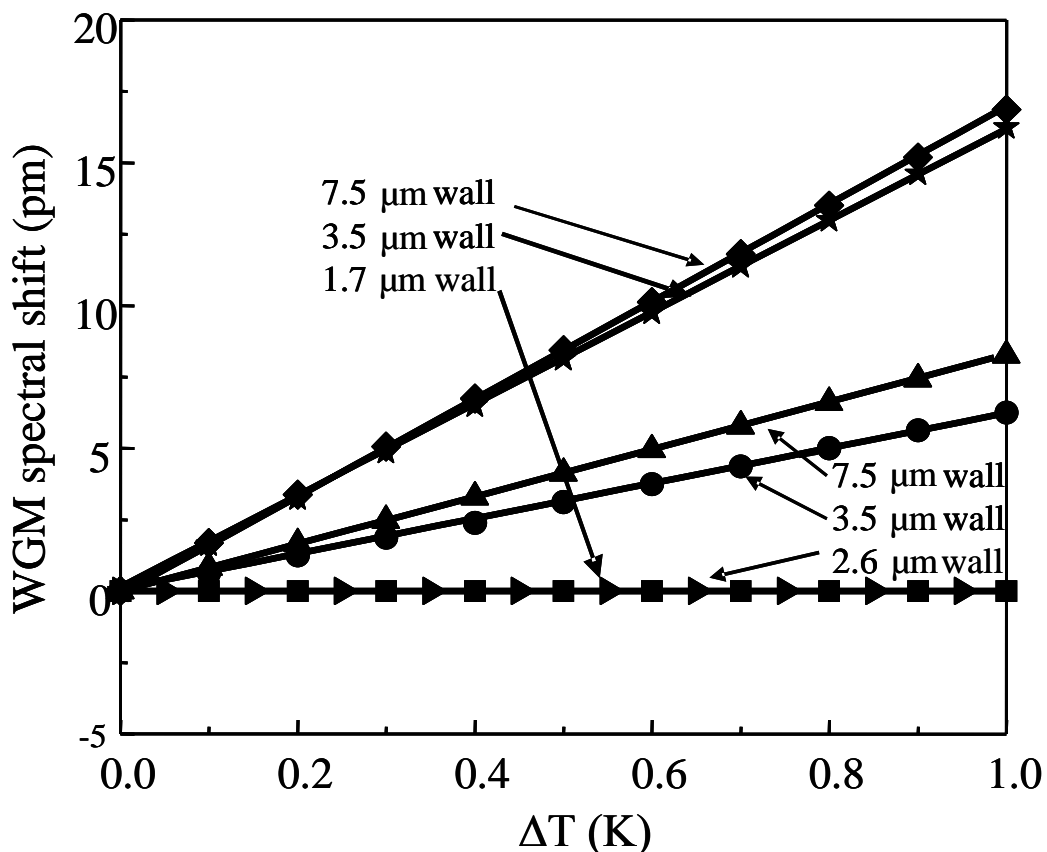


**Figure 2.7.** Simulation of spectral response to temperature change for 100  $\mu\text{m}$  OD thick-walled ( $\blacklozenge$ ) and thin-walled ( $\blackstar$ ) aluminosilicate, thick-walled ( $\blacktriangle$ ) and thin-walled ( $\bullet$ ) fused silica, and zero-sensitivity fused silica ( $\blacktriangleright$ ) and aluminosilicate ( $\blacksquare$ ) OFRRs using reported thermal expansion coefficient,  $\alpha$ , and experimentally determined thermo-optic coefficient,  $k$ . The values of the constants used are listed in Table 2.1.

It is worth noting that different solvent systems would provide different degrees of thermo-optic compensation. Most conventional polar and nonpolar solvents have large negative  $k$ s, so this compensation effect would likely be observed in virtually any biochemical assay. For instance, ethanol and methanol both have  $k$ 's of approximately -3.9

$\times 10^{-4} \text{ K}^{-1}$  [177]. A comparative examination of these solvent properties, however, is beyond the scope of this paper.

## 2.6. Conclusions

In this chapter, we have presented a thorough temperature-dependence calibration technique for the OFRR. We have also described a method for modeling this complicated resonating sensor system using Mie theory. Our experiments show that the OFRRs based on fused silica and aluminosilicate glass have a thermal dependence of the order of  $10 \text{ pm K}^{-1}$ , and that the thermal response for fused silica is much smaller than aluminosilicate because of its smaller thermal expansion coefficient. Furthermore, the OFRR system exhibits unique temperature-related noise control capability through the effect of the negative thermo-optic coefficient of water. As opposed to conventional ring resonators such as microspheres, the thermal noise can be reduced by adjusting the OFRR wall thickness, which can be exploited in future OFRR sensor development.

Our results are also important in OFRR detection limit estimation. A  $Q$  factor of  $1 \times 10^6$  can regularly be obtained in OFRRs, which corresponds to a linewidth of  $1.5 \text{ pm}$  at  $1550 \text{ nm}$  and generally yields a spectral resolution of approximately  $0.05 \text{ pm}$  [21, 34]. Assuming the thermal noise level is  $5 \text{ pm K}^{-1}$ , a thermal stability of  $0.01 \text{ K}$  is needed in order for the OFRR to fully realize its spectral resolving power, which, based on the sensitivity of  $51.9 \text{ nm/RIU}$  achieved in previous studies [90], results in a detection limit of  $1 \times 10^{-6} \text{ RIU}$ .

The implication of this work is that in future studies using the OFRR sensors, wall thinning techniques will be improved upon, allowing for better sensitivities and noise control. Better temperature control devices, such as thermoelectric cooling units, will be implemented, making the OFRRs applicable to a diverse variety of assays.

## CHAPTER 3

### FUNDAMENTAL DNA DETECTION WITH THE OFRR

#### 3.1. Background and introduction

Highly specific DNA detection is very important in many applications including medicine [178, 179], food safety [180] and forensic studies [181]. Currently, the most popular method is fluorescent microarray technology [182, 183]. However, quantitative analysis of DNA has been challenging due to the fluorescence signal bias, as the number of fluorophores on each DNA target molecule cannot be precisely controlled [184]. Furthermore, microarrays do not offer real-time signal acquisition, and thus kinetic information that can be used to reduce the false positives is lost. Optical label-free detection of analytes in their native forms has been under intensive investigation to address the limitations in microarrays [185, 186]. Most label-free systems also allow real-time data collection for kinetic analysis. A notable type of label-free sensor is the surface plasmon resonance (SPR) sensor [187, 188], which is exemplified by the instruments commercialized by both Biacore and Spreeta.

Recently, very sensitive planar waveguide-based [110, 117] and stand-alone microsphere-based [33, 34] ring resonator biosensors have been demonstrated. In fact, a detection limit of 6 pg/mm<sup>2</sup> for hybridization-based DNA detection has been achieved using microsphere ring resonators [33].

While microsphere-based sensors exhibit high  $Q$ -factor ( $>10^6$  in water) [33, 34] and low detection limit, fluidic integration, mass production, and reproducibility are extremely difficult, as has been noted in Chapter 1. On the other hand, planar ring

resonators can be mass-produced relatively easily through lithographic or imprint technologies, but they suffer from relatively low  $Q$ -factor ( $10^4$  in water) [110, 117]. Furthermore, incorporation of fluidics is very challenging, as the fluidics needs to be fabricated separately and then mounted onto ring resonator sensors through multiple steps.

### **3.2. Sensor platform**

Fig. 3.1(A) displays a schematic of the OFRR sensing mechanism. Fig. 3.1(B) displays the entire OFRR mounted in its experimental setup. The OFRR utilizes a glass capillary as a microfluidic channel and its circular cross-section forms the ring resonator that supports the WGM. The capillary wall is sufficiently thin (2–4  $\mu\text{m}$ ) so that the evanescent field of the WGM is present in the core and interacts with the analyte near the OFRR interior surface when the sample is passed through the capillary [83]. This internal surface sensing is a unique feature that enables advanced photonic integration because the fluid is conducted through the inside of the capillary while the optical interface is on the outer surface, as shown later.

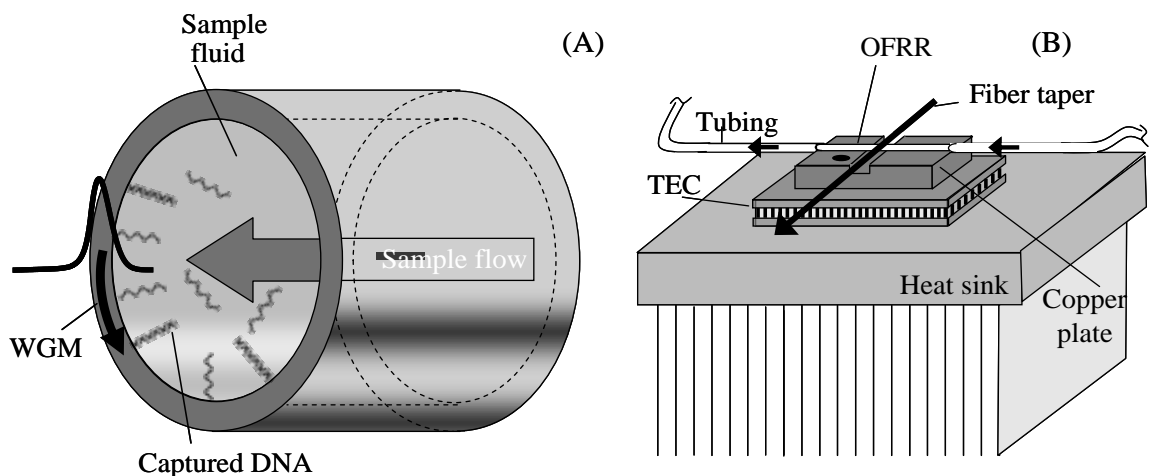


**Figure 3.1.** (A) Cross-sectional diagram of an individual OFRR sensor. (B) Side view of the experimental setup.

The performance of the OFRR has been described in the previous chapters. Briefly, when biomolecules attach to the OFRR interior surface, the RI near the OFRR surface changes, and thus the WGM resonant wavelength changes. Therefore, the temporal response of the WGM spectral position conveys the quantitative and kinetic information regarding the biomolecule binding to the OFRR surface.

Additionally, since each ring along a capillary can be as short as a few tens of microns [189], sub-nL detection volume per ring resonator can be achieved. It also benefits from reduced diffusion times due to small dimensions and large surface-to-volume ratio resulting from the circular fluidic channel. Furthermore, the OFRR can potentially be scaled up into a two-dimensional array for multiplexed detection. It is estimated that thousands of ring resonator sensors can be packed onto a  $1 \text{ cm}^2$  chip. This sort of array will provide a promising and complementary technology to traditional fluorescence-based DNA microarrays.

In this chapter, we introduce a protocol for OFRR DNA hybridization assays. Furthermore, the OFRR response (WGM spectral shift) to various DNA samples was experimentally and theoretically analyzed in order to evaluate DNA detection capability of the OFRR. We know that the OFRR is able to detect DNA concentrations down to 10 pM. It has also been estimated that we can detect as little as 4 pg/mm<sup>2</sup> mass density on the OFRR surface. Compared to other label-free technologies this performance is quite comparable. DNA studies with localized SPR on gold nanoparticles have demonstrated best limits of detection (LOD's) of 10 pM and ~100 fg/mm<sup>2</sup> [190]. Evanescent waveguides have yielded LOD's of 300 pM [191] and protein surface densities as good as 20 fg/mm<sup>2</sup> [192]. Base-mismatched DNA hybridization was also investigated through the net spectral shift and kinetic response of the WGM. Our results will provide insight into the interaction between biomolecules (specifically DNA) and the WGM and will lay a solid foundation for future label-free DNA microarray development.

### **3.3. Experimental methods**

#### **3.3.1. Materials**

Reagents used in this study included 98% ethanol, 12M HCl, anhydrous methanol, 48% hydrofluoric acid (HF), and 3-aminopropyltrimethoxysilane (3-APS), all obtained from Sigma–Aldrich. 3xSSC running buffer was produced in-house using 0.45 M NaCl and 0.045 M sodium citrate in purified water. Homobifunctional amine-reactive crosslinking agent dimethyl adipimidate (DMA) was obtained from Aldrich. 18 M $\Omega$  water purified by an Easypure-UV system from Barnstead was used in all solutions.

Glass capillaries were purchased from Sutter Instruments. All DNA samples used in the experiments were custom strands made by Sigma Genosys and were designed specifically to reduce the probability of secondary structure formation using online mfold software (Rensselaer Polytechnic Institute) [193]. The aminated probe strands designed in this manner had the sequence, ‘5-NH<sub>2</sub>-C<sub>6</sub>-CCA ACC AGA GAA CCG CAG TCA CAA T-3’.

For the purpose of mismatch discrimination the target sequence was modified in the following way, with bolded letters indicating mismatched nucleotides:

- 1-base mismatch: ‘5 -ATT GTG ACT GCG **CTT** CTC TGG TTG G-3’
- 2-base mismatch: ‘5 -ATT GTG ACT **CCG CTT** CTC TGG TTG G-3’
- 5-base mismatch: ‘5 -ATT GTG ACT **CGG CAA** CTC TGG TTG G-3’

For experiments using longer targets, a 50-mer was ordered with a sequence of ‘5-ATT GTG ACT GCG GTT CTC TGG TTG GAC TTG TGA CTG GCT TCT ATG GTT GG-3’ and a 100-mer was ordered with a sequence of ‘5-ATT GTG ACT GCG GTT CTC TGG TTG GAC TTG TGA CTG GCT TCT ATG GTT GGA TTG TGA CTT CGG TTC TCT GGT TGG ACT TGT GAC TGG CTT CTA TGG TTG G-3’. The first 25 bases are identical in all three strand lengths so that the same probe length and sequence may be used for each experiment.

### 3.3.2. Sensor fabrication

An OFRR of 100  $\mu\text{m}$  in outer diameter (OD) was fabricated by pulling a quartz capillary under intense heat ( $\sim 2000^\circ\text{C}$ ) followed by HF etching from inside, as has been detailed in previous work [83, 189]. Then the OFRR's and optical fibers were mounted orthogonally on the sensor platform as shown in Fig. 3.1(B). The OFRR was fixed onto a copper plate ( $1\text{ cm}^2$ ) that, in turn, sat on top of a thermo-electric cooler (TEC) unit (Marlow Industries, Inc.) connected to a temperature controller (ILX Lightwave). A thermister was embedded in the copper plate near the coupling region with thermally conductive epoxy (Arctic Silver). A custom fitted acrylic cap was placed on top of the copper plate to protect the system from air current disruption. Fluidic delivery was handled by a syringe pump (Harvard Apparatus) and Tygon tubing. All experiments were performed at room temperature ( $\sim 25^\circ\text{C}$ ).

The WGM was launched inside the circumference of the OFRR with the 1550 nm tunable diode laser (JDS Uniphase) scanned across a range of 100 pm at a scanning rate of 2 Hz. Light was guided to the OFRR with a single-mode optical fiber that was tapered to approximately 3  $\mu\text{m}$  in diameter at the coupling location. At its output, the fiber was directed at a photodetector to collect a spectral intensity dataset. When the laser wavelength is on resonance with the WGM, a spectral dip was observed at the fiber output, indicating the WGM spectral position [87]. The  $Q$ -factor for the WGM, which was deduced from the full-width at the half maximum of the resonance dip, was approximately  $10^6$  [85].

### **3.3.3. BRIS measurement**

Prior to DNA detection, the BRIS was measured to noninvasively estimate the OFRR wall thickness. In addition, the BRIS also provides vital information for the deduction of the DNA molecule density on the surface, as discussed later. During the characterization, progressively higher concentrations of ethanol in water were injected into the OFRR, causing small increases in the fluid's RI. The WGM shifted to a longer wavelength in response to the RI increase in the core. A BRIS of 6.8 nm/RIU was then obtained by measuring the slope of the WGM shift versus the RI change (presented in Fig. 3.2). This sensitivity corresponds to a wall thickness of approximately 4  $\mu\text{m}$ , based on the theoretical model that we developed earlier [83, 87].

### **3.3.4. Experimental protocol**

To begin the experiment, the HF-treated OFRR was rinsed with a 1:1 HCl:methanol mixture for 30 min, followed by the rinse with methanol. 3 $\times$  SSC buffer, the running buffer for the entire experiment, was subsequently pumped through the OFRR at a volumetric flow rate of 15  $\mu\text{L}/\text{min}$  for 10–15 min. This establishes the detection baseline for subsequent WGM spectral shift measurements. Then, 1% 3-APS in 3 $\times$  SSC buffer was run through the OFRR for 30 min at 15  $\mu\text{L}/\text{min}$ .

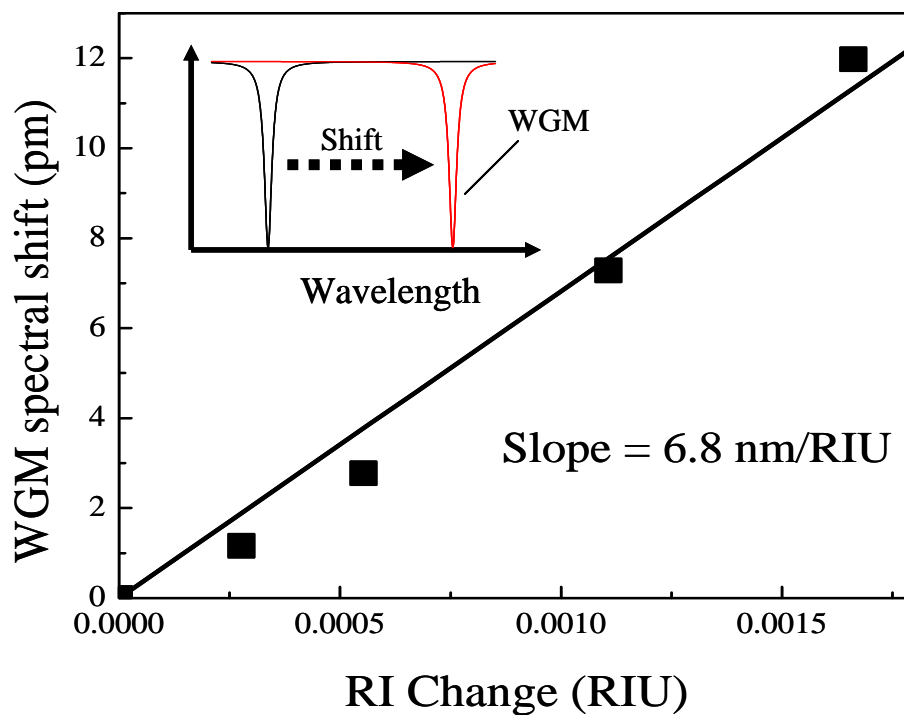


**Figure 3.2.** BRIS of 6.8 nm/RIU for the OFRR. Inset: WGM spectral shift when the RI changes in the core.

After this and each subsequent step, 3xSSC rinse was employed to remove the non-specifically bound molecules. Next, 10  $\mu\text{M}$  of the 25-base DNA probe and 5 mg/mL DMA were mixed in 3xSSC and pumped through for 1 h to crosslink aminated probes to the OFRR surface. Finally, the OFRR was filled with 3xSSC and ready for the detection of target DNA. After DNA detection, the OFRR could be regenerated by running low concentration of HF to etch off the deposited DNA and 3-APS molecules.

Because of the real-time data acquisition capabilities of the OFRR, each stage in the experiment may be monitored, from the amine-functionalization through target DNA hybridization. Figure 3.3 plots the sensorgram for the surface activation described in the

previous section and for the subsequent detection of a positive control target strand (25-base complementary DNA).

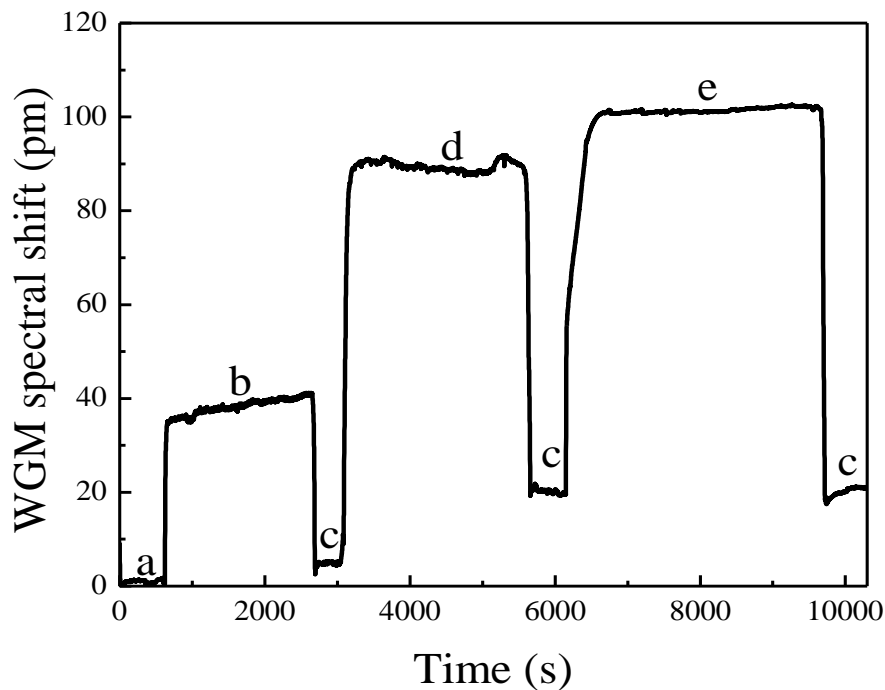


**Figure 3.3.** Sensorgram for OFRR surface activation and 25-mer complementary target DNA detection. a: initial baseline; b: 3-APS modification; c: buffer rinses with 3x SSC; d: amine-modified probe DNA incubation; e: target DNA incubation.

The total WGM shift at the beginning of each activation phase is caused additively by real and non-specific binding of reactant molecules to the OFRR surface and by small changes in the bulk RI of the core fluid due to dissolved materials. The nonspecific binding and the bulk RI change can be removed by rinsing the OFRR with 3xSSC buffer, as indicated by the downward shift in the WGM spectral position. Consequently, the net WGM shift corresponds to predominant contribution from the actual binding and small

portion of non-specific binding that could not be rinsed off. Based on Fig. 3.3, the net WGM shift for the 25-mer probe was 21 pm.

### **3.4. Results**

Fig. 3.4(A) explores the OFRR detection capability of distinguishing target DNA molecules of different strand lengths (25-mer, 50-mer, and 100-mer). The concentration of all DNA samples are 10  $\mu\text{M}$  to ensure that the saturation WGM shift was reached. The WGM shifts were measured by comparing the post-rinse WGM position with the pre-target position, yielding a net shift value. Clearly, saturation signal values in Fig. 3.4(A) do not behave linearly with strand length. This is explainable by pointing out the increased likelihood of steric effects with longer nucleotide chains. This effect is quantitatively investigated in Table 3.1.

**Table 3.1.** WGM shift and surface coverage data for various DNA samples.

<b>DNA sample</b>	<b>Net <math>\delta\lambda</math> at 10 <math>\mu\text{M}</math> (<math>\mu\text{m}</math>)</b>	<b>Surface density (molecules/<math>\text{cm}^2</math>)</b>	<b>Fractional coverage</b>
25-mer aminated DNA probe	21	$3 \times 10^{13}$	51%
25-mer complementary target	10.9	$1.5 \times 10^{13}$	26%
25-mer 1-base mismatch target	9.6	$1.3 \times 10^{13}$	23%
25-mer 2-base mismatch target	8.1	$1.1 \times 10^{13}$	20%
25-mer 5-base mismatch target	0.56	$0.077 \times 10^{13}$	1.4%
25-mer 25-base mismatch target	0.41	$0.056 \times 10^{13}$	1%
50-mer complementary target	16.4	$1.23 \times 10^{13}$	22%
100-mer complementary target	20.5	$0.7 \times 10^{13}$	12%
25-mer aminated DNA probe (reduced density)	12	$1.7 \times 10^{13}$	29%
25-mer complementary target (with reduced probe density)	5.1	$0.72 \times 10^{13}$	12%

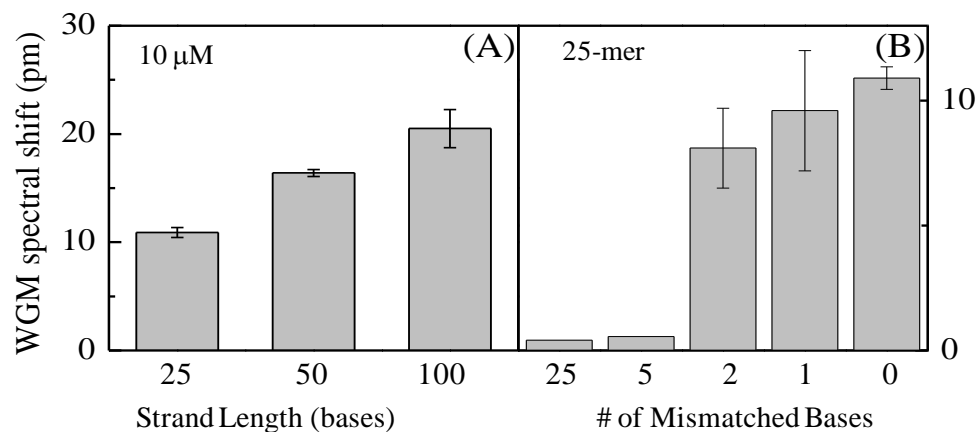


**Figure 3.4.** Net WGM shift for various DNA strand lengths (A) and for various mismatches at the same 10  $\mu\text{M}$  concentration (B). Hybridizations performed at 25°C in 3 x SSC buffer. Displayed standard deviations are 0.45 pm, 0.32 pm, and 1.77 pm for 25-, 50-, and 100-mers, respectively (A), and 1.6 pm, 2.41 pm, and 0.45 pm for 2-base, 1-base, and complimentary target (B).

Note that the quantitative comparisons in DNA strand length can only be achieved with this label-free detection. In fluorescence-based DNA microarray, the strand length information is lost and concentration estimation may be skewed due to the errors in fluorophore labeling. Fig. 3.4(B) investigates the OFRR's capability of detecting base-mismatched target DNA. In this experiment, various target DNA samples ranging from zero-base-mismatch (complementary DNA, positive control) to 25-base-mismatch (negative control) were used. All the DNA samples had the same strand length (25-base) and concentration (10  $\mu\text{M}$ ). With the increased mismatched bases, the net WGM shift drops gradually. For the single- and double-base mismatch targets, the difference in the net WGM shift is 1.3 and 2.8 pm, respectively. Although small, these differences are well within the system resolution capability ( $\sim 0.02$  pm). Presently, the large standard

deviation in this data makes repeatability a challenge, but subsequent work has already shown promise for improvement in this area. Given that the hybridizations were performed at room temperature, the conditions are far from optimized and there is reason to believe that this base-mismatch resolution could be improved. In fact, previous literature has demonstrated that buffer salt concentration can be adjusted to achieve as much as a 10 to 1 signal discrepancy between matched and single base-mismatched strands [33]. A significant decrease in the WGM net shift was observed when five or more bases are mismatched.

The results obtained in Fig. 3.4(B) can further be exploited in designing DNA assays to analyze the composition of mixed solutions of complementary and mismatched target strands, which has many important research and clinical applications such as DNA methylation studies in cancer patients [179, 194, 195]. Fig. 3.4(B) indicates that the detection signal, *i.e.*, the net WGM shift, is small for 5-base-mismatch DNA, as compared to that for complementary DNA. Therefore, the OFRR should be able to clearly discriminate among mixed solutions of complementary and 5-base-mismatched target strands

Figure 3.5 shows good linearity ( $R^2 = 0.946$ ) is obtained for various fractional compositions of the complementary strands. The regression line on this figure has a slope of 0.89667 (forced through the origin). Note that with zero complementary bases, we still see a small shift due to the contribution from the 5-base mismatched DNA, as discussed earlier.

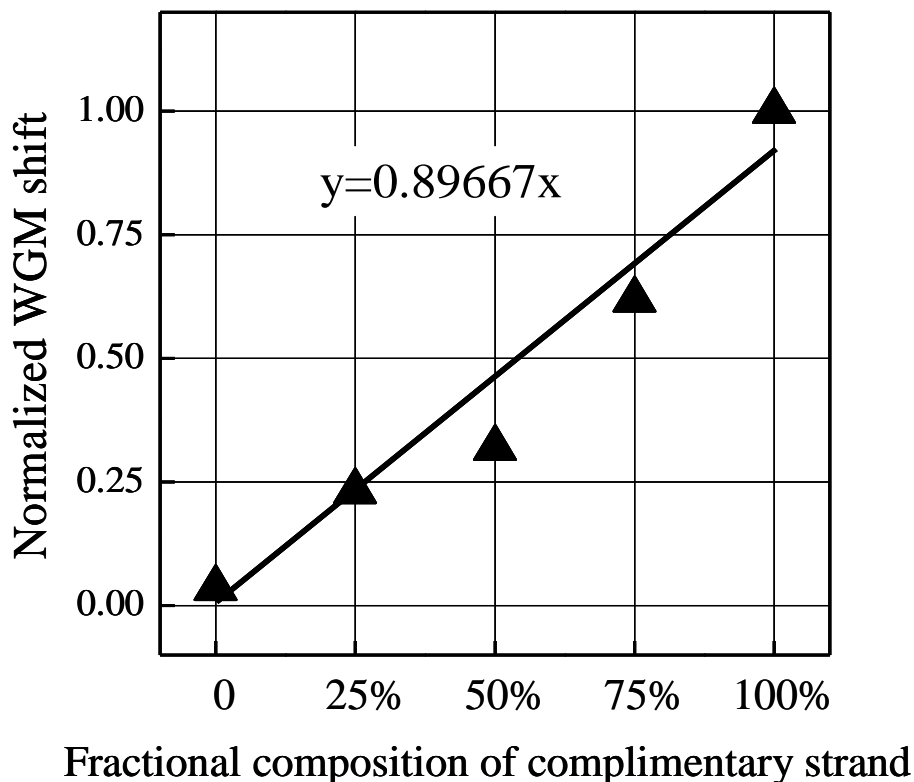


**Figure 3.5.** Normalized net WGM shift as a function of the fractional composition of the complementary target DNA. DNA mixtures contain 25-mer complementary DNA and 5-base-mismatched 25-mer DNA. Total concentration: 10  $\mu$ M.

In addition to the net WGM shift, kinetic information can also be used to distinguish the base-mismatched DNA. Fig. 3.6(A) shows the binding curves for completely matched, 2-base mismatched, 5-base-mismatched, and completely mismatched target 25-mer DNA strands. Although the final saturation WGM shift the three target DNA samples are close, their kinetic behavior is quite different. We can examine and model hybridization curves for DNA using a first-order Langmuir model for diffusion-limited interaction [196]:

$$\Gamma(t) = \Gamma_o [1 - \exp(-kt)] \quad (3.1)$$

where  $\Gamma(t)$  is the sensor response signal as a function of time,  $t$ , and  $\Gamma_o$  is the final signal plateau.  $k$  is the reaction rate constant (in units of  $s^{-1}$ ) – which involves both hybridization and non-specific adsorption – and is plotted in Fig. 3.6(B) against the fraction of complementarity, which is defined as the fraction of DNA in the target strand that are complementary to the immobilized probe. Fig. 3.6(B) also shows an exponential fit to the rate constant, which demonstrates the high resolving power of kinetic analysis at low-mismatch (or high complementarity) values. This is very useful to reduce false positives when differentiating complementary DNA sample from those with only a few mismatched bases.

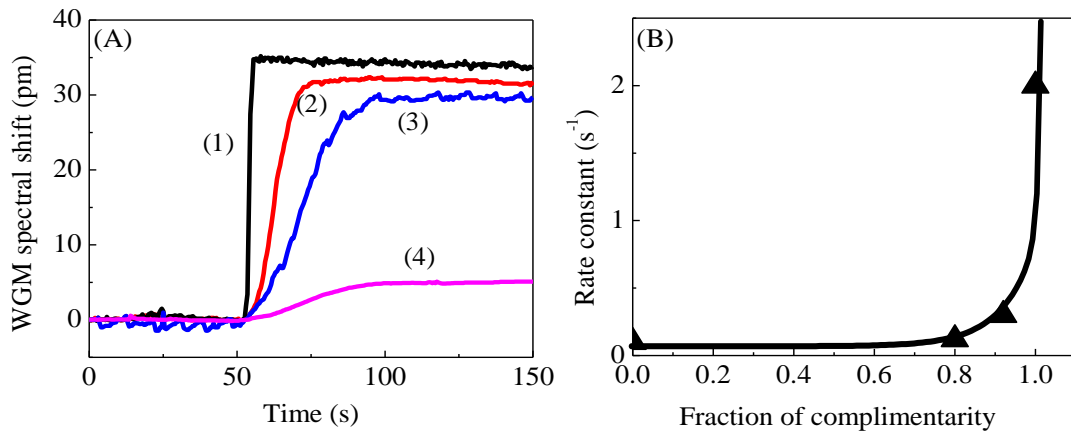


**Figure 3.6.** (A) Kinetic data showing binding curves for DNA target that is (1) 100% complementary; (2) 2-base mismatch; (3) 5-base mismatch; (4) completely mismatch. (B) Triangles: Rate constants extracted from (A) using a Langmuir model. Solid curve: exponential fit. DNA concentration: 10 mM.

To evaluate the concentration dynamic range of the OFRR DNA detection, we used complementary 25-base DNA ranging from 0.5 to 500 nM. The probes were immobilized on the OFRR interior surface as before, but the probe surface density was reduced in order to test the probe density effect on the OFRR sensing signal. The net WGM shift corresponding to the probe deposition was 12 pm, as compared to 21 pm obtained previously. Fig. 3.7 shows the net WGM shift in response to the target DNA concentration, which can be easily modeled as a function of bulk concentration using a form of Michaelis–Menton:

$$\delta\lambda_{WGM} = \frac{\delta\lambda_{\max} [DNA]}{K_d + [DNA]} \quad (3.2)$$

where  $\lambda_{WGM}$  is the relative spectral shift,  $\lambda_{\max}$  is the maximum possible shift observed for maximum surface coverage with target,  $K_d$  is the dissociation constant for hybridization, and  $[DNA]$  is the bulk concentration of the target strand. A Michaelis–Menton fit produces a dissociation constant  $K_d$  of 2.9 nM, close to what has been reported in previous studies [197, 198].  $\lambda_{\max}$  is 5.1 pm, which is half of the saturation WGM shift when a higher probe density was used.

To further explore the detection limit of the OFRR, the inset of Fig. 3.7 is presented with a net shift for 10 pM 25-mer using an OFRR with much higher sensitivity (37.1 nm/RIU), achieved by wall thinning. This demonstrates that improved LOD is possible with further optimization.

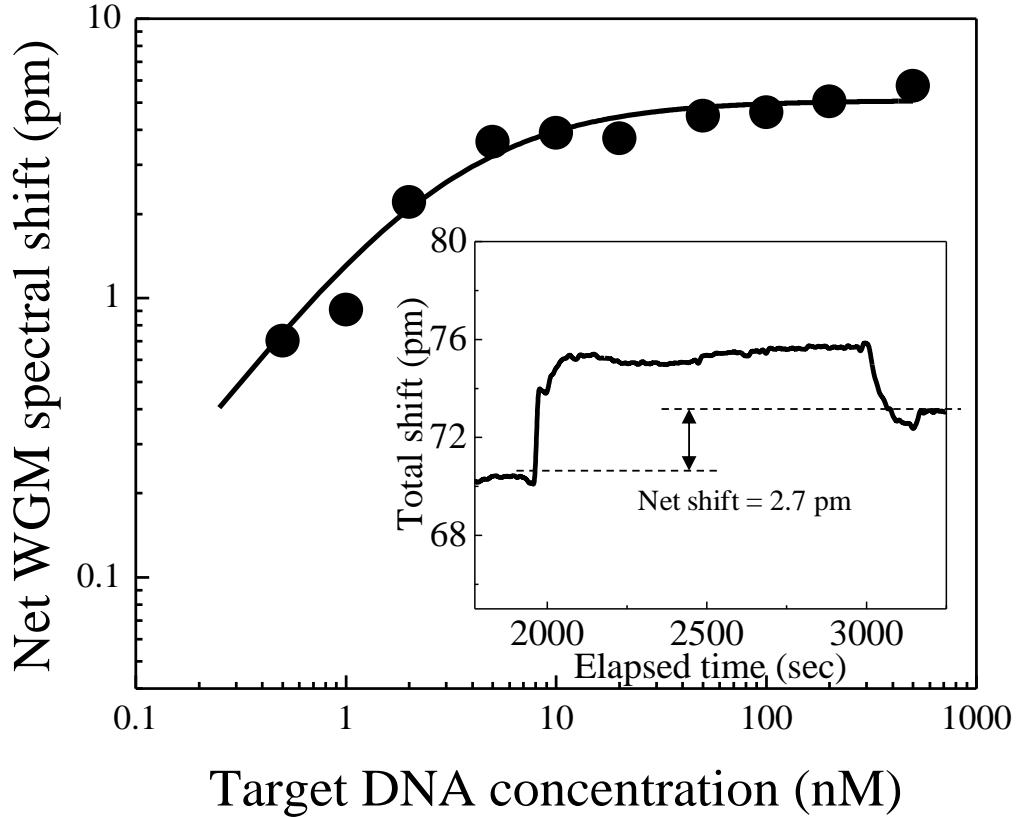


**Figure 3.7.** Target DNA titration curve using 25-mer strands. Solid line: Michaelis-Menton curve fit using  $K_d = 2.9$  nM and  $\delta\lambda_{\max} = 5.1$  pm. Insert shows net shift from 10 pM target using a 37 nm/RIU OFRR.

WGM shift versus surface coverage is plotted in Fig. 3.8, where the slope of each line is proportional to the molecular weight, and essentially the length, of the DNA represented. A linear relationship between the WGM shift and the molecule density on the OFRR surface has been developed and is described in Chapter 1 as Eq. (1.5) [32]. This equation allows for detailed quantitative analysis of the molecule detection using the OFRR. In our experiment,  $S = 6.8$  nm/RIU.  $n_3$  is assumed to be equal to that of water, 1.33, and  $n_2$  is 1.45 for silica. The excess polarizability for DNA scales linearly with

molecular weight and has been determined to be  $4\pi\epsilon_0(4.4\times 10^{-22} \text{ cm}^3)$  for 25-mer DNA,  $4\pi\epsilon_0(8.9\times 10^{-22} \text{ cm}^3)$  for 50-mer DNA, and  $4\pi\epsilon_0(1.78\times 10^{-21} \text{ cm}^3)$  for 100-mer DNA [33, 199].

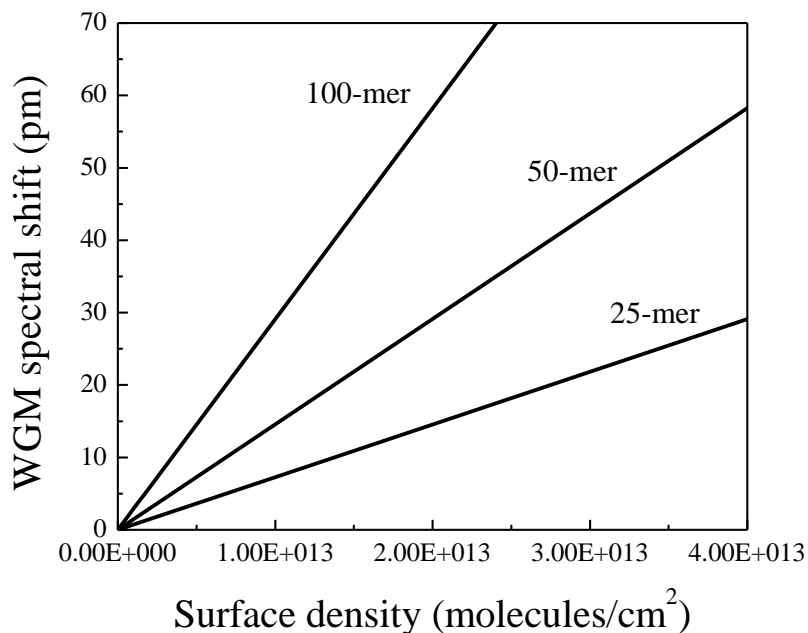


**Figure 3.8.** Theoretical WGM spectral shift as a function of the molecule density on the OFRR interior surface for various lengths of DNA. The BRIS is chosen to be 6.8 nm/RIU.

Using Eq. (1.5) it is also possible to deduce the LOD for DNA molecules on the surface, since the WGM shift is linearly proportional to the molecule density of the surface. Assuming that 0.02 pm is our system resolution, which has been obtained in an earlier study [87], the LOD for molecule density can be estimated using the net WGM shift. Corresponding surface densities for each chemical activation stage are listed in Table 3.1. For 25-mer, 50-mer, and 100-mer DNA samples, the LOD's are  $2.7\times 10^{10}$ ,  $1.5\times 10^{10}$ , and  $6.8\times 10^9$  molecules/cm<sup>2</sup>, respectively. The molecular weights of those DNA

samples are approximately 7.78, 16.01, and 31.57 kDa, for 25-mer, 50-mer, and 100-mer, respectively. Therefore, the LOD for mass loading can also be obtained.

According to our calculations the LOD for mass is on the order of  $4 \text{ pg/mm}^2$ , close to what is reported in label-free DNA detection based on microspheres [33] and SPR [187]. The minimal detectable surface coverage was also calculated, where the maximal loading density is assumed to be  $5.7 \times 10^{13} \text{ molecules/cm}^2$ . These values were 0.05%, 0.026%, and 0.012% for 25-mer, 50-mer, and 100-mer, respectively. Note that the minimal detectable surface coverage decreases progressively as the DNA strand lengths increases, since longer DNA carries larger mass.

### **3.5. Conclusions**

In this chapter, we have developed a protocol for OFRR based DNA assays. Detailed analysis of the OFRR response to a variety of DNA samples has been performed to evaluate the OFRR DNA detection capability. DNA molecules on the OFRR were quantified using the theoretical model that relates the sensing signal (WGM shift) to the molecule surface density. Bulk DNA detection of 10 pM 25-mer has been achieved and the actual limit of detection is significantly lower. The mass loading limit of detection is estimated to be  $4 \text{ pg/mm}^2$ , competitive with other label-free methods [33, 187].

Further improvement in the LOD can be accomplished with a better BRIS by using a thinner wall. Polymers such as dextran, to which multiple DNA probes can be attached, will also be used to increase the mass loading on the surface [33]. Furthermore, an additional reference channel can be used to reduce common-mode noise such as

temperature fluctuation and non-specific binding. Non-specific binding can also be further reduced by using blocking agents. Currently, 40–50% hybridization has been achieved. In the future, temperature and buffer salt concentration will be optimized to obtain more efficient hybridization [117]. In the meantime, microfabricated waveguides in replacement of fragile-tapered optical fibers for DNA microarray development will also be investigated [200].

## CHAPTER 4

### METHYLATED DNA ANALYSIS WITH THE OFRR

#### **4.1. Motivation of DNA methylation analysis**

Genomic methylation analysis is of great importance for cancer research and clinics, since it enables earlier cancer diagnosis prior to the point of metastasis [201]. An ever increasing body of work within the field of epigenomics is strengthening the linkage between the hypermethylation of key nucleotide sequences and the advent of many different cancers [201, 202]. As a natural component of cellular transcription, methyl groups are normally attached to select cytosine bases by methyltransferase enzymes in order to suppress expression of unnecessary proteins. Methylcytosines count for as much as 1% of all nucleotides in the human genome [203] and tend to be concentrated in CpG “islands” commonly seen in gene promoter regions [204]. However, abnormal methylation can prevent expression of important molecules, including those that govern cellular proliferation, which may lead to tumorigenesis [201, 205, 206].

In order to further study and predict this behavior, several methylation-specific assays have been developed [195, 207-209]. Two of the most common assays are restriction enzyme digestion [210] and bisulfite-conversion assays [209]. The restriction enzyme process involves digesting a large segment of DNA into smaller segments. Methylated bases prevent the enzyme cleavage, and the difference between strand lengths is detected via southern blot or PCR amplification [211]. While sophisticated and reliable, this method can only focus on a few restriction sites at a time, and cannot be

used to fully quantify the degree of methylation in a strand. The bisulfite method converts methylated cytosines to uracil bases that show up as thymine after PCR amplification and can be detected by sequencing or microarray hybridization [195]. Recently, a very interesting and sensitive FRET detection assay was developed based on bisulfate conversion [212]. While it is popular and widely used, it is known to be somewhat unpredictable and inefficient due to degradation of the DNA sample during conversion [211]. A very new method, called single-molecule, real-time sequencing (SMRT) cleverly uses DNA polymerases to create high-throughput, dye-coded DNA strands [213].

A great deal of recent research has focused on utilizing the interaction between DNA and methyl binding proteins to gain a better understanding of methylation patterns and regulation [214, 215]. Methyl binding proteins are a family of transcription-regulating molecules, among which five are currently known, that actually bind directly to methylcytosines. This provides an advantage compared to the previously discussed methods because no pre-treatment or conversion of the sample DNA is required in order to detect it. While each protein shares the same binding region, their functions and behavior are decidedly unique from one another [214, 216]. Only a few of these proteins, including MBD-2, are known to bind DNA in-vitro. MBD-2 is also known to bind methylated DNA with very little sequence specificity. Therefore, it is able to perform detection of the extent of methylation of any portion of the genome, making it very useful for cancer research and diagnostic applications. In addition to methyl binding proteins, methylcytosine-specific antibodies, such as anti 5-methylcytidine (anti-5mC), have also

been employed in methylation studies. Various detection protocols, such as such as methylated-CpG island recovery assay (MIRA) [217] and methylated DNA immunoprecipitation (MeDIP) [218] have been developed based on those capture molecules. While these technologies can be very sensitive, they require fluorescent labeling, and therefore, have a limited ability to perform quantitative methylation analysis due to the signal bias resulting from the lack of precise control in molar ratio of fluorophores to analytes [184].

In contrast, label-free detection offers an excellent alternative, which directly and quantitatively detects the analyte without fluorescence labeling. However, to date very few label-free sensing formats have been employed in methylation studies. One such technique involves a non-optical nano-wire-based field effect transistor (FET) sensor [219]. While this platform offers exceedingly low limits of detection, the fabrication of nanowires is a delicate and costly process.

Another recent label-free technique utilized surface plasmon resonance (SPR) to detect dsDNA using methyl binding proteins in a micro-array format [220]. SPR is a mature and sensitive assay, however the instrumentation is often quite costly.

Label-free detection can also be achieved using cylindrical opto-fluidic ring resonators (OFRRs). This structure has been described in the previous chapters, but the specific setup for these experiments is illustrated in Fig. 4.1(a) [92]. The OFRR is a thin-walled glass capillary. In the OFRR, the resonant light circulates repeatedly along the ring resonator surface and the resonance wavelength,  $\lambda$ , is determined by [31]. In the past few years, detection of various biomolecules using the OFRR has been demonstrated,

including virus [88], DNA [90, 92], protein [32], and cancer biomarker in serum or blood [221, 222].

In the work described in this chapter, DNA methylation analysis was demonstrated using a methyl binding protein, MBD-2, or antibody to capture methylated oligonucleotides to the OFRR inner surface, as illustrated by Fig. 4.1(b). The high specificity of MBD-2 proteins (or antibodies) and the quantitative, real-time optical sensing capabilities of the OFRR complement each other well. The sensor response to methylated oligonucleotides based on concentration and degree of methylation was investigated, showing that the protein can discriminate small changes in the degree of methylation, on the order of 3 to 5 methylcytosines. The MBD-2 protocol's preference for double stranded DNA (dsDNA) was also explored, and anti-5mC assays (shown in Fig. 4.1(c)) were carried out for comparison. It was observed that MBD-2 strongly prefers dsDNA, whereas the antibody binds more strongly to single stranded DNA (ssDNA), thus providing complementary approaches to methylation research.

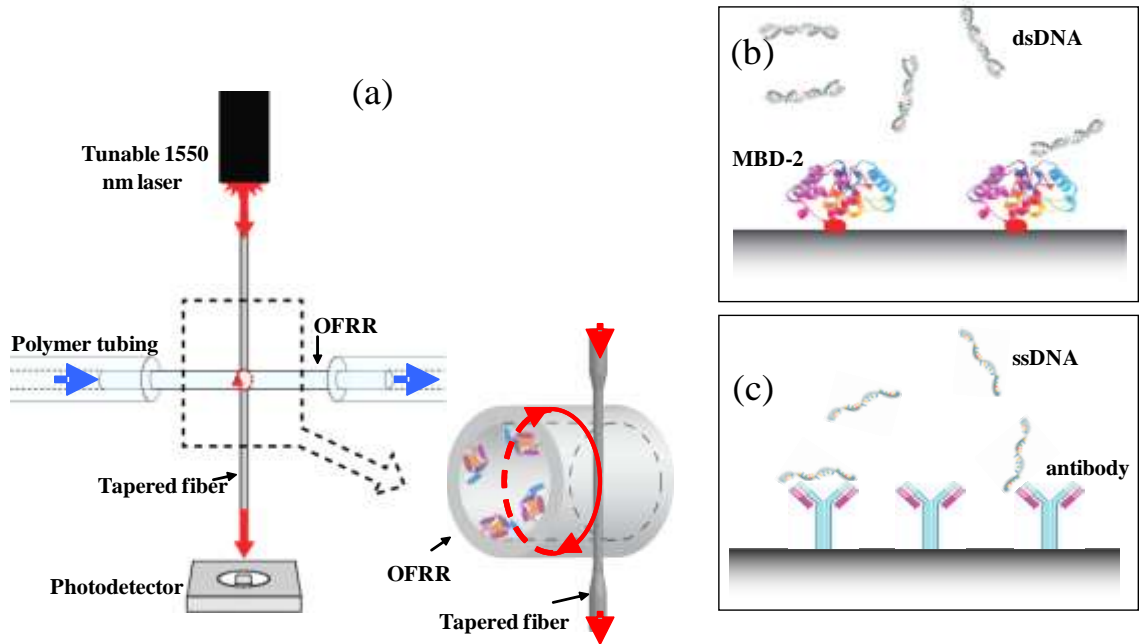


**Figure 4.1.** (a) Experimental setup for OFRR. Inset shows biomolecule immobilization on the interior capillary wall. (b) Representation of methylated DNA strands binding to methyl binding proteins. (c) Representation of methylated DNA strands binding to immobilized antibodies inside the OFRR.

## 4.2. Experimental methods

### 4.2.1. Materials

DNA samples (all 30 bases in length) were obtained from Integrated DNA Technologies. Details of the DNA sequences and methylation are as follows:

#### For MBD-2 protocol:

ssDNA, 5 methylcytosines per target strand (underlined nucleotides are methylated):

5' – CTG AGC TGT GCC GCC ACG TCG TGA AAG AGC – 3'

ssDNA, 3 methylcytosines per target strand:

5' – CTG AGC TGT GCC GCC ACG TCG TGA AAG AGC – 3'

ssDNA, 1 methylcytosine per target strand:

5' – CTG AGC TGT GCC GCC ACG TCG TGA AAG AGC – 3'

ssDNA, zero methylcytosines per target strand:

5' – CTG AGC TGT GCC GCC ACG TCG TGA AAG AGC – 3'

dsDNA, fully methylated, 5 methylcytosines per target strand:

5' – CTG AGC TGT GCC GCC ACG TCG TGA AAG AGC – 3'

3' – GAC TCG ACA CGG CGG TGC AGC ACT TTC TCG – 5'

dsDNA, fully methylated, 3 methylcytosines per target strand:

5' – CTG AGC TGT GCC GCC ACG TCG TGA AAG AGC – 3'

3' – GAC TCG ACA CGG CGG TGC AGC ACT TTC TCG – 5'

dsDNA, fully methylated, 1 methylcytosines per target strand:

5' – CTG AGC TGT GCC GCC ACG TCG TGA AAG AGC – 3'

3' – GAC TCG ACA CGG CGG TGC AGC ACT TTC TCG – 5'

dsDNA, zero methylcytosines per target strand (negative control):

5' – CTG AGC TGT GCC GCC ACG TCG TGA AAG AGC – 3'

3' – GAC TCG ACA CGG CGG TGC AGC ACT TTC TCG – 5'

dsDNA, hemi-methylated, 5 methylcytosines per target strand:

5' – CTG AGC TGT GCC GCC ACG TCG TGA AAG AGC – 3'

3' – GAC TCG ACA CGG CGG TGC AGC ACT TTC TCG – 5'

dsDNA, hemi-methylated, 3 methylcytosines per target strand:

5' – CTG AGC TGT GCC GCC ACG TCG TGA AAG AGC – 3'

3' – GAC TCG ACA CGG CGG TGC AGC ACT TTC TCG – 5'

dsDNA, hemi-methylated, 1 methylcytosines per target strand:

5' – CTG AGC TGT GCC GCC ACG TCG TGA AAG AGC – 3'

3' – GAC TCG ACA CGG CGG TGC AGC ACT TTC TCG – 5'

dsDNA, hemi-methylated, zero methylcytosines per target strand:

5' - CTG AGC TGT GCC GCC ACG TCG TGA AAG AGC - 3'

3' - GAC TCG ACA CGG CGG TGC AGC ACT TTC TCG - 5'

**For antibody protocol:**

ssDNA, 5 methylcytosines per target strand (underlined nucleotides are methylated):

5' – CTG AAC TGT TCC GCC CCA CTG TGA AAG AGC – 3'

ssDNA, 3 methylcytosines per target strand:

5' – CTG AAC TGT TCC GCC CCA CTG TGA AAG AGC – 3'

ssDNA, 1 methylcytosine per target strand:

5' – CTG AAC TGT TCC GCC CCA CTG TGA AAG AGC – 3'

ssDNA, zero methylcytosines per target strand:

5' – CTG AAC TGT TCC GCC CCA CTG TGA AAG AGC – 3'

Recombinant MBD-2 protein was obtained from Bioclone Inc. Antibody selected was mouse IgG<sub>1</sub> raised against 5-methylcytidine, purchased from AbD Serotec. Dimethyl adipimidate (DMA) and dimethyl pimelimidate (DMP) crosslinker was obtained from Pierce. Other reagents, including SSC buffer, PBS buffer, ethanol, hydrofluoric acid, 3-aminopropyltrimethoxysilane (3-APS), and protein G were obtained from Sigma-Aldrich. OFRR capillary performs were purchased from Sutter Instruments. Water, used as a diluent or in buffers, was purified to 18 MΩ using a Barnstead Easypure-UV system.

### 4.2.2. Sensor fabrication

The OFRR fabrication and characterization have been discussed in the previous chapters and in previous publications [83, 189]. Briefly, a quartz glass capillary with an outer diameter of 1.2 mm and wall thickness of 150  $\mu\text{m}$  was pulled under  $\text{CO}_2$  laser illumination until the outer diameter was approximately 100  $\mu\text{m}$  and the wall thickness was approximately 5  $\mu\text{m}$ . Then hydrofluoric acid (HF) was passed through the capillary, etching the wall down even further. The OFRR was then placed on top of a thermal electric cooling (TEC) unit. The experiments were performed at room temperature. A syringe pump was used to push the fluid through the OFRR at a constant rate of 10  $\mu\text{L}/\text{min}$ . The resonant light from a tunable diode laser (1550 nm) scanned at 2 Hz was coupled into the OFRR by an optical taper in contact with the OFRR (Fig. 4.1(a)). The resonance wavelength emerged as a dip in this transmitted spectrum, which shifted in response to biomolecule attachment to the OFRR inner surface.

Based on our previous theoretical analysis, the resonance wavelength shift,  $\delta\lambda$ , is linearly dependent on the molecules attached to the OFRR inner surface [32]:

$$\frac{\delta\lambda}{S} \propto \sigma \quad (4.1)$$

where  $S$  is the bulk RI change and  $\sigma$  is the molecule surface density. In the following studies, we will use  $\Delta n = \delta\lambda/S$  (in units of “refractive index units (RIU)”) as the sensing signal.

### 4.2.3. Experimental protocol

To immobilize MBD-2 onto the inner surface of the OFRR, the OFRR was cleaned with HF and purged with air to generate a more hydrophobic surface. Then, 3-APS (1% by volume) was passed through and allowed to form a layer on top of this. To encourage crosslinking between silane molecules, the OFRR was then drained of fluid and heated with the TEC to 50°C for 20 to 40 minutes. Then MBD-2 was crosslinked to the surface with 5 mg/mL DMA. After rinsing, the DNA sample was introduced. Fig. 4.2(a) shows a sample sensorgram representing the MBD-2 immobilization and sample DNA detection steps. Each step is represented as a large increase in sensing signal due to both specific and non-specific binding as well as bulk RI changes. The subsequent rinsing steps cause a substantial RI drop due to removal of non-specific binding and bulk RI change, but the resulting net change represents specifically bound analytes.

Fig. 4.2(b) demonstrates the sensor preparation process for anti-5mC based detection. The sensor was silanized the same way as in MBD-2, but then protein G (at 0.1 mg/mL) was covalently crosslinked to the 3-APS layer using DMP (at 5 mg/mL). Next, anti-5mC antibodies were introduced at a concentration of 10 µg/mL and allowed to bind to protein G. After this treatment, the capillary was ready to selectively immobilize methylated oligonucleotide targets. The inset of Fig. 4.2(b) shows the lowest demonstrated concentration of ssDNA captured with this method, which is 5 nM. The shift, or  $\Delta n$  from this sample,  $3.2 \times 10^{-5}$  RIU, is well above the RI detection limit of the sensor, which is closer to  $2 \times 10^{-6}$  RIU based on the spectral noise observed from these sensorgrams, so it is theoretically possible to detect samples below 1 nM.

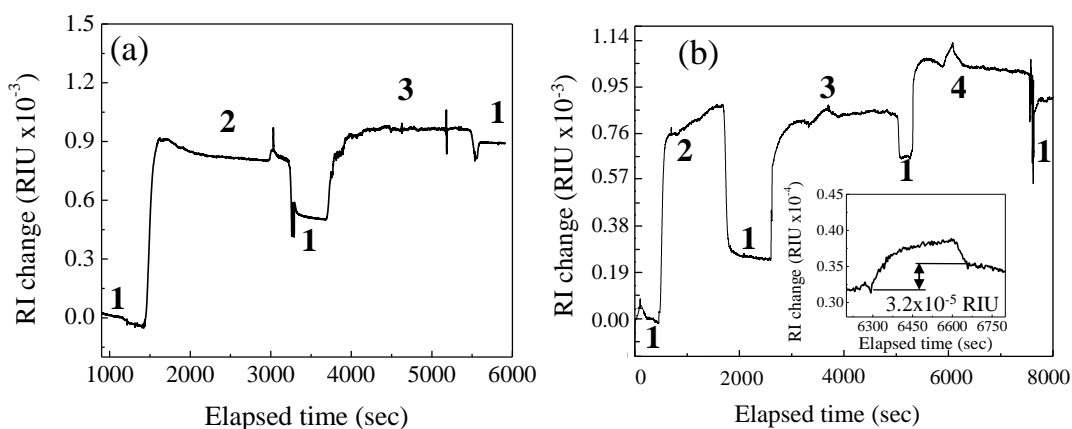


**Figure 4.2.** Sensorgram showing DNA detection with MBD-2 (a) and anti-5mC (b). For (a) steps are: PBS buffer rinse 1, MBD-2 protein immobilization 2, and capture of 10  $\mu$ M 30-mer dsDNA with 5 methylcytosines 3. For (b) steps are: PBS buffer rinse 1, protein G immobilization 2, antibody immobilization 3, and capture of 10  $\mu$ M ssDNA with 5 methylcytosines 4. Inset shows resolvable shift resulting from 5 nM methylated ssDNA.

### 4.3. Results

Titration curves are plotted in Fig. 4.3 to compare the protein's performance in binding different types of DNA (fully methylated dsDNA and methylated ssDNA) at concentrations ranging from 1 nM to 10  $\mu$ M with 5 methylcytosines each. An unmethylated dsDNA sample was used as a negative control. This data shows that MBD-2 binds much more strongly to dsDNA than to the other samples, which is consistent with past studies of this protein [214]. Compared to the negative control in Fig. 4.3, the ssDNA signal cannot really be statistically separated, indicative of weak interaction with the protein. Fitting a Langmuirian curve to the dsDNA data, we found an estimated dissociation constant (or  $K_d$ ) equal to 15 nM. Although, to our knowledge, no data exists

regarding the dissociation constant of MBD-2 specifically, our result is similar to that recorded for other methyl binding proteins [223].

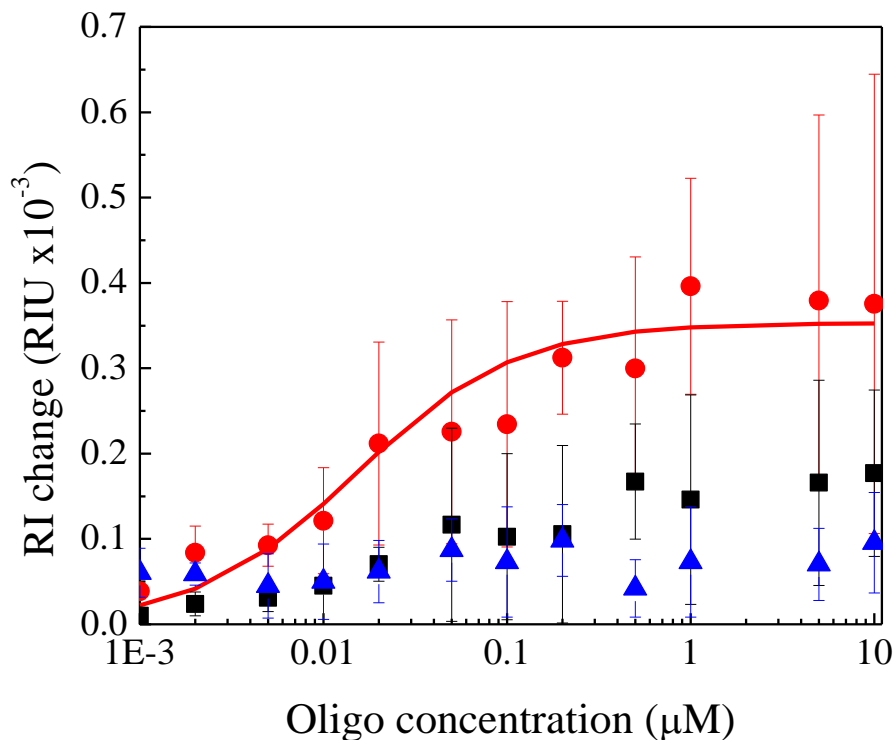


**Figure 4.3.** Titration curves for MBD-2 experiments including 5-methyl dsDNA (circular data points), 5-methyl ssDNA (square data points), and a negative control containing no methylcytosines (triangular data points). The fitted curve yields a  $K_d$  value of 15 nM for dsDNA. The ssDNA data cannot be discriminated from the negative control.

The alternative protocol, using anti-5mC was also investigated based on binding curves for dsDNA and ssDNA. In Fig. 4.4(a) dsDNA was introduced to an antibody-covered sensor, showing a net RI change after dsDNA binding, which is almost 10 times smaller than the shift obtained from the MBD-2 method. Conversely, the antibody has a strong response to ssDNA samples with 5 methylcytosines, as shown in Fig. 4.4(b). Fig.

4.4(b) plots titration curves for ssDNA detection using anti-5mC and ssDNA samples between 1 nM and 10  $\mu$ M. The curve from the antibody-based immobilization yields a dissociation constant of 36 nM. It can be concluded that anti-5mC strongly prefers ssDNA samples to dsDNA samples, the opposite of what was observed with MBD-2. This conclusion is reinforced by recent publications [217, 224].

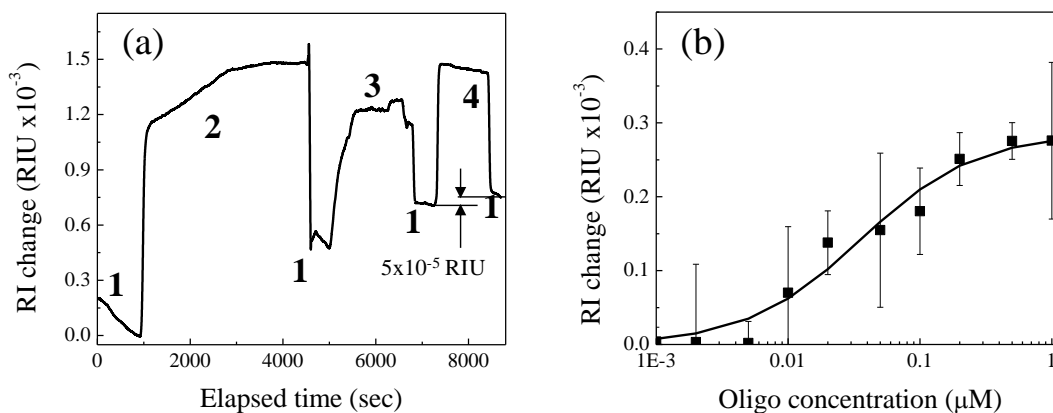


**Figure 4.4.** (a) Sensorgram for immobilization of 10  $\mu$ M dsDNA with 5 methylcytosines with anti-5mC showing very small net shift. Steps: PBS buffer rinse 1, protein G immobilization 2, antibody immobilization 3, and 10  $\mu$ M ssDNA capture 4. (b) Titration curves for anti-5mC experiments using 10  $\mu$ M, 5-methyl ssDNA. The fitted curve yields a  $K_d$  of 36 nM for the antibody-based approach.

In addition to strand-type (*i.e.*, double-stranded vs. single stranded) comparisons, it is important to characterize the OFRR's ability to discriminate small differences in methylation density. Fig. 4.5(a) compares signals from 10  $\mu$ M 30-mer DNA samples with either 0 (negative control), 1, 3, or 5 methyl groups per strand. These strands were either fully methylated dsDNA (both strands being methylated), hemi-methylated (only a single strand being methylated), or methylated ssDNA. Several trends are quite clear. Discrimination between strands based on a single methyl group was not observed with

MBD-2 because very little single-methylated sample was captured. However, at 3 or 5 methylcytosines fully methylated dsDNA can be clearly distinguished. Some binding also occurred between the methylated ssDNA and hemi-methylated dsDNA samples at 3 or 5 methyl groups per strand, but at a much lower level, as compared to fully methylated dsDNA. Also, there is no statistical difference between the signal from methylated ssDNA and hemi-methylated dsDNA. This is consistent with previous observations in the literature [214]. In fact, it is well known that MBD-2 needs to form a dimer with MBD-3 in order to strongly bind hemi-methylated DNA [225]. While these observations have been made before, never have they delivered the ability for quantitative optical label-free analysis. Instead, research has been limited to fluorescence-based approaches like microarrays and gel assays.

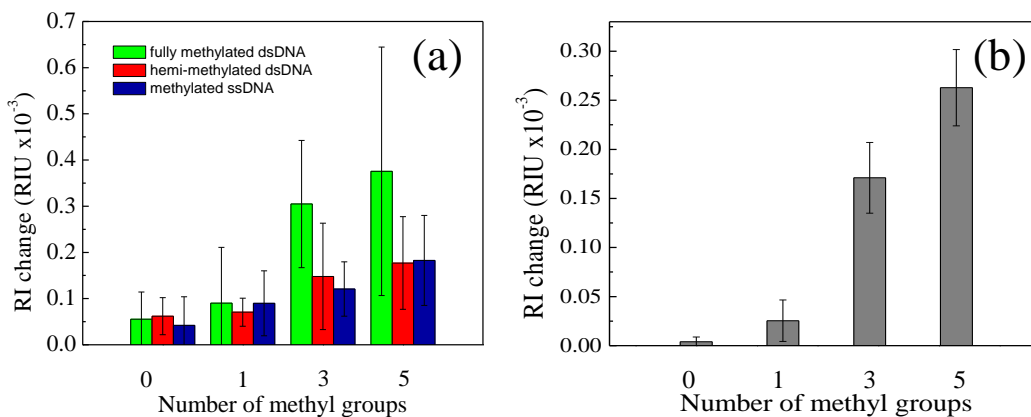


**Figure 4.5.** (a) Net resonance wavelength shift values for 10  $\mu$ M DNA with variable methylation states after binding to immobilized MBD-2 proteins. DNA samples were either fully methylated dsDNA (left bars), hemi-methylated dsDNA (middle bars), or methylated ssDNA (right bars). (b) Net resonance wavelength shift values for 10  $\mu$ M ssDNA with variable methylation states after binding to immobilized 5-mC antibodies.

In Fig. 4.5(b), the effect of degree of methylation on the antibody-based approach is examined. We used 10  $\mu\text{M}$  ssDNA with 0, 1, 3, and 5 methyl groups per strand. It is quite clear that in this case, different number of methylation cytosine have significant impact on the ssDNA's affinity for antibody. Using our method, we were able to differentiate between unmethylated and single-methylated ssDNA. Fig. 4.5(a) and (b) together demonstrate the obvious difference in the two assays. Methyl binding proteins show much stronger binding affinity for dsDNA and anti-5mC antibodies show much stronger binding affinity for ssDNA. The strengths and weaknesses of these approaches must be considered to determine which is appropriate for a particular application.

#### **4.4. Conclusions**

We have developed OFRR label-free sensors for DNA methylation analysis using MBD-2 and anti-5mC as the capture molecule. It is shown that the MBD-2 methods, for most applications, will be preferable due to its ability to bind dsDNA that naturally exists in blood samples. However, the antibody method provides a better capability to identify single methylcytosines. Future efforts will focus on developing this sensor for nucleotide-sequence-specific methylation analysis by expanding our protocol to use both DNA hybridization (for determining sequence specificity) and methyl binding protein recognition (for determining methylation density). Actual DNA samples from blood will also be used to evaluate the clinical utility of the OFRR based methylation analysis.

# CHAPTER 5

## INTRODUCTION TO RING RESONATOR-BASED MICROFLUIDIC LASERS

### 5.1. Background of microfluidic lasers

Another important application of the ring resonator is the laser, which was first demonstrated in the 1960's using doped microspheres with the gain medium being in the solid state [226]. Since then, many solid state ring resonator lasers have been created using microspheres [49, 227-229], planar rings [230], cylinders [231], and even microtoroids [232]. Cylindrical microcavity lasers can also be formed from optical fibers coated with a high RI fluorescent polymer [233] or from polymer ring doped with dye [234]. Due to the multimode nature of WGMs within ring resonators, the lasing output is typically multi-peaked like the spectrum shown in Fig. 5.1. The relatively broadband emission of ring resonator lasers can be minimized by etching a grating onto the sphere surface [227] or by using the Vernier effect with a second ring of a different size [234].

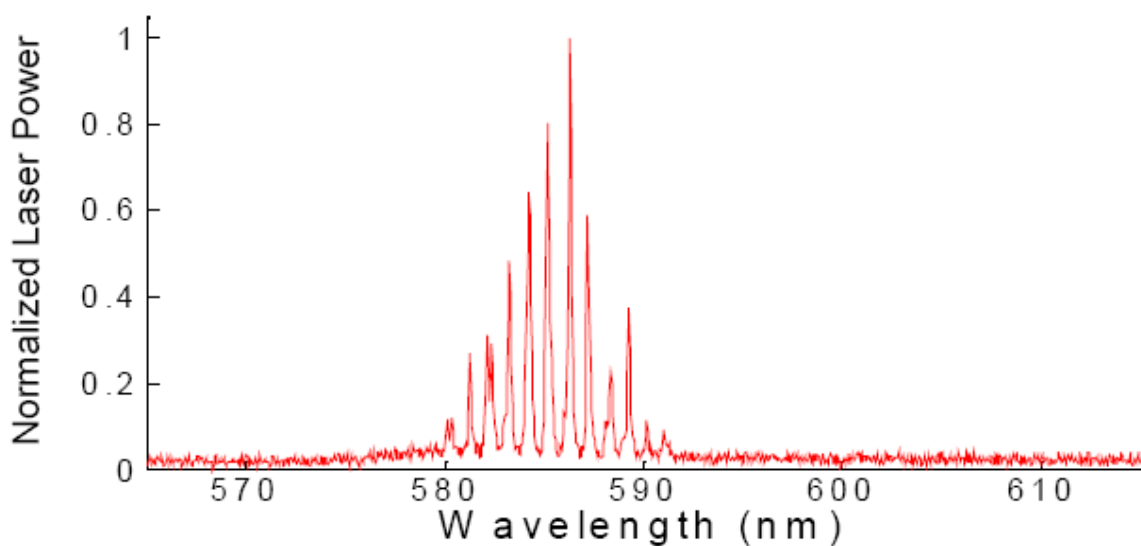


**Figure 5.1.** Broadband R6G lasing from a PDMS fluid planar ring. Reprinted with permission from Li et al. (2007).

Ring resonators have recently been employed in microfluidic lasers, in which the gain medium is in liquid form. Table 5.1 lists the relevant traits of some interesting microfluidic lasers described in the literature. They take advantage of the adaptive nature of liquid, the convenience of changing the liquid gain medium, potential compatibility with microfluidics for easy and safe gain medium and sample delivery. As a result, these devices are of great interest for the development of integrated, miniaturized tunable laser light sources with broad spectral coverage and for the development of micro-total-analysis system (or lab-on-a-chip) for biological and chemical analysis.

In ring resonator microfluidic lasers, the gain medium is usually fluorescent dyes or quantum dots (QDs) [235] dissolved in solvent. For Raman lasers, the gain can be the solvent itself. Many solvents, such as carbon disulfide [236], glycerol [27] or ethanol [237], have large Raman gain coefficients and therefore can be used as an excellent

Raman gain medium. The dye may be carried externally to the resonator cavity using microfluidics (in the case of a solid ring resonator) or it may be embedded or dissolved within it (in the case of a fluid ring resonator). In the first case, the gain region for the dye will be the small area of evanescent overlap. In the second case, the majority of the WGM optical field within the resonator can be used as the gain region.

The optical pump of the gain medium can be from the direct excitation by tuning the pump light into the gain absorption band or from indirect excitation through such a mechanism as energy transfer. It is achieved either by free space excitation or through an optical coupler such as a fiber taper, waveguide, or prism. The dye emission is coupled into the WGM, which provides positive optical feedback for lasing. Due to the high Q-factor of the ring resonator, low threshold lasing is possible. The laser can be in a continuous wave (CW) mode or a pulsed mode, depending on how it is pumped. The laser output is typically collected by free space coupling or through an optical coupler for efficient and directional light delivery.

## **5.2. Current examples of ring resonator-based microfluidic lasers**

### **5.2.1. Solid dielectric microspheres**

Microspheres are among the most widely used formats for microfluidic lasers. Compared to droplet lasers they are much easier to manipulate and compared to most other geometries they are easier to produce. The world-record Q-factors obtainable with microspheres [31] also provide extremely high optical feedback for extremely low lasing thresholds.

In order to create a microfluidic laser from a microsphere, the sphere must be immersed in a fluorescent gain medium. Lasing has been observed from microspheres immersed in R6G, obtaining a threshold of 200  $\mu\text{J}$  per pulse from 532 nm laser with a 10 nsec pulse [238]. This work also showed how the spectral position of the peak lasing emission changed depending on the concentration of R6G used due to self-absorption.

### **5.2.2. Microdroplets**

Unlike solid microspheres, the majority of the WGM of a microdroplet is accessible to gain-generating molecules. Microdroplet lasers have been created from ethanol [68], methanol [67], ethylene glycol [76], and water [66, 239], and are typically cladded with air, providing high RI contrast. The emission of microdroplets is usually collected and excited via free-space, due to the difficulty in controlling and positioning the droplets. However, coupling of a tapered optical fiber to a liquid-cladded droplet has been demonstrated as an efficient delivery waveguide for lasing emissions [71]. Such advancement makes the use of microdroplets much more practical, however positioning of such a fiber is quite difficult.

Manipulation of microdroplet lasers is another significant challenge which has been approached a number of different ways. Often, droplets generated at the end of a pipette or similar orifice can be lased while they hang. With the use of delicate optical alignments, droplets can even be lased as they fall through space as shown in Fig. 5.2 with Rhodamine 590 in ethanol [240]. More recently, droplet levitation has been researched [76, 235]. Levitating droplet in air prevents distortion and optical loss from contact with a

substrate. Ultrahydrophobic substrates, however, can provide an excellent way of controlling droplets while creating good fluid contact angles in order to maintain sphericity [27, 241]. Contact angles over  $150^\circ$  have been measured.

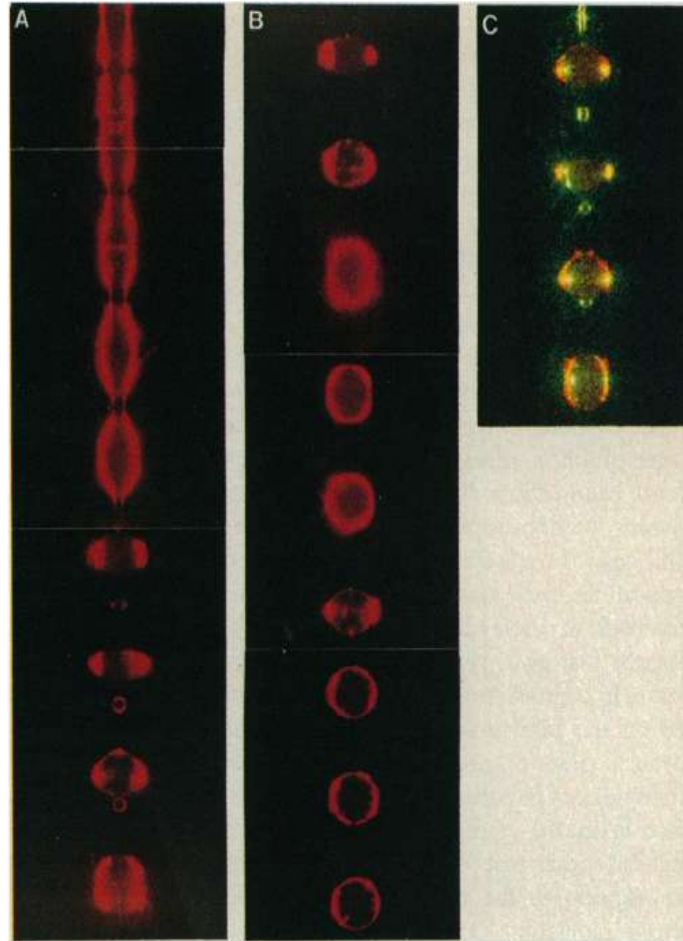


**Figure 5.2.** Red lasing signal from Rhodamine 590-doped ethanol droplets near the top of the aperture (a), much farther down (b), and with the green scattering signal from pump laser (c). Reprinted with permission from Qian et al. (1986).

It is also possible to substitute the air cladding for enhanced droplet stability. Saito et al. (2008) demonstrated that it was possible also to suspend a methanol microdroplet within a viscous polysiloxane resin (Fig. 5.3(a)). Doing so provides the benefit of being able to isolate the droplet in a defined position. This manuscript also demonstrated that

shape deformations could be induced on the droplet by squeezing the elastomer, which allows tuning of the droplet lasing spectrum as shown in Fig. 5.3(b). Droplets have also been produced within another liquid by forming water droplets (RI=1.33) in a lower RI oil (RI=1.29) [70, 71]. While handling and positioning of microdroplets within another liquid can be challenging, it avoids the problem of evaporation which plagues microdroplets in air. Extremely small droplets possess such an extremely large surface to volume ratio that evaporation will have an appreciable impact on the volume within seconds. Tanyeri et al. (2007) achieved lasing in R6G-doped water/glycerol microdroplets carried through fluidic chambers filled with oil. This not only presents a good solution to prevent droplet evaporation, but also proves that the droplets can be precisely positioned within the fluid given the correct approach.

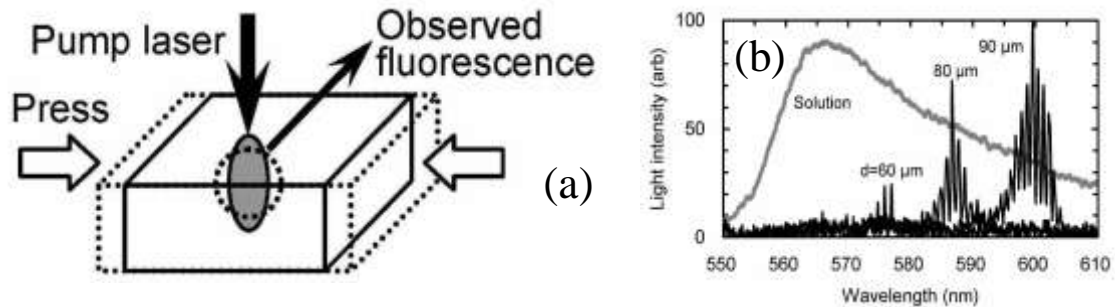


**Figure 5.3.** Schematic of microdroplet laser tuning with mechanical deflection (a). Laser spectrum dependence on droplet diameter. Reprinted with permission from Saito et al. (2008).

Demonstrations of microdroplet lasers have utilized both conventional dyes and quantum dots. An example of the latter used 9  $\mu\text{m}$  diameter droplets of water/glycerin with CdSe/ZnS quantum dots dissolved in them [235]. These droplets achieved a threshold of  $53 \text{ mJ/cm}^2$ . The most common dye for microdroplet lasing is R6G because of

its high quantum efficiency. Early demonstrations produced some relatively high lasing thresholds with falling R6G-doped droplets. For instance, Lin et al. (1986) observed  $10^4$  W/cm<sup>2</sup> using a pulsed pump system and Tzeng et al. (1984) observed 35 W/cm<sup>2</sup> using a CW pump system. Levitated droplets have shown lasing thresholds of 500 mW using R6G [76]. A similar dye, Rhodamine B, has been used with a pulsed pump laser, exhibiting a lasing threshold of 750 J/cm<sup>2</sup> in 20 μm droplets [241].

Microdroplets have also been explored for Raman lasers. Weak Raman signals can be amplified by the WGM in a ring resonator. Raman lasing has been demonstrated in microdroplets using strong Raman bands within glycerol [27]. Stimulated Raman scattering (SRS), a similar coherent phenomenon, has been demonstrated many times with microdroplets [5, 237, 242-246]. These experiments are largely interesting for purposes relating to theoretical research, but also have the potential to eventually provide versatile customizable light sources.

### **5.2.3. Cylinder and microcapillary**

Cylindrical ring resonators bring the same benefits to microfluidic lasers that they do to biological and chemical sensing. With hollow capillaries, dye media can be passed through the center of the capillary continuously, preventing intensity drops due to photobleaching. Additionally, since the dye is flowed through the hollow core, the laser energy can be coupled out via the external capillary surface using a fiber taper [247] or angle-polished fiber prism [248]. This is particularly important because without such outcoupling ability, the laser energy generated by the resonator will be scattered

tangentially away and will be much less useful for all practical purposes.

Cylinders can also be used for microfluidic lasers. As with microspheres, a solid cylinder (essentially an optical fiber) must be immersed in the gain medium. An interesting idea involving cylinders requires threading a 125  $\mu\text{m}$  silica fiber inside of a capillary and filling the gap space with R6G in ethanol (RI of ethanol = 1.361) [249]. This configuration is displayed in Fig. 5.4(a). The evanescent field from the inner fiber is used to create the gain medium. The lasing threshold observed for this system was 200  $\mu\text{J}$  with a 5 nsec pulsed laser source and looks like the photograph in Fig. 5.4(b).

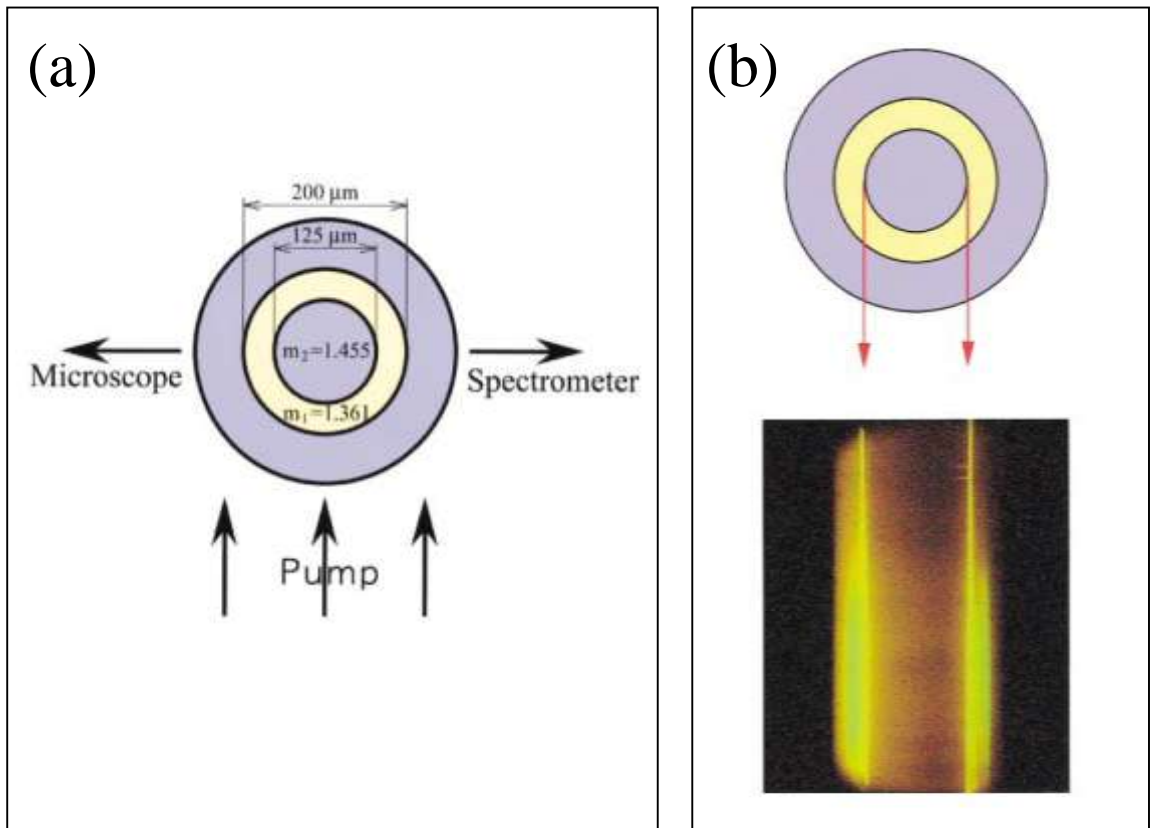


**Figure 5.4.** Capillary with axial silica rod and ethanol filled fluid cavity with R6G (a) and a photograph of WGM emission (b). Reprinted with permission from Moon et al. (2000).

Very low lasing thresholds down to  $25 \text{ nJ/mm}^2$  have been demonstrated with thin-walled capillaries using R6G in ethanol [250]. In the same manuscript, it was also demonstrated that capillaries can operate in two different lasing modes depending on the RI of the dye solvent, providing the potential for versatile RI selection. In the case that the RI of the solvent is less than that of the capillary wall (usually around 1.45), the WGM exists almost entirely within the glass wall. In the case that the RI of the solvent is greater however, such as in the case of solvents like quinoline (RI=1.626), the WGMs exist almost entirely within the fluid core. Knight et al. (1992) was the first to observe cylindrical WGM lasing with R6G in quinoline using a thick-walled capillary [251]. Several subsequent studies pursued this strategy as well [252]. A similar study, also using R6G in quinoline, was conducted by Moon et al. (2000), which examined how decreasing the RI of the solvent inside the capillary caused blue shifts in the WGM lasing spectrum. It is possible to obtain the same result using PDMS cavities with a quinoline dye solvent [248].

Thin-walled capillary microlasers can be used as intra-cavity biosensors. Using an R6G donor and an LDS 722 acceptor, Shopova et al. (2008) created a FRET laser. A cascaded FRET laser was also demonstrated using Coumarin 480 as the first donor in sequence with R6G and LDS 722. Also, a QD was used as a donor to excite Nile Blue lasing in the same cavity [253]. These demonstrations comprise one of the few efforts to date in the direction of microfluidic laser-based biosensing.

#### **5.2.4. Planar ring resonators**

Planar ring resonators are a relatively uncommon form of microfluidic laser. They are innately well suited for handling dye solution because it can be flowed over the ring surface without disturbing alignments or distorting structures. Microfluidic lasers have been demonstrated with fluid channels fabricated in PDMS polymer [122]. As long as the fluid RI is maintained above that of PDMS, the structure works as a ring resonator. In this case, the channels were filled with a methanol/ethylene glycol mixture, which had an RI just large enough to confine WGMs ( $RI = 1.409$ ). The channels were pumped with a pulsed laser resulting in a lasing threshold of 9 nJ/pulse.

#### **5.2.5. Microfiber loops**

The microfiber loop is a relatively new form of ring resonator, and as such, is still being developed towards its full potential. However, it has been proven to be quite functional as a microfluidic laser. Because of this ring resonator's fiber composition, the lasing signal can be easily collected through its ends without evanescent coupling to an external waveguide.

Jiang et al. (2007) immersed a microknot into an R6G solution and launched a pulsed pump signal through it. The evanescent field from the fiber excited the surrounding dye, which then coupled into the ring's WGMs. The laser signal generated from the WGM had a threshold of 9.2  $\mu$ J/pulse. The resulting system can be seen in Fig. 5.5.

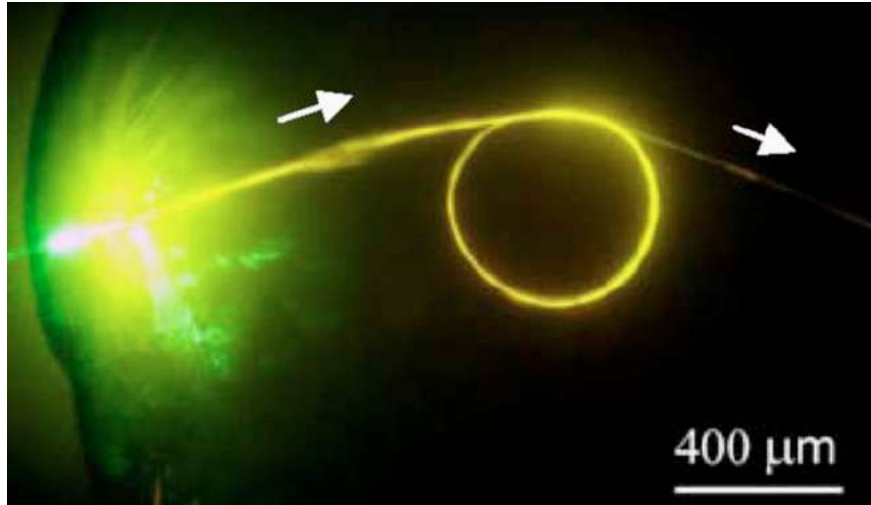


**Figure 5.5.** Microfluidic laser from 450  $\mu\text{m}$  microknot immersed in an R6G solution. Reprinted with permission from Jiang et al. (2007).

To summarize, Table 5.1 gives a quick review of some of the optofluidic ring resonator laser technologies discussed in the preceding section. They can be compared based on the gain medium used for lasing as well as the threshold achieved. Note that CW mode operation is quite difficult to achieve due to its relatively low average power and is thus rather rare in the literature.

**Table 5.1.** Comparison of lasing threshold and lasing mode for various types of optofluidic ring resonators

Platform	Lasing Threshold	Mode (CW/pulse)	Gain	Reference
Microsphere	200 $\mu\text{J/pulse}$	Pulsed (10 nsec)	R6G	[238]
Microdroplet	500 mW	Pulsed (5 nsec)	R6G	[76]
Microdroplet	750 $\text{J/cm}^2$	Pulsed (100 nsec)	Rhodamine B	[241]
Microdroplet	35 $\text{W/cm}^2$	CW	R6G	[68]
Microdroplet	0.5 $\text{MW/cm}^2$	Pulsed (100 nsec)	R6G	[70]
Microdroplet	0.4 $\text{J/pulse}$	Pulsed (10 nsec)	CdSe/ZnS QD	[235]
Microdroplet	NA	Pulsed	Glycerol/water (Raman)	[27]
Microcapillary	25 $\text{nJ/mm}^2$	Pulsed (10 nsec)	R6G	[250]
Microfiber	9.2 $\mu\text{J/pulse}$	Pulsed (6 nsec)	R6G	[160]
Loop				

## CHAPTER 6

### PDMS PACKAGING OF OFRR-BASED MICROFLUIDIC LASERS

#### 6.1. Motivation for packaging

Many different configurations for opto-fluidic dye lasers have been reported in the previous chapter. Recently however, the opto-fluidic ring resonator (OFRR) was also developed to provide a unique interface for the photonic cavity and microfluidics [247, 250, 253, 254]. In the OFRR case, the gain medium, typically dye solution, flows through the core and interacts with the WGM, which provides the optical feedback for the laser [247, 250, 253]. The laser emission can be efficiently coupled out through an optical coupler in contact with the OFRR, thus providing a convenient means to guide and deliver the laser emission [247, 250].

Although significant progress has been made in both experimental and theoretical aspects of the OFRR laser [247, 250, 253, 254], to date it has operated in free space with the tapered fiber and OFRR capillary being suspended in air, which is too delicate for manual manipulation and is difficult to mount on a chip. The infrastructure for fluidic connectivity is also too bulky to fit within the footprint of a traditional lab-on-a-chip device. Improvement in the portability and mechanical strength of the OFRR laser and demonstration of its compatibility with soft lithography based microfluidics platforms has now become a crucial step towards eventual OFRR based  $\mu$ TAS development. In this paper, we address these issues by embedding the glass based OFRR in a polymer of low refractive index (RI), as illustrated in Fig. 6.1. When the high index gain medium (such as

dye in a solvent) is passed through the OFRR, the WGM forms at the boundary between the liquid and the glass wall and provides optical feedback for lasing. The laser emission can be directionally out-coupled into a fiber through a fiber prism or a tapered optical fiber in contact with the OFRR. We will show that a Q-factor in excess of  $10^6$  can still be obtained, leading to a laser threshold below  $1 \mu\text{J}/\text{mm}^2$ , on par with or even better than most of the microfluidic lasers mentioned previously. The laser output from the fiber is measured to be 80 nW, corresponding to 50% power extraction efficiency. These designs not only enhance the portability and mechanical strength of the microfluidic laser itself, but also provide the convenience of connecting it to microfluidics built within a polymer-based chip. Eventually, due to the small size of the OFRR ( $\sim 100 \mu\text{m}$  in diameter), a large number of the microfluidic dye lasers can be packed on a small chip for multiplexed functionalities.

## **6.2. Experimental methods**

### **6.2.1. Materials and fabrication**

The fiber prism used in our work is made out of a 200- $\mu\text{m}$  multimode fiber, which is first anchored in acrylic and then angle polished at  $15^\circ$  at one of its ends [21, 255]. The tapered fiber is made by pulling an SMF-28 optical fiber under intense heat until it reaches approximately 3  $\mu\text{m}$  at its narrowest part. The OFRR with an outer diameter (OD) of 75  $\mu\text{m}$  and a wall thickness of 5  $\mu\text{m}$  is drawn out of a fused silica preform (Polymicro) using previously published methods [250]. The embedding process is highlighted in Fig. 6.2. The fiber prism (or tapered fiber) is then positioned against the OFRR and the whole

device is placed in a small module before liquid polydimethylsiloxane (PDMS, Dow Corning Sylgard 184) is poured on the device and cured in air at 70°C for 2 hours. A photograph of the finished product is shown in Fig. 6.3. We choose PDMS because it is a material commonly used in microfluidic devices and it has a relatively low refractive index ( $n \sim 1.41$ ) [256]. It is also chemically inert and has low loss in the visible spectrum, both of which are important characteristics in microfluidic laser development.

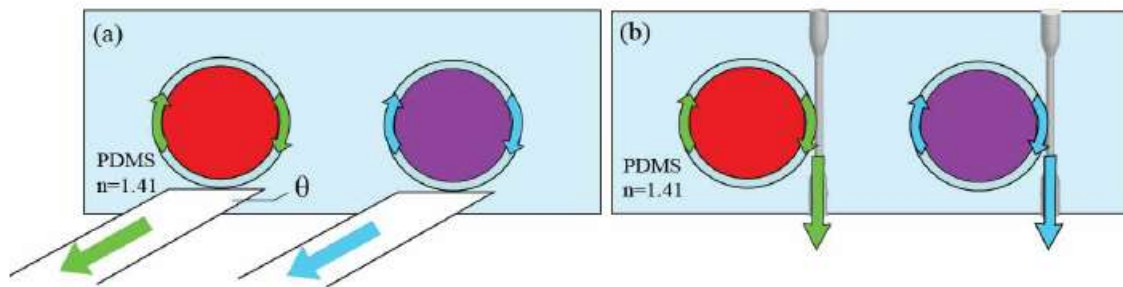


**Figure 6.1.** (A) Conceptual illustration of the glass based OFRR embedded in a low index polymer. The laser emission can be directionally coupled out through a tapered optical fiber or a fiber prism for easy light delivery.  $\theta$  is the fiber prism angle. (B). The OFRR formed by filling the circular void with high index gain medium. (C) Conceptual illustration of the polymer embedded OFRR array with different laser emission spectra.

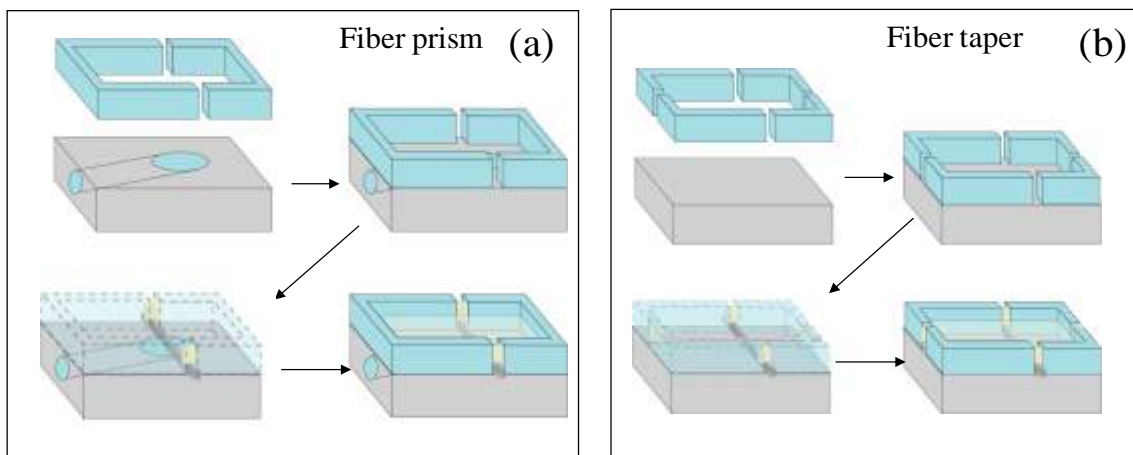


**Figure 6.2.** Fabrication process of PDMS-embedded OFRRs for the angle-polished fiber method (a) and the fiber-taper method (b).

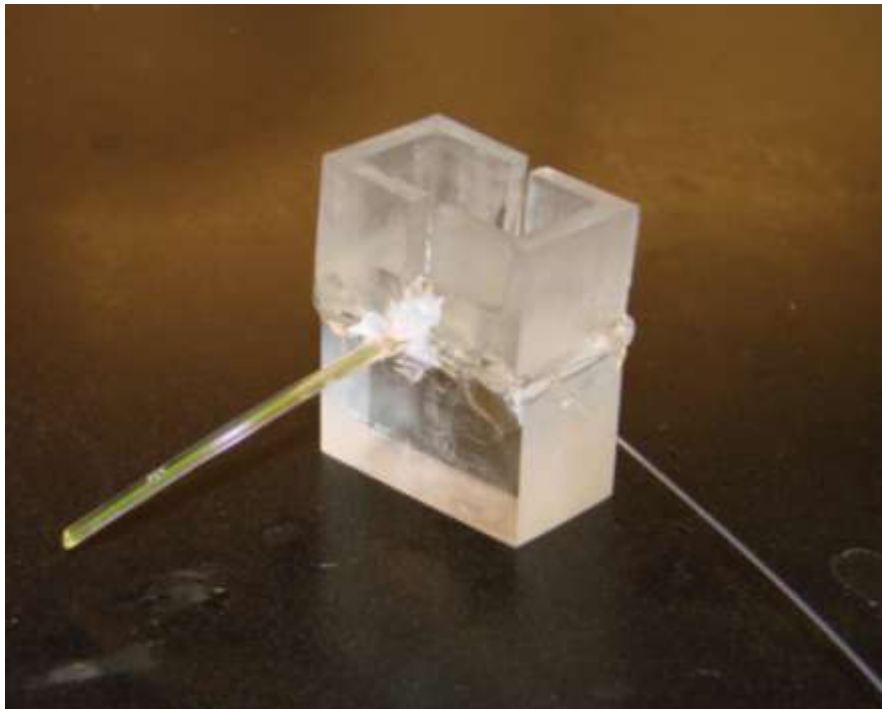


**Figure 6.3.** PDMS-embedded OFRR showing optical and fluidic input ports. Top structure is PDMS reservoir and bottom structure is acrylic holder for fiber prism.

### 6.2.2. Experimental protocol

To demonstrate the microfluidic lasers, dye (Coumarin 504, R6G, and LDS 722) in quinoline ( $n = 1.626$ ) is flowed through the OFRR at a rate of  $10 \mu\text{L}/\text{min}$  with a syringe pump and is excited by a 5-ns pulsed tunable OPO laser (Opotek, Vibrant, repetition rate: 10 Hz) from the side of the OFRR through PDMS. The microfluidic laser emission is coupled through the fiber and detected at the distal end of the fiber with a spectrometer (Ocean Optics HR4000 USB, spectral resolution: 3.7 nm).

### 6.3. Results

Figure 6.4 shows the R6G laser spectra for embedded OFRRs using a fiber prism (Fig. 6.4(a)) and a tapered fiber (Fig. 6.4(b)) to deliver the lasing output. The line width in Fig. 6.4(a) is approximately 8 nm, larger than the spectrometer resolution, indicating that the laser is operated at multi-mode lasing. However, the actual laser emission line from each individual WGM is too narrow to resolve. Note that the detected laser emission linewidth is broader when the laser is out-coupled with a fiber prism than with a tapered fiber, which is around 3.5 nm, limited by the spectrometer resolution. This discrepancy can be accounted for by considering the different out-coupling efficiencies between the fiber prism and tapered fiber for various WGMs. Since the fiber prism is made of a large fiber (200  $\mu\text{m}$  core) that supports multi-mode transmission, the WGMs having different propagation constants can always be phase-matched by the modes in the fiber prism. The corresponding light in those WGM can thus be coupled out and subsequently transmitted down the fiber with low loss [21, 255]. In contrast, the tapered fiber supports many fewer transmission modes and is therefore much more selective in picking up the WGMs. Only those that phase-match the modes in the tapered fiber can be efficiently coupled out. For the same reason, part of spontaneous emission, *i.e.*, the regular fluorescence, can be coupled out through the fiber prism, whereas in the tapered fiber case, only the laser emission is observed, which is in agreement with the previous observation when the OFRR-taper is in free space [250].

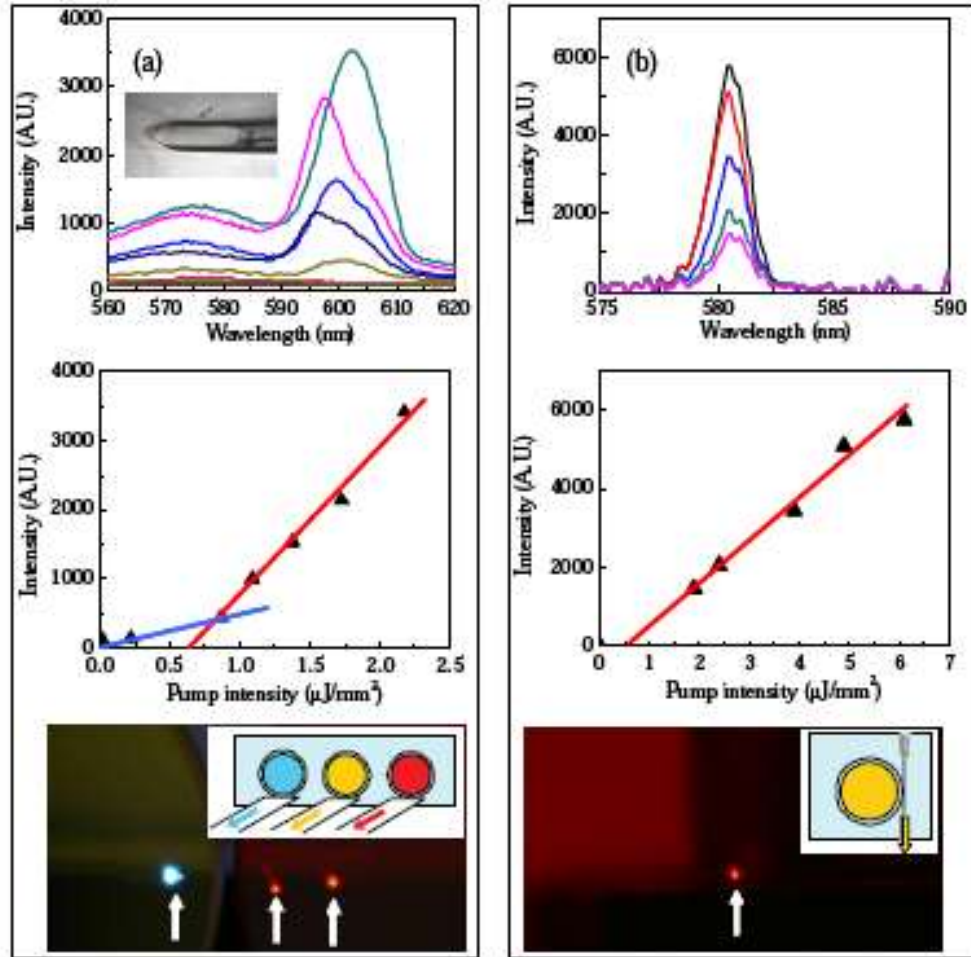


**Figure 6.4.** (a). Top: R6G WGM lasing spectrum collected with a fiber prism. The inset shows the picture of a fiber prism. Middle: Emission from the fiber prism vs. excitation intensity. Threshold is estimated to be  $0.7 \mu\text{J}/\text{mm}^2$ . Bottom: Photograph of three color simultaneous emission out of the fiber ends when three parallel OFRRs are filled with Coumarin 504 (left,  $\lambda_{\text{peak}}=480 \text{ nm}$ ), R6G (middle,  $\lambda_{\text{peak}}=600 \text{ nm}$ ), and LDS 722 (right,  $\lambda_{\text{peak}}=730 \text{ nm}$ ). A long-pass filter is used to remove the excitation light. (b) Top: R6G WGM lasing spectrum collected with a tapered fiber. Middle: Emission from the taper vs. excitation intensity. Threshold is estimated to be  $0.5 \mu\text{J}/\text{mm}^2$ . Bottom: Photograph of R6G laser emission from the end of a tapered fiber.

Figure 6.4 also shows the laser emission peak intensity versus the excitation intensity. The lasing threshold is estimated to be  $0.7 \mu\text{J}/\text{mm}^2$  and  $0.5 \mu\text{J}/\text{mm}^2$  for the fiber prism configuration and tapered fiber configuration, respectively. Although the lasing

threshold is over ten times higher than the best threshold reported for the OFRR laser in free space [250], it is still a few times lower than many other types of microfluidic lasers due to its high Q-factors, as discussed later. Note that the threshold reported here is a conservative estimation, as the light intensity is measured in front of the PDMS. The actual intensity impinged on the OFRR is expected to be lower.

The laser output from the fiber prism for 2 mM R6G is measured to be 80 nW (after the removal of the regular fluorescence signal), when the pump intensity is  $2.2 \mu\text{J}/\text{mm}^2$ , which corresponds to 8 nJ output per pulse. Considering the pump laser is impinging an area of  $200 \mu\text{m}$  by  $75 \mu\text{m}$ , the overall power extraction efficiency is 25%, much higher than the 1% efficiency reported in the microfluidic laser based on distributed-feedback grating cavity [257]. In reality, since only a layer of R6G molecules near the OFRR wall contribute to the laser emission, the actual power extraction efficiency should be much higher. Assuming that R6G molecules within a circular shell of  $3 \mu\text{m}$  in thickness (see the discussion for Fig. 6.6 later),  $75 \mu\text{m}$  in diameter, and  $200 \mu\text{m}$  in height participate in lasing and that the R6G absorption cross section is  $4.5 \times 10^{-16} \text{ cm}^2$  [258], a power extraction efficiency of 50% can be obtained, attesting to the highly efficient out-coupling [250].

To demonstrate the versatility and multiplexing in our device, three fiber prisms are polished simultaneously and brought into contact with three OFRRs before the whole system is embedded in PDMS, as illustrated in the bottom figure of Fig. 6.4(a). Three different dyes (Coumarin 504, R6G, and LDS 722) at a concentration of 2 mM in quinoline running through the OFRRs are excited with a 460 nm beam, which overlaps

with the absorption spectra of all three dyes. The bottom figure in Fig. 6.4(a) shows the photograph of the three-color laser emission out-coupled by fiber prisms. Color multiplexing can also be realized with taper fibers in replacement of fiber prisms. The bottom figure in Fig. 6.4(b) shows the photograph of laser emission from the tapered fiber when only one OFRR channel is excited. Unlike the light travelling in the fiber prism, which is protected by the fiber cladding, the light transmitted through the tapered fiber is exposed to the surrounding medium. However, it has been shown that low loss transmission can still be maintained when the taper is immersed in a low RI polymer [153, 259, 260]. Finally, color multiplexing can be achieved by running multiple dye through the same OFRR channel. Figure 6.5 shows that the laser emission from Coumarin 504 and R6G co-propagates along the same fiber.

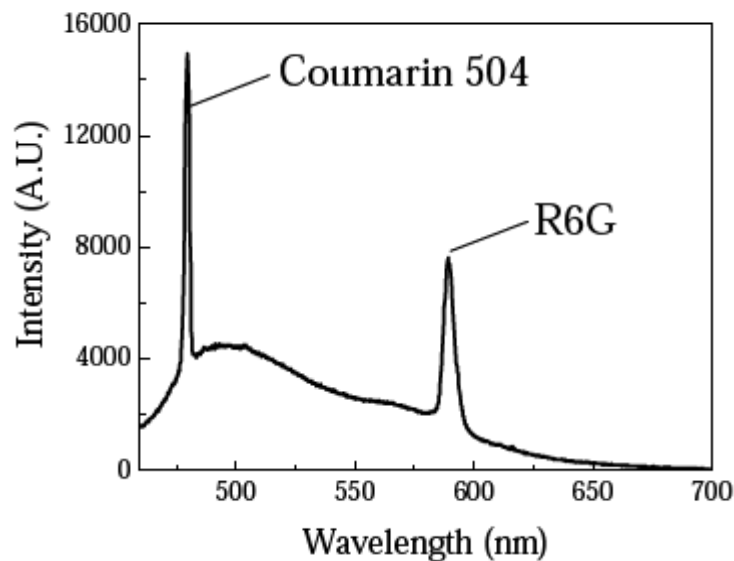


**Figure 6.5.** Spectrum of the OFRR laser when Coumarin 504 (1 mM) and R6G (1 mM) mixture is flowed through the OFRR. Excitation wavelength: 450 nm. Laser emission is out-coupled by a fiber prism.

To better understand the behavior of the WGMs in the embedded OFRR, we examine the radial intensity profile using a theoretical model based on Mie theory [254]. Figure 6.6 shows the radial distribution of the WGM of the 1st, 2nd, and 3rd order. All modes have strong electric field concentrated within 2-3  $\mu\text{m}$  near the wall surface, which interacts with the gain medium and provides the optical feedback for lasing. The intrinsic Q-factor for these modes, which is determined by the mode radiation loss, exceeds  $10^7$ , indicating that our device can potentially support high-Q modes. The actual Q-factor is measured by coupling the light from a 780 nm tunable diode laser (Toptica) into the OFRR through the tapered fiber using the same OFRR in Fig. 6.4(b). Based on the resonance linewidth in Fig. 6.7, the highest empty Q-factor when the OFRR is filled with quinoline without dye is approximately  $2.6 \times 10^6$ . Similar Q-factors are also obtained in the fiber prism case. Since the intrinsic Q-factors of higher order WGMs are lower than  $10^6$ , we believe that the laser emission observed in our experiment is from the three lowest order WGMs. While the measured Q-factor is substantially below the predicted intrinsic Q-factor, it is still a few orders of magnitude higher than that in other microfluidic resonators [261]. The Q-factor degradation is attributed to the absorption of quinoline and polymer, the roughness induced scattering loss at the OFRR and polymer boundary, and the fiber out-coupling loss.

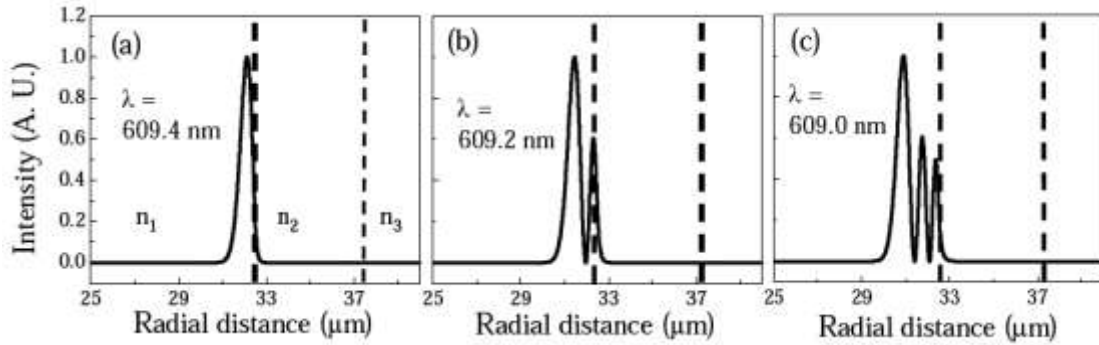


**Figure 6.6.** Radial distributions for (a) 1<sup>st</sup> order (b) 2<sup>nd</sup> order (c) and 3<sup>rd</sup> order modes. Intrinsic Q-factor for each exceeds  $10^7$ . OD = 75  $\mu\text{m}$ , wall thickness = 5  $\mu\text{m}$ ,  $n_1 = 1.626$ ,  $n_2 = 1.45$ ,  $n_3 = 1.41$ . Dashed lines are the OFRR inner and outer surface.

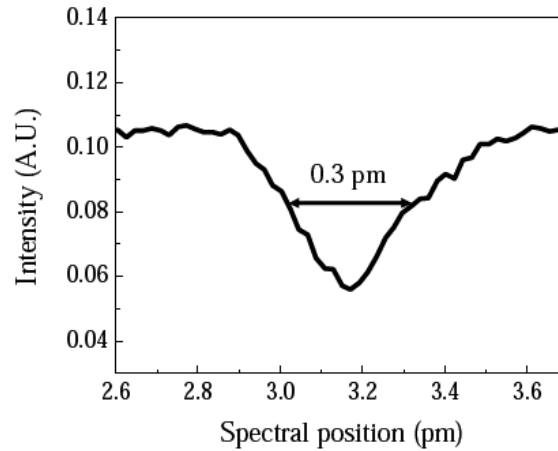


**Figure 6.7.** WGM resonance displaying a Q-factor of  $2.6 \times 10^6$ . Tunable diode laser wavelength is 780 nm.

Since the RI of PDMS is close to that of glass, the OFRR laser can also be achieved even in the absence of the glass wall. In Fig. 6.8, we used a structure similar to the one described in Fig. 6.1(a). A small metal rod of 800  $\mu\text{m}$  in diameter is used to define a circular hole in PDMS, which is removed after the polymer cured. The hole is subsequently filled with 0.5 mM R6G in quinoline. The laser emission can readily be seen from this OFRR. Demonstration of the OFRR laser in the absence of a glass capillary

enables the fabrication of the OFRR using soft lithographic technologies. However, directly exposing the polymer to organic solvents may degrade the polymer integrity over time, appropriate selection of the solvent therefore become important in this type of microfluidic laser.

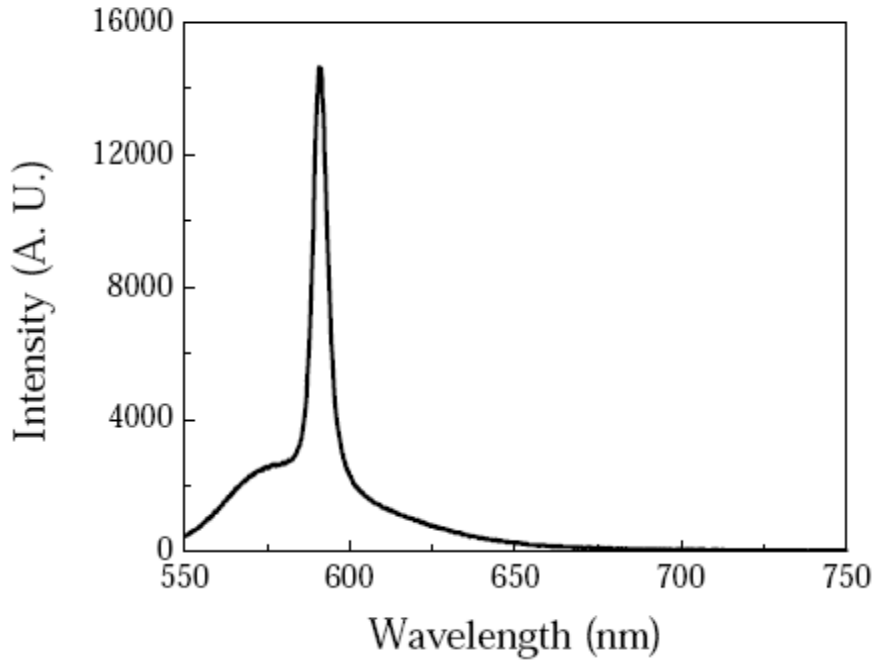


**Figure 6.8.** WGM lasing emission from a bare PDMS channel using 0.5 mM R6G. Excitation wavelength is 540 nm.

#### 6.4. Conclusions

To summarize, we have demonstrated an OFRR dye laser embedded in PDMS that has enhanced portability, mechanical stability, and compatibility with soft lithography based microfluidic technology. Even in PDMS, the OFRR still retains Q-factors larger than  $10^6$  and achieves a lasing threshold below  $1 \mu\text{J}/\text{mm}^2$ . The laser emission can be efficiently coupled out through a fiber prism or a tapered fiber, which provides a convenient means for on-chip light delivery. We have also demonstrated simultaneous

lasing of multiple dyes in individual capillaries as well as multiple excitation of a mixed dye solution, proving the versatility of this system. Our work opens a door to a new  $\mu$ TAS system that brings together the OFRR technology with the traditional polymer based microfluidic technology.

Future efforts will be focused on several important areas. We will improve the OFRR Q-factors by refining our fabrication method, which will result in an even lower lasing threshold. In the subsequent chapter, we discuss how to completely remove the need for a glass capillary element, improving the lab-on-a-chip compatibility and ease of fabrication. Additional optical functionalities such as in-line optical filter based on fiber Bragg gratings will be added to further enhance the device performance. Concurrent to these developments, applications of the embedded OFRRs in biological and chemical detection will also be pursued.

## CHAPTER 7

### PDMS-BASED MICROFLUIDIC LASERS WITH NOVEL OUTCOUPLING

#### 7.1. Motivation and need for novel outcoupling

One of the challenges with the optofluidic ring resonator (OFRR) dye lasers, however, is the efficient and directional outcoupling of the laser emission into a waveguide, which subsequently delivers the light to its destination (such as channels where bio/chemical sensing takes place). Unfortunately, by nature the emission from those ring resonator lasers is usually scattered omnidirectionally, limiting their usefulness. Recently, the OFRR laser emission has successfully been coupled into an optical fiber through direct coupling via a microknot ring resonator made out of a sub-micron-sized optical fiber [160] and through evanescent coupling where a tapered optical fiber is in contact with the ring resonator [247, 250]. While those demonstrations represent the OFRR laser emission into a solid waveguide, coupling of the OFRR laser into a liquid channel remains largely unexplored. The direct coupling between the OFRR and a liquid channel offers a number of benefits. (1) It enables the integration of the OFRR lasers with optofluidic components, *i.e.*, liquid channels, on one monolithic piece without mediation of solid-state optical components. (2) Many optofluidic technologies developed to date, such as refractive index (RI) tuning, can be employed to control the OFRR/waveguide coupling and the light in the liquid channel. (3) The laser light can be directly delivered to desired microfluidic locations for various applications in bio/chemical sensing and laser metrology in liquid.

Recently, Li et al. (2007) demonstrated such coupling between the liquid ring resonator and the liquid-filled waveguide [122]. However, in this structure, the microfluidic channel defining the ring resonator has a fluidic connection with the waveguide, meaning that dye fills both ring resonator and the waveguide. This design may be problematic, because dye in the waveguide will re-absorb the lasing signal. Moreover, in many applications, the presence of dyes in a liquid channel is highly undesirable, as it may contaminate optofluidic components, damage biological samples, and generate unwanted background signal.

We propose and demonstrate two schemes to couple the OFRR dye laser emission into an physically separated liquid waveguide channel. In the first scheme, as illustrated in Fig. 7.1(a) and (b), the liquid waveguide is placed on the side of the OFRR and they are separated by a solid-state gap. These designs have been submitted for publication [262]. Coupling is achieved through the evanescent interaction between the WGM in the OFRR and the mode in the liquid waveguide [248]. In the second scheme, as shown in Fig. 7.1(c), we employed a spiral ring resonator [234, 263], which can be described by  $r(\theta) = r_0(1 + \varepsilon\theta/2\pi)$ , where  $r$  and  $\theta$  are the spiral radius and the angle, respectively.  $r_0$  is the spiral initial radius and  $\varepsilon$  is the deformation parameter. The spiral ring resonator allows for unidirectional emission into a separate liquid waveguide using direct, non-evanescent butt-coupling, as opposed to the side-coupled design. Each of these schemes resolves the issues in the aforementioned structures, particularly the problem of outcoupling the laser emission into physically separated waveguides. They allow for independent engineering

and control of the laser cavity and liquid waveguide, thus significantly enhancing the versatility of the entire OFRR laser system.

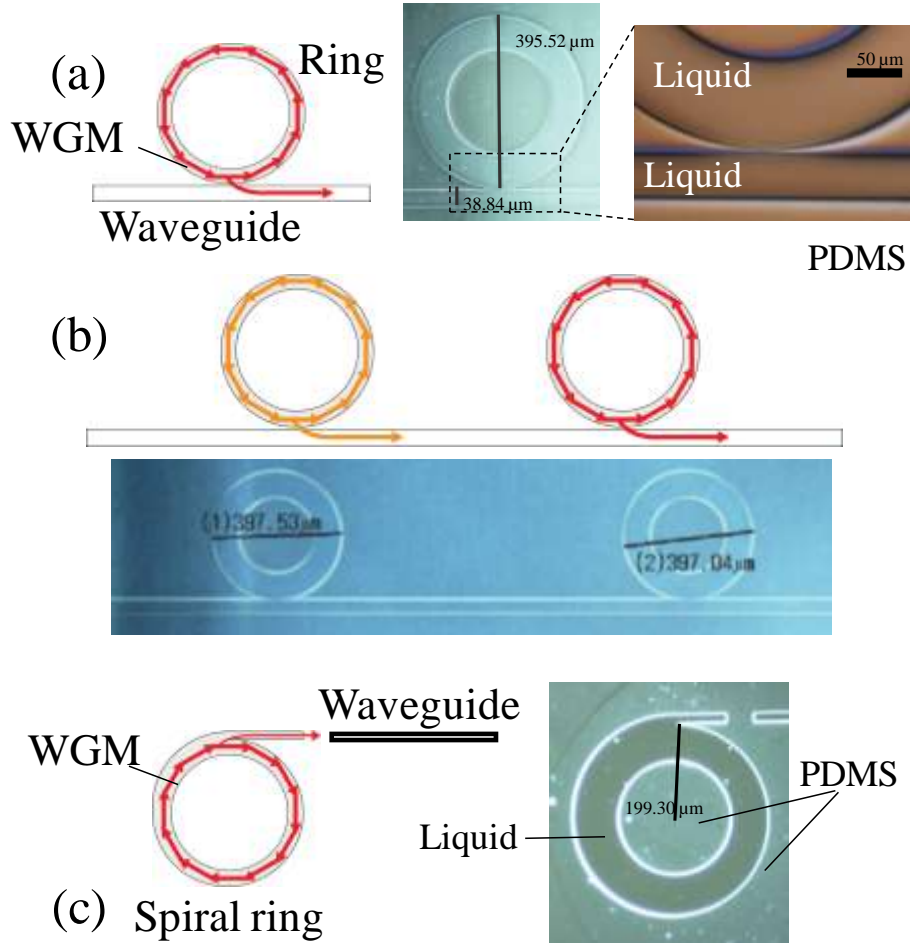


**Figure 7.1.** Schematic and corresponding image of single side-coupled OFRR laser (a), two side-coupled OFRR lasers (b), and a spiral OFRR (c). All the ring resonators are filled with dye in TEG whereas the waveguides are filled only with TEG. The magnified region in (a) shows the separation of the OFRR and the waveguide by a 2 μm PDMS gap.

## 7.2. Experimental methods

### 7.2.1. Materials and fabrication

We implemented the above schemes using an OFRR and a waveguide fabricated on a polydimethyl siloxane (PDMS slab). The side-coupled rings are designed to have an

outer diameter (OD) of approximately 400  $\mu\text{m}$ , an inner diameter (ID) of 240  $\mu\text{m}$ , and a depth of 10  $\mu\text{m}$ . The liquid channel has a width of 40  $\mu\text{m}$  and a depth of 10  $\mu\text{m}$ . The waveguide is separated from the ring by a PDMS gap of 2  $\mu\text{m}$  (Fig. 7.1(a)). The spiral ring resonator has an initial OD of 400  $\mu\text{m}$  and ID of 240  $\mu\text{m}$ .  $\varepsilon$  is chosen to be 0.1, which results in an output notch of 20  $\mu\text{m}$  in width. The notch is separated from the liquid filled waveguide by about 40  $\mu\text{m}$ . In both structures, the 240- $\mu\text{m}$  diameter central PDMS disk is small enough that it does not interact with the WGMs contributing to the lasing signal. Rather, their purpose is to exclude dye from the central regions that would contribute to unwanted fluorescence background.

Ensuring wall straightness and smoothness in the outer wall of the rings is critical to make sure that scattering is reduced and optical confinement is possible. In order to get a 3D view of these structures in PDMS, finished side-coupled and spiral rings were mounted on a laser interferometer. The resulting images are presented in Figs. 7.2 (a), (b), and (d). In these three figures the vertical axis is expanded to better reveal features on the walls. Fig. 7.2(a) shows an image of a side-coupled ring with a 2  $\mu\text{m}$  gap. This image shows that the gap is intact even at the thinnest part. Figs. 7.2(b) and (d) show a spiral ring and a zoomed-in image of its notch, respectively. It is observed that the corner that separates the waveguide stub from the ring is very sharp, which is an important characteristic for outcoupling. For all of these laser interferometer images, it can be seen that the walls are very smooth and straight. Fig. 7.2(c) shows a microscope image of the cross-section of a 40  $\mu\text{m}$  waveguide, further demonstrating how straight the walls are after fabrication and contact molding.

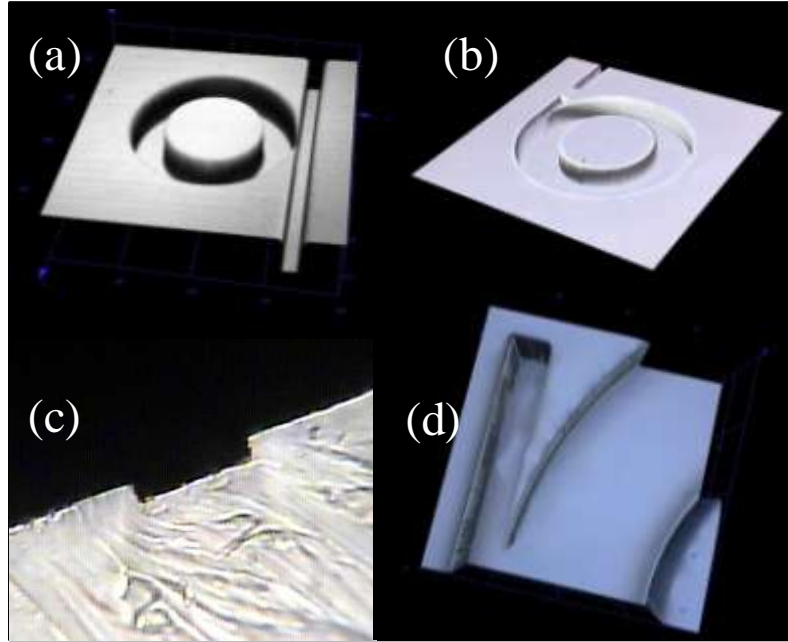


**Figure 7.2.** Laser interferometric images of a side-coupled ring (a) and a spiral ring (b). A microscope image of a waveguide cross-section shows wall straightness (c). A blow-up of the spiral ring image in (b) highlights the waveguide stub (d).

We fabricate a master mold on a silicon wafer using standard reactive ion etching procedures. The etched wafer is vacuum coated with trichlorosilane as a release layer. Finally, the wafer is coated with a 4 mm layer of mixed and degassed PDMS, which is subsequently heated at 75°C for 30 minutes before its release and treatment with a plasma cleaner.

### 7.2.2. Experimental protocol

The experimental setup is illustrated in Fig. 7.3(a). We use a micro-syringe to introduce R6G (or LDS 722) dissolved in tetraethylene glycol (TEG) into the OFRR and to fill the waveguide with TEG alone. Due to the plasma treatment, the solvent quickly

wicks to fill the entire structures. Inspection under a microscope shows no bubbles or leakage. TEG has a refractive index of approximately 1.46, slightly higher than that of PDMS (~1.40). Therefore, the liquid ring supports the WGMs and liquid channel is able to guide the light. The OFRR laser is pumped by a 10-ns pulsed optical parametric oscillator at 500 nm with a spot size of approximately 10 mm<sup>2</sup>. The emission is collected by an optical fiber (600 μm in core diameter) at the terminal of the liquid waveguide (see Fig. 7.3(a) and sent to a spectrometer (Horiba iHR550, ~0.1 nm spectral resolution) for post-analysis. The Q-factor of the side-coupled ring resonator and spiral resonator is approximately 5000 (limited by the spectrometer resolution) and 750, respectively.

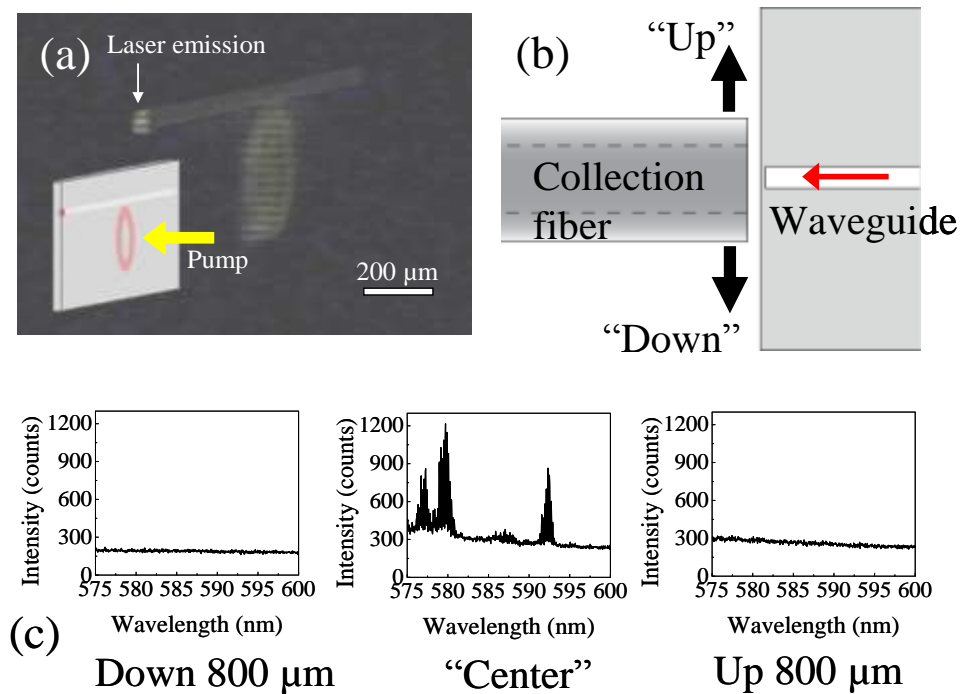


**Figure 7.3.** Demonstration of outcoupling of the OFRR laser emission into a TEG filled liquid waveguide. (a) Photograph of the OFRR and the waveguide during laser operation. Inset illustrates the experimental setup. (b) Alignment schematic of a collection fiber at the end of the waveguide. (c) Spectra with the collection fiber in and out of alignment.

### 7.3. Verification of output

We first investigate the side-coupled OFRR to verify lasing and to confirm the ability to evanescently couple the emission into the liquid waveguide. For this purpose, a single ring is filled with 2 mM R6G. When the OFRR laser is in operation, strong lasing output can be observed from the end of the waveguide in addition to the scattered light from the ring itself that contains both fluorescence and laser emission (Fig. 7.3(a)). In contrast, much less light is seen from the body of the waveguide (as opposed to the terminus), suggesting that (1) the ring and the waveguide are unconnected and (2) the light is directionally coupled into the waveguide. Note that while the side-coupling is bi-directional, only one end of the waveguide is imaged in Fig. 7.3(a).

To further confirm this directional coupling, a fiber is placed very close to the waveguide output and moved by small increments (Fig. 7.3(b)). As plotted in Fig. 7.3(c), groups of clustered laser peaks, resulting from the multi-transverse mode nature of the ring resonator [160, 233], emerge when the fiber is right at the waveguide. In contrast, when the fiber is slightly away from the waveguide, only weak and featureless background is picked up. This verifies that the laser emission is indeed coupled into and guided by the liquid waveguide. It should be noted that while the ring-waveguide coupling in air requires the ring-waveguide gap be smaller than one micrometer, efficient coupling can take place even with a relatively large gap when the ring and the waveguide are surrounded by PDMS because of the large extension of the electric field of the WGM and the waveguide mode resulting from the low index contrast, which has been demonstrated previously under similar circumstances [259].

## 7.4. Results

The side-coupling design allows for fabrication of a series of OFRRs along the same waveguide channel and independent control of each OFRR. Therefore, multiple color emission from different OFRRs can be coupled into a single waveguide.

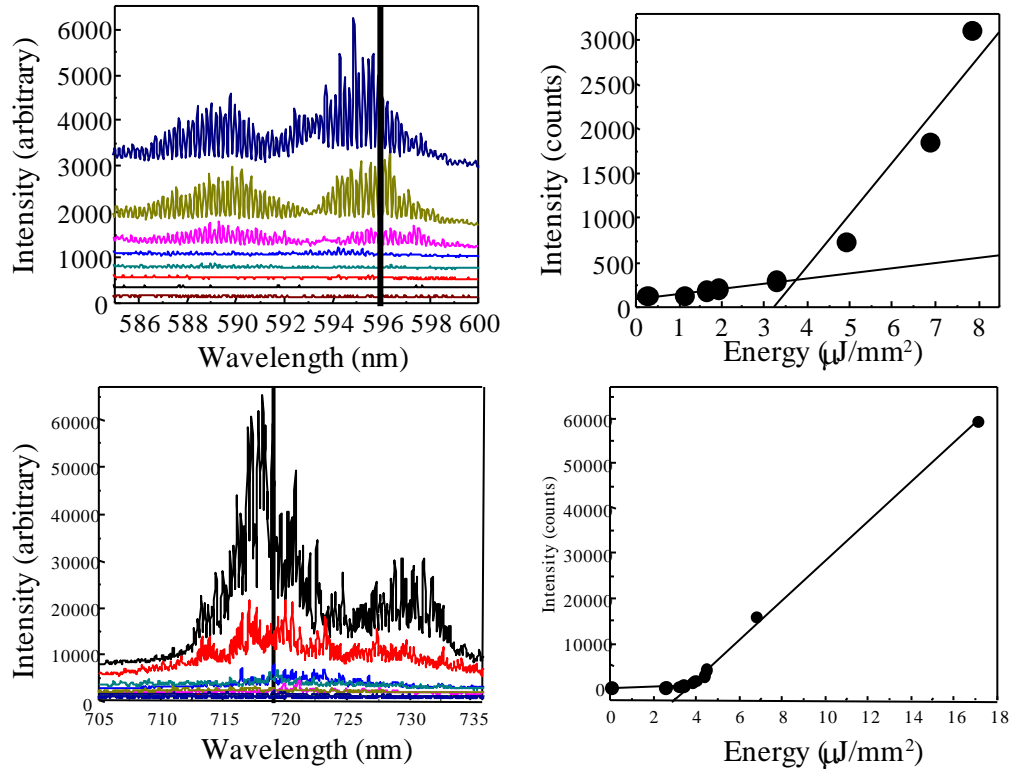


**Figure 7.4.** Concomitant lasing emission spectra collected from the waveguide for the dual ring configuration in which 2 mM R6G (a) and 2 mM LDS 722 (b) are injected into each ring, respectively. Both rings are simultaneously pumped. The spectra recorded for each pump intensity are vertically shifted for clarity. (c) and (d) are the corresponding laser emission intensity (at the wavelength marked by black vertical line in (a) and (b)) as a function of the pump energy density. The lasing threshold is 3.7  $\mu\text{J}/\text{mm}^2$  and 4.0  $\mu\text{J}/\text{mm}^2$  for R6G and LDS 722, respectively.

Furthermore, the emission from the upstream OFRR can be processed (such as amplification and filtering) by the downstream OFRRs. In Fig. 7.4, coupling of dual

emission from two rings to a single waveguide is achieved for the first time using 2 mM R6G for one ring and 2 mM LDS 722 for the adjacent one. Both OFRRs are simultaneously pumped and their emission can be observed concomitantly from the waveguide, as shown in Fig. 7.4(a) and (b). The lasing threshold is approximately  $3.7 \mu\text{J}/\text{mm}^2$  (Fig. 7.4(c)) and  $4.0 \mu\text{J}/\text{mm}^2$  (Fig. 7.4(d)) for R6G and LDS 722, respectively, on par with most of the optofluidic lasers [248, 261, 264].

In Fig. 7.5, we demonstrate another outcoupling scheme using a spiral OFRR. The spiral geometry is known to produce unidirectional emission through its terminal notch facet [234, 263], in contrast to bi-directional emission in the side-coupling design in Fig. 7.1(a). In addition, since the spiral OFRR uses butt-coupling, no stringent requirements on the gap between the ring and the side waveguide are needed, making the fabrication and microfluidic integration much easier. As shown in Fig. 7.5(a), when the spiral OFRR laser is in operation, strong laser emission can be observed at the end of the waveguide while the waveguide itself is nearly invisible, suggesting that the laser is coupled into and guided by the waveguide. Fig. 7.5(b) shows the actual lasing spectrum obtained from the end of this waveguide. The lasing threshold is approximately  $26 \mu\text{J}/\text{mm}^2$ , much higher than that for the side-coupled ring resonator. In addition, the laser spectrum appears at a lower wavelength. Both indicate that the spiral has a much lower Q-factor [250]. The lasing peaks are superimposed on a broad fluorescence background. The relatively large background is likely to come from the fluorescence in the notch portion of the spiral, whose emission can also be coupled into the waveguide. Reducing the notch size could minimize this fluorescence background, but it would also have an effect upon the laser

coupling and threshold. In contrast, the evanescent coupling scheme in Figs. 7.3 and 7.4 can significantly suppress the OFRR fluorescence background, as only the lasing modes can be coupled into and subsequently guided by the liquid waveguide. Fig. 7.6 shows a slightly better single-frame lasing spectrum from a different spiral with the same specifications. This spectrum shows stronger lasing peaks, likely due to minute differences in the fabrication process.

## 7.5. Conclusions

In summary, in this chapter we have presented two schemes for outcoupling the OFRR laser emission into a liquid channel using evanescent side-coupling and direct butt-coupling methods. These configurations enable physical separation of the fluids in the laser cavities and waveguides, allowing for independent control of each optofluidic component. The laser threshold is on the order of a few  $\mu\text{J}/\text{mm}^2$  for the side-coupled ring resonator and approximately  $26 \text{ mJ}/\text{mm}^2$  for the spiral ring resonator.

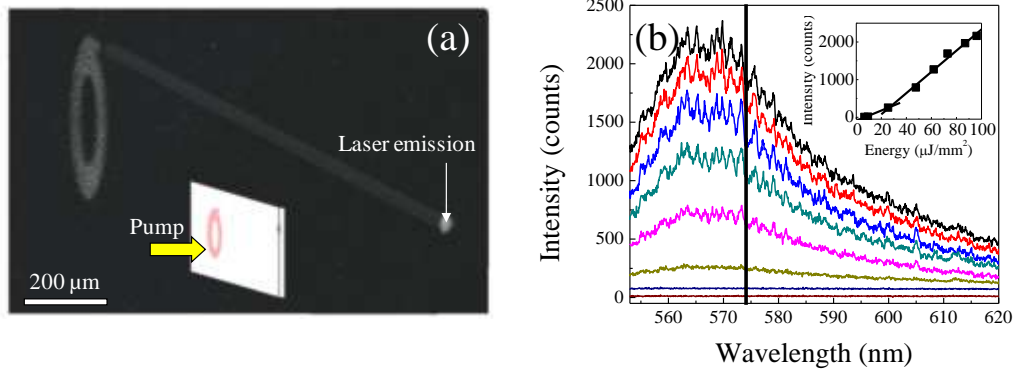


**Figure 7.5.** (a) Photograph of the spiral OFRR and the waveguide during laser operation. Inset shows the PDMS slab and pump beam orientation. (b) The corresponding laser emission spectra collected through the waveguide at different pump energy densities. Curves are vertically shifted for clarity. Inset is the corresponding laser emission intensity (at the wavelength marked by black vertical line) as a function of the pump energy density. The estimated lasing threshold is  $25.9 \mu\text{J}/\text{mm}^2$ .

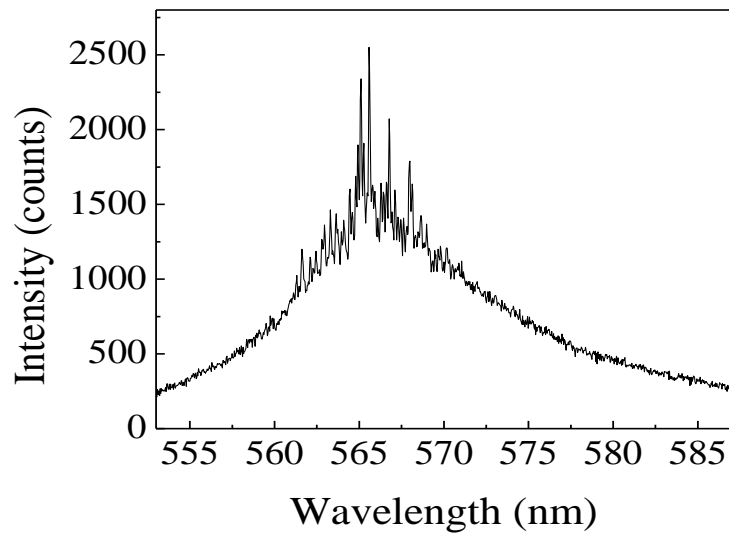


**Figure 7.6.** A single spectrum emitted from a spiral ring structure showing best recorded multi-mode structure.

Future work will involve generating a single-mode OFRR and dynamically tuning the laser wavelength. In addition, improvement in fabrication will increase the Q-factor, in particular in the spiral structure, thus lowering the lasing threshold. Finally, it will also be useful to coat the liquid channel with extremely low-index materials like Teflon [265] and nanoporous silicates [266] so that biological buffer (containing mainly water) can be used to guide the light in the liquid channel for many biochemical applications.

## CHAPTER 8

### SUMMARY AND FUTURE WORK

In the preceding chapters I have presented the detailed background and fundamental operating principles of the opto-fluidic ring resonator (OFRR). Characterization of the OFRR's response to thermal fluctuations was described in particular detail. Subsequently, two applications of the OFRR were described in detail, DNA methylation detection and microfluidic laser production.

The DNA methylation project approached the problem of determining the degree of methylation in an oligonucleotide using two distinct affinity methods. The first used an anti-methylcytidine antibody, which showed preferential affinity for single-stranded DNA. The second used a methyl-binding protein, which showed preferential affinity for double-stranded DNA. By binding these molecules to the inside of the OFRR using established covalent attachment methods, it is possible to create a very sensitive and specific tool that can discriminate between DNA molecules with small differences in methycytosine density. Such an approach lays the foundation for using the OFRR as a research tool to better understand the role of DNA methylation in disease development.

The second project investigated the problem of enhancing functionality and practical applications of ring-resonator-based microfluidic lasers. The first phase of the project looked at how an OFRR-based microfluidic laser could be embedded in PDMS. Lasing signal from the embedded structures was outcoupled using either fiber tapers or angle-polished fibers. Such structures proved to be uncommonly robust and were

demonstrated in both single-capillary and multi-capillary arrays.

The next step in microfluidic laser research looked at ways of creating opto-fluidic lasers in PDMS without the need for glass capillaries. Such a step makes the lasers compatible with lab-on-a-chip. Two geometries of PDMS ring-resonator lasers were constructed using DRIE and contact-molding which had distinctly different outcoupling modes. The first structure was a side-coupled ring, which utilized evanescent coupling to collect the laser signal. The second structure was a spiral ring, which utilized direct butt-coupling. While more difficult to fabricate, the side-coupled rings showed lower lasing thresholds, close to  $4 \mu\text{J}/\text{mm}^2$ , and had very little fluorescence background. The spiral ring had a lasing threshold closer to  $26 \mu\text{J}/\text{mm}^2$  due to intrinsically lower Q-factor and higher fluorescence background, but used a more convenient outcoupling method.

## REFERENCES

1. Lefevre-Seguin, V. and S. Haroche, *Towards cavity-QED experiments with silica microspheres*. Mater. Sci. Eng. B, 1997. **48**: p. 53-58.
2. Vernooy, D.W., A. Furusawa, N. Ph. Georgiades, V. S. Ilchenko and H. J. Kimble, *Cavity QED with high-Q whispering gallery modes*. Phys. Rev. A, 1998. **57**: p. R2293-R2296
3. Baer, T., *Continuous-wave laser oscillation in a Nd:YAG sphere*. Opt. Lett., 1987. **12**: p. 392-394.
4. Liu, X., W. Fang, Y. Huang, X. H. Wu, S. T. Ho, H. Cao and R. P. H. Chang, *Optically pumped ultraviolet microdisk laser on a silicon substrate*. Appl. Phys. Lett., 2004. **84**: p. 2488-2490.
5. Lin, H.-B. and A.J. Campillo, *Microcavity enhanced Raman gain*. Opt. Commun., 1997. **133**: p. 287-292.
6. Klug, M., S.I. Kalblukov, and B. Wellegehausen, *Cw hyper-Raman laser and four-wave mixing in atomic sodium*. Opt. Commun., 2005. **245**: p. 415-424.
7. Culverhouse, D., K. Kalli, and D.A. Jackson, *Stimulated Brillouin scattering ring resonator laser for SBS gain studies and microwave generation*. Electron. Lett., 1991. **27**: p. 2033-2035.
8. Cohen, D.A., M. Hossein-Zadeh, and A.F.J. Levi, *Microphotonic modulator for microwave receiver*. Electron. Lett., 2001. **37**: p. 300-301.
9. Little, B.E., S. T. Chu, P. P. Absil, J. V. Hryniewicz, F. G. Johnson, F. Seiferth, D. Gill, V. Van, O. King and M. Trakalo, *Very high-order microring resonator filters for WDM applications*. IEEE Photonic. Tech. L., 2004. **16**: p. 2263-2265.
10. Madsen, C.K., G. Lenz, A. J. Bruce, M. A. Cappuzzo, L. T. Gomez and R. E. Scotti, *Integrated all-pass filters for tunable dispersion and dispersion slope compensation*. IEEE Photonic. Tech. L., 1999. **11**: p. 1623-1625.
11. Heebner, J.E., R.W. Boyd, and Q.-H. Park, *Slow light, induced dispersion, enhanced nonlinearity, and optical solitons in a resonator-array waveguide*. Phys. Rev. E, 2002. **65**: p. 036619.

12. Del'Haye, P., A. Schliesser, O. Arcizet, T. Wilken, R. Holzwarth and T. J. Kippenberg, *Optical frequency comb generation from a monolithic microresonator*. Nature, 2007. **450**: p. 1214-1217.
13. Armenise, M.N., V. M. N. Passaro, F. DeLeonardis and M. Armenise, *Modeling and design of a novel miniaturized integrated optical sensor for gyroscope systems*. J. Lightwave Technol., 2001. **19**: p. 1476-1494.
14. Huston, A.L. and J.D. Eversole, *Strain-sensitive elastic scattering from cylinders*. Opt. Lett., 1993. **18**: p. 1104-1106.
15. Kippenberg, T.J., H. Rokhsari, T. Carmon, A. Scherer and K. J. Vahala, *Analysis of radiation-pressure induced mechanical oscillation of an optical microcavity*. Phys. Rev. Lett., 2005. **95**: p. 033901.
16. Ashkenazi, S., C-Y. Chao, L. J. Guo and M. O'Donnell, *Ultrasound detection using polymer microring optical resonator*. Appl. Phys. Lett., 2004. **85**: p. 5418-5420.
17. Sakai, Y., I. Yokohama, T. Kominato and S. Sudo, *Frequency stabilization of laser diode using a frequency-locked ring resonator to acetylene gas absorption lines*. IEEE Photonic. Tech. L., 1991. **3**: p. 868-870.
18. Psaltis, D., S.R. Quake, and C. Yang, *Developing optofluidic technology through the fusion of microfluidics and optics*. Nature, 2006. **442**: p. 381-386.
19. Monat, C., P. Domachuk, and B.J. Eggleton, *Integrated optofluidics: a new river of light*. Nat. Photonics, 2007. **1**: p. 106-114.
20. Horowitz, V.R., D.D. Awschalom, and S. Pennathur, *Optofluidics: field or technique?* Lab Chip, 2008. **8**: p. 1856-1863.
21. Hanumegowda, N.M., C. J. Stica, B. C. Patel, I. M. White and X. Fan, *Refractometric sensors based on microsphere resonators*. Appl. Phys. Lett., 2005. **87**: p. 201107.
22. Bernardi, A., S. Kiravittaya, A. Rastelli, R. Songmuang, D. J. Thurmer, M. Benyoucef and O. G. Schmidt, *On-chip Si/SiO<sub>x</sub> microtube refractometer*. Appl. Phys. Lett., 2008. **93**: p. 094106.
23. Zamora, V., A. Diez, M. V. Andres and B. Gimeno, *Refractometric sensor based on whispering-gallery modes of thin capillaries*. Opt. Express, 2008. **15**: p. 12011-12016.

24. Xu, F. and G. Brambilla, *Manufacture of 3-D microfiber coil resonators*. IEEE Photonic. Tech. L., 2007. **19**: p. 1481-1483.
25. Nitkowski, A., L. Chen, and M. Lipson, *Cavity-enhanced on-chip absorption spectroscopy using microring resonators*. Opt. Express, 2008. **16**: p. 11930-11936.
26. Blair, S. and Y. Chen, *Resonant-enhanced evanescent-wave fluorescence biosensing with cylindrical optical cavities*. Appl. Optics, 2001. **40**: p. 570-582.
27. Sennaroglu, A., A. Kiraz, M. A. Dundar, A. Kurt and A. L. Demirel, *Raman lasing near 630 nm from stationary glycerol-water microdroplets on a superhydrophobic surface*. Opt. Lett., 2007. **32**: p. 2197-2199.
28. White, I.M., J. Gohring, and X. Fan, *SERS-based detection in an optofluidic ring resonator platform*. Opt. Express, 2007. **15**: p. 17433-17442.
29. Ilchenko, V.S. and A.B. Matsko, *Optical resonators with whispering-gallery modes - part II: applications*. IEEE J. Sel. Top. Quant., 2006. **12**: p. 15-32.
30. Fan, X., I. M. White, S. I. Shopova, H. Zhu, J. D. Suter, and Y. Sun, *Sensitive optical biosensors for unlabeled targets: a review*. Anal. Chim. Acta, 2008. **620**: p. 8-26.
31. Gorodetsky, M.L. and V.S. Ilchenko, *Optical microsphere resonators: optimal coupling to high-Q whispering-gallery modes*. J. Opt. Soc. Am. B, 1999. **16**: p. 147-154.
32. Zhu, H., I. M. White, J. D. Suter, P. S. Dale and X. Fan, *Analysis of biomolecule detection with optofluidic ring resonator sensors*. Opt. Express, 2007. **15**: p. 9139-9146.
33. Vollmer, F., S. Arnold, D. Braun, I. Teraoka and A. Libchaber, *Multiplexed DNA quantification by spectroscopic shift of two microsphere cavities*. Biophys. J., 2003. **85**: p. 1974-1979.
34. Vollmer, F., D. Braun, A. Libchaber, M. Khoshsim, I. Teraoka and S. Arnold, *Protein detection by optical shift of a resonant microcavity*. Appl. Phys. Lett., 2002. **80**: p. 4057-4059.
35. Chao, C.-Y. and L.J. Guo, *Design and optimization of microring resonators in biochemical sensing applications*. J. Lightwave Technol., 2006. **24**: p. 1395-1402.
36. Suter, J.D., I. M. White, H. Zhu and X. Fan, *Thermal characterization of liquid core optical ring resonator sensors*. Appl. Optics, 2007. **46**: p. 389-396.

37. Han, M. and A. Wang, *Temperature compensation of optical microresonators using a surface layer with negative thermo-optic coefficient*. Opt. Lett., 2007. **32**: p. 1800-1802.
38. Armani, A.M., R. P. Kulkarni, S. E. Fraser, R. C. Flagan and K. J. Vahala, *Label-free, single-molecule detection with optical microcavities*. Science, 2007. **317**: p. 783-787.
39. He, L., Y-F. Xiao, C. Dong, J. Zhu, V. Gaddam and L. Yang, *Compensation of thermal refraction effect in high-Q toroidal microresonator by polydimethylsiloxane coating*. Appl. Phys. Lett., 2008. **93**: p. 201102.
40. Nadeau, J.L., V. S. Ilchenko, D. Kossakovski, G. H. Bearman and L. Maleki, *High-Q whispering-gallery mode sensor in liquids*. In *Proceedings of SPIE*. **4629** 2002. p. 172-180.
41. Armani, A.M. and K.J. Vahala, *Heavy water detection using ultra-high-Q microcavities*. Opt. Lett., 2006. **31**: p. 1896-1898.
42. Farca, G., S.I. Shopova, and A.T. Rosenberger, *Cavity-enhanced laser absorption spectroscopy using microresonator whispering-gallery modes*. Opt. Express, 2007. **15**: p. 17443-17448.
43. Hanumegowda, N.M., I. M. White, H. Oveys and X. Fan, *Label-free protease sensors based on optical microsphere resonators*. Sens. Lett., 2005. **3**: p. 1-5.
44. Teraoka, I., S. Arnold, and F. Vollmer, *Perturbation approach to resonance shifts of whispering-gallery modes in a dielectric microsphere as a probe of a surrounding medium*. J. Opt. Soc. Am. B, 2003. **20**: p. 1937-1946.
45. Arnold, S., M. Khoshsima, I. Teraoka, S. Holler and F. Vollmer, *Shift of whispering-gallery modes in microspheres by protein adsorption*. Opt. Lett., 2003. **28**: p. 272-274.
46. Grillet, C., S. N. Bian, E. C. Magi and B. J. Eggleton, *Fiber taper coupling to chalcogenide microsphere modes*. Appl. Phys. Lett., 2008. **92**: p. 171109.
47. Lutti, J., W. Langbein, and P. Borri, *A monolithic optical sensor based on whispering-gallery modes in polystyrene microspheres*. Appl. Phys. Lett., 2008. **93**: p. 151103.

48. Ma, X., J. Q. Lu, R. S. Brock, K. M. Jacobs, P. Yang and X-H. Hu, *Determination of complex refractive index of polystyrene microspheres from 370 to 1610 nm*. Phys. Med. Biol., 2003. **48**: p. 4165-4172.
49. Zijlstra, P., K.L. van der Molen, and A.P. Mosk, *Spatial refractive index sensor using whispering gallery modes in an optically trapped microsphere*. Appl. Phys. Lett., 2007. **90**: p. 161101.
50. Hanumegowda, N.M., I.M. White, and X. Fan, *Aqueous mercuric ion detection with microsphere optical ring resonator sensors*. Sens. Actuat. B, 2006. **120**: p. 207-212.
51. Snee, P.T., Y. Chan, D. G. Nocera, and M. G. Bawendi, *Whispering-gallery-mode lasing from a semiconductor nanocrystal/microsphere resonator composite*. Adv. Mater., 2004. **17**: p. 1131-1136.
52. Topolancik, J. and F. Vollmer, *Photoinduced transformations in bacteriorhodopsin membrane monitored with optical microcavities*. Biophys. J., 2007. **92**: p. 2223-2229.
53. Nuhiji, E. and P. Mulvaney, *Detection of unlabeled oligonucleotide targets using whispering gallery modes in single, fluorescent microspheres*. Small, 2007. **3**: p. 1408-1414.
54. Francois, A., S. Krishnamoorthy, and M. Himmelhaus. *Advances in label-free optical biosensing: direct comparison of whispering gallery mode sensors with surface plasmon resonance*. In *Single Molecule Spectroscopy and Imaging*. 2008. San Jose, CA: SPIE.
55. Zhu, H., J. D. Suter, I. M. White, and X. Fan, *Aptamer based microsphere biosensor for thrombin detection*. Sensors, 2006. **6**: p. 785-795.
56. Noto, M., D. Keng, I. Teraoka, and S. Arnold, *Detection of protein orientation on the silica microsphere surface using transverse electric/transverse magnetic whispering gallery modes*. Biophys. J., 2007. **92**: p. 4466-4472.
57. Becker, R.C. and F.A. Spencer, *Thrombin: structure, biochemistry, measurement, and status in clinical medicine*. J. Thromb. Thrombolys., 1998. **5**: p. 215-229.
58. Francois, A. and M. Himmelhaus, *Whispering gallery mode biosensor operated in the stimulated emission regime*. Appl. Phys. Lett., 2009. **94**: p. 031101.
59. Weller, A., F. C. Liu, R. Dahint, and M. Himmelhaus, *Whispering gallery mode biosensors in the low-Q limit*. Appl. Phys. B, 2008. **90**: p. 561-567.

60. Meissner, K.E. and A. Allen, *Whispering gallery mode biosensors using semiconductor quantum dots*. In *IEEE Sensors*. 2005: IEEE. p. 4-7.
61. Ren, H.-C., F. Vollmer, S. Arnold, and A. Libchaber, *High-Q microsphere biosensor - analysis for adsorption of rodlike bacteria*. *Opt. Express*, 2007. **15**: p. 17410-17423.
62. Vollmer, F., S. Arnold, and D. Keng, *Single virus detection from the reactive shift of a whispering-gallery mode*. *P. Natl. Acad. Sci. USA*, 2008. **105**: p. 20701-20704.
63. Keng, D., S. R. McAnanama, I. Teraoka, and S. Arnold, *Resonance fluctuations of a whispering gallery mode biosensor by particles undergoing Brownian motion*. *Appl. Phys. Lett.*, 2007. **91**: p. 103902.
64. Norris, D.J., M. Kuwata-Gonokami, and W.E. Moerner, *Excitation of a single molecule on the surface of a spherical microcavity*. *Appl. Phys. Lett.*, 1997. **71**: p. 297-299.
65. White, I.M., N.M. Hanumegowda, and X. Fan, *Subfemtomole detection of small molecules with microsphere sensors*. *Opt. Lett.*, 2005. **30**: p. 3189-3191.
66. Lin, H.-B., J.D. Eversole, and A.J. Campillo, *Spectral properties of lasing microdroplets*. *J. Opt. Soc. Am. B*, 1992. **9**: p. 43-50.
67. Saito, M., H. Shimatani, and H. Naruhashi, *Tunable whispering gallery mode emission from a microdroplet in elastomer*. *Opt. Express*, 2008. **16**: p. 11915-11919.
68. Tzeng, H.-M., K. F. Wall, M. B. Long, and R. K. Chang, *Laser emission from individual droplets at wavelengths corresponding to morphology-dependent resonances*. *Opt. Lett.*, 1984. **9**: p. 499-501.
69. Lin, H.-B., A. L. Huston, B. L. Justus, and A. J. Campillo, *Some characteristics of a droplet whispering-gallery-mode laser*. *Opt. Lett.*, 1986. **11**: p. 614-616.
70. Tanyeri, M., R. Perron, and I.M. Kennedy, *Lasing droplets in a microfabricated channel*. *Opt. Lett.*, 2007. **32**: p. 2529-2531.
71. Hossein-Zadeh, M. and K.J. Vahala, *Fiber-taper coupling to whispering-gallery modes of fluidic resonators embedded in a liquid medium*. *Opt. Express*, 2006. **14**: p. 10800-10810.

72. Dorrer, C. and J. Ruhe, *Advancing and receding motion of droplets on ultrahydrophobic post surfaces*. Langmuir, 2006. **22**: p. 7652-7657.
73. Kiraz, A., S. Doganay, A. Kurt, and A. L. Demirel, *Enhanced energy transfer in single glycerol/water microdroplets standing on a superhydrophobic surface*. Chem. Phys. Lett., 2007. **444**: p. 181-185.
74. Kiraz, A., Y. Karadag, and A.F. Coskun, *Spectral tuning of liquid microdroplets standing on a superhydrophobic surface using electrowetting*. Appl. Phys. Lett., 2008. **92**: p. 191104.
75. Arnold, S. and L.M. Folan, *Fluorescence spectrometer for a single electrostatically levitated microparticle*. Rev. Sci. Instrum., 1986. **57**: p. 2250-2253.
76. Azzouz, H., L. Alkhafadiji, S. Balslev, J. Johansson, N. A. Mortensen, S. Nilsson, and A. Kristensen, *Levitated droplet dye laser*. Opt. Express, 2006. **14**: p. 4374-4379.
77. Hopkins, R.J., L. Mitchem, A. D. Ward, and J. P. Reid, *Control and characterization of a single aerosol droplet in a single-beam gradient-force optical trap*. Phys. Chem. Chem. Phys., 2004. **6**: p. 4924-4927.
78. Barnes, M.D., K. C. Ng, W. B. Whitten, J. M. Ramsey, *Detection of single Rhodamine 6G molecules in levitated microdroplets*. Anal. Chem., 1993. **65**: p. 2360-2365.
79. Mugele, F. and J.-C. Baret, *Electrowetting: from basics to applications*. J. Phys.-Condens. Mat., 2005. **17**: p. R705-R774.
80. Stone, J., *Measurements of the absorption of light in low-loss liquids*. J. Opt. Soc. Am., 1972. **62**: p. 327-333.
81. Tanyeri, M. and I.M. Kennedy, *Detecting single bacterial cells through optical resonances in microdroplets*. Sens. Lett., 2008. **6**: p. 326-329.
82. Tanyeri, M., D. Dosev, and I.M. Kennedy. *Chemical and biological sensing through optical resonances in pendant droplets*. In *Proceedings of the SPIE*. 2005. **6008**: p. 60800Q.
83. White, I.M., H. Oveys, and X. Fan, *Liquid-core optical ring-resonator sensors*. Opt. Lett., 2006. **31**: p. 1319-1321.

84. Shopova, S.I., Y. Sun, A. T. Rosenberger, and X. Fan, *Highly sensitive tuning of coupled optical ring resonators by microfluidics*. *Microfluid. Nanofluid.*, 2009. **6**: p. 425-429.
85. White, I.M., H. Zhu, J. D. Suter, N. M. Hanumegowda, H. Oveys, M. Zourob, and X. Fan, *Refractometric sensors for lab-on-a-chip based on optical ring resonators*. *IEEE Sens. J.*, 2007. **7**: p. 28-35.
86. Zhu, H., I. M. White, J. D. Suter, and X. Fan, *Phage-based label-free biomolecule detection in an opto-fluidic ring resonator*. *Biosens. Bioelectron.*, 2008. **24**: p. 461-466.
87. Zhu, H., I. M. White, J. D. Suter, M. Zourob, and X. Fan, *Integrated refractive index optical ring resonator detector for capillary electrophoresis*. *Anal. Chem.*, 2007. **79**: p. 930-937.
88. Zhu, H., I. M. White, J. D. Suter, M. Zourob, and X. Fan, *Opto-fluidic micro-ring resonator for sensitive label-free viral detection*. *Analyst*, 2008. **133**: p. 356-360.
89. Yang, G., I.M. White, and X. Fan, *An opto-fluidic ring resonator biosensor for the detection of organophosphorus pesticides*. *Sens. Actuat. B*, 2008. **133**: p. 105-112.
90. Suter, J.D., D. J. Howard, H. Shi, C. W. Caldwell, and X. Fan, *Label-free DNA methylation analysis using opto-fluidic ring resonators*. *Biosens. Bioelectron.*, In press, 2010.
91. Smith, D.D., H. Chang, and K.A. Fuller, *Whispering-gallery mode splitting in coupled microresonators*. *J. Opt. Soc. Am. B*, 2003. **20**: p. 1967-1974.
92. Suter, J.D., I. M. White, H. Zhu, H. Shi, C. W. Caldwell, and X. Fan, *Label-free quantitative DNA detection using the liquid core optical ring resonator*. *Biosens. Bioelectron.*, 2008. **23**: p. 1003-1009.
93. Kipp, T., H. Welsch, Ch. Strelow, Ch. Heyn, and D. Heitmann, *Optical modes in semiconductor microtube ring resonators*. *Phys. Rev. Lett.*, 2006. **96**: p. 077403.
94. Schmidt, O.G. and K. Eberl, *Thin solid films roll up into nanotubes*. *Nature*, 2001. **410**: p. 168.
95. Prinz, V.Y., V. A. Seleznev, A. K. Gutakovskiy, A. V. Chehovskiy, V. V. Preobrazhenskii, M. A. Putyato, and T. A. Gavrilova, *Free-standing and overgrown InGaAs/GaAs nanotubes, nanohelices and their arrays*. *Physica E*, 2000. **6**: p. 828-831.

96. Songmuang, R., C. Deneke, and O.G. Schmidt, *Rolled-up micro- and nanotubes from single-material thin films*. Appl. Phys. Lett., 2006. **89**: p. 223109.
97. Mendach, S., R. Songmuang, S. Kiravittaya, A. Rastelli, M. Benyoucef, and O. G. Schmidt, *Light emission and wave guiding of quantum dots in a tube*. Appl. Phys. Lett., 2006. **88**: p. 111120.
98. Songmuang, R., A. Rastelli, S. Mendach, Ch. Deneke, and O. G. Schmidt, *From rolled-up Si microtubes to SiO<sub>2</sub>/Si optical ring resonators*. Microelectron. Eng., 2007. **84**: p. 1427-1430.
99. Sumetsky, M., R. S. Windeler, Y. Dulashko, and X. Fan, *Optical liquid ring resonator sensor*. Opt. Express, 2007. **15**: p. 14376-14381.
100. Ling, T. and L.J. Guo, *A unique resonance mode observed in a prism-coupled micro-tube resonator sensor with superior index sensitivity*. Opt. Express, 2007. **15**: p. 17424-17432.
101. Shopova, S.I., I. M. White, Y. Sun, H. Zhu, X. Fan, G. Frye-Mason, A. Thompson, and S-J. Ja, *On-column micro gas chromatography detection with capillary-based optical ring resonators*. Anal. Chem., 2008. **80**: p. 2232-2238.
102. Sun, Y. and X. Fan, *Analysis of ring resonators for chemical vapor sensor development*. Opt. Express, 2008. **16**: p. 10254-10268.
103. Sun, Y., S. I. Shopova, G. Frye-Mason, and X. Fan, *Rapid chemical-vapor sensing using optofluidic ring resonators*. Opt. Lett., 2008. **33**: p. 788-790.
104. Xia, Y., J. J. McClelland, R. Gupta, D. Qin, X-M. Zhao, L. L. Sohn, R. J. Celotta, and G. M. Whitesides, *Replica molding using polymeric materials: a practical step toward nanomanufacturing*. Adv. Mater., 1997. **9**: p. 147-149.
105. Hua, F., Y. Sun, A. Gaur, M. A. Meitl, L. Bilhaut, L. Rotkina, J. Wang, P. Geil, M. Shim, and J. A. Rogers, *Polymer imprint lithography with molecular-scale resolution*. Nano Lett., 2004. **4**: p. 2467-2471.
106. Xu, D.-X., A. Densmore, A. Delage, P. Waldron, R. McKinnon, S. Janz, J. Lapointe, G. Lopinski, T. Mischki, E. Post, P. Cheben, and J. H. Schmid, *Folded cavity SOI microring sensors for high sensitivity and real time measurement of biomolecular binding*. Opt. Express, 2008. **16**: p. 15137-15148.
107. De Vos, K., I. Bartolozzi, E. Schacht, P. Bienstman, R. Baets, *Silicon-on-insulator microring resonator for sensitive and label-free biosensing*. Opt. Express, 2007. **15**: p. 7610-7615.

108. Xu, D.-X., A. Densmore, P. Waldron, J. Lapointe, E. Post, A. Delage, S. Janz, P. Cheben, J. H. Schmid, and B. Lamontagne, *High bandwidth SOI photonic wire ring resonators using MMI couplers*. Opt. Express, 2007. **15**: p. 3149-3155.
109. Dai, D., L. Yang, and S. He, *Ultrasmall thermally tunable microring resonator with a submicrometer heater on Si nanowires*. J. Lightwave Technol., 2008. **26**: p. 704-709.
110. Passaro, V.M.N., F. Dell'Olio, and F. DeLeonardis, *Ammonia optical sensing by microring resonators*. Sensors, 2007. **7**: p. 2741-2749.
111. Martinez, L. and M. Lipson, *High confinement suspended micro-ring resonators in silicon-on-insulator*. Opt. Express, 2006. **14**: p. 6259-6263.
112. Baehr-Jones, T., M. Hochberg, C. Walker, and A. Scherer, *High-Q ring resonators in thin silicon-on-insulator*. Appl. Phys. Lett., 2004. **85**: p. 3346-3347.
113. Almeida, V.R., C. A. Barrios, R. R. Panepucci, M. Lipson, M. A. Foster, D. G. Ouzounov, and A. L. Gaeta, *All-optical switching on a silicon chip*. Opt. Lett., 2004. **29**: p. 2867-2869.
114. Padigi, S.K., K. Asante, V. S. R. Kovvuri, R. K. K. Reddy, A. La Rosa, and S. Prasad, *Micro-photonic cylindrical waveguide based protein biosensor*. Nanotechnology, 2006. **17**: p. 4384-4390.
115. Niehusmann, J., A. Vorckel, P. H. Bolivar, T. Wahlbrink, W. Henschel, and H. Kurz, *Ultrahigh-quality-factor silicon-on-insulator microring resonator*. Opt. Lett., 2004. **29**: p. 2861-2863.
116. Passaro, V.M.N. and F. DeLeonardis, *Modeling and design of a novel high-sensitivity electric field silicon-on-insulator sensor based on a whispering-gallery-mode resonator*. IEEE J. Sel. Top. Quant., 2006. **12**: p. 124-133.
117. Chao, C.-Y., W. Fung, and L.J. Guo, *Polymer microring resonators for biochemical sensing applications*. IEEE J. Sel. Top. Quant., 2006. **12**: p. 134-142.
118. Chao, C.-Y. and L.J. Guo, *Polymer microring resonators fabricated by nanoimprint technique*. J. Vac. Sci. Technol. B, 2002. **20**: p. 2862-2866.
119. Lee, H.-P., J.-J. Park, H.-H. Ryoo, S. G. Lee, O. B. Hoan, E.-H. Lee, *Resonance characteristics of waveguide-coupled polyimide microring resonator*. Opt. Mater., 2002. **21**: p. 535-541.

120. Shaforost, E.N., N. Klein, S. A. Vitusevich, A. Offenhausser, and A. A. Barannik, *Nanoliter liquid characterization by open whispering-gallery mode dielectric resonators at millimeter wave frequencies*. J. Appl. Phys., 2008. **104**: p. 074111.
121. Schweinsberg, A., S. Hocde, N. N. Lepeshkin, R. W. Boyd, C. Chase, and J. E. Fajardo, *An environmental sensor based on an integrated optical whispering gallery mode disk resonator*. Sens. Actuat. B, 2007. **123**: p. 727-732.
122. Li, Z., Z. Zhang, A. Scherer, and D. Psaltis, *Optofluidic microring dye laser*. in *IEEE/LEOS Summer Topical Meetings*. 2007. Portland, OR: IEEE. p. 70-71.
123. Robinson, J.T., L. Chen, and M. Lipson, *On-chip gas detection in silicon optical microcavities*. Opt. Express, 2008. **16**: p. 4296-4301.
124. Ghulinyan, M., D. Navarro-Urrios, and A. Pitanti, *Whispering-gallery modes and light emission from a Si-nanocrystal-based single microdisk resonator*. Opt. Express, 2008. **16**: p. 13218-13224.
125. Yalcin, A., K. C. Popat, J. C. Aldridge, T. A. Desai, J. Hryniewicz, N. Chbouki, B. E. Little, O. King, V. Van, S. Chu, D. Gill, M. Anthes-Washburn, M. S. Unlu, and B. B. Goldberg, *Optical sensing of biomolecules using microring resonators*. IEEE J. Sel. Top. Quant., 2006. **12**: p. 148-155.
126. Rahachou, A.I. and I.V. Zozoulenko, *Effects of boundary roughness on a Q factor of whispering-gallery-mode lasing microdisk cavities*. J. Appl. Phys., 2003. **94**: p. 7929-7931.
127. Chao, C.-Y. and L.J. Guo, *Reduction of surface scattering loss in polymer microrings using thermal-reflow techniques*. IEEE Photonic. Tech. L., 2004. **16**: p. 1498-1500.
128. Boyd, R.W. and J.E. Heebner, *Sensitive disk resonator photonic biosensor*. Appl. Optics, 2001. **40**: p. 5742-5747.
129. Boyd, R.W., J. E. Heebner, N. N. Lepeshkin, Q-H. Park, A. Schweinsberg, G. W. Wicks, A. S. Baca, J. E. Fajardo, R. R. Hancock, M. A. Lewis, R. M. Boysel, M. Quesada, R. Welty, A. R. Bleier, J. Treichler, and R. E. Slusher, *Nanofabrication of optical structures and devices for photonics and biophotonics*. J. Mod. Optic., 2003. **50**: p. 15-17.
130. Ramachandran, A., S. Wang, J. Clarke, S. J. Ja, D. Goad, L. Wald, E. M. Flood, E. Knobbe, J. V. Hryniewicz, S. T. Chu, D. Gill, W. Chen, O. King, and B. E. Little, *A universal biosensing platform based on optical micro-ring resonators*. Biosens. Bioelectron., 2008. **23**: p. 939-944.

131. Almeida, V.R., Q. Xu, C. A. Barrios, and M. Lipson, *Guiding and confining light in void nanostructure*. Opt. Lett., 2004. **29**: p. 1209-1211.
132. Barrios, C.A., M. J. Banuls, V. Gonzalez-Pedro, K. B. Gylfason, B. Sanchez, A. Griol, A. Maquieira, H. Sohlstrom, M. Holgado, and R. Casquel, *Label-free optical biosensing with slot-waveguides*. Opt. Lett., 2008. **33**: p. 708-710.
133. Barrios, C.A., K. B. Gylfason, B. Sanchez, A. Griol, H. Sohlstrom, M. Holgado, and R. Casquel, *Slot-waveguide biochemical sensor*. Opt. Lett., 2007. **32**: p. 3080-3082.
134. Barrios, C.A., K. B. Gylfason, B. Sanchez, A. Griol, H. Sohlstrom, M. Holgado, and R. Casquel, *Slot-waveguide biochemical sensor: erratum*. Opt. Lett., 2008. **33**: p. 2554-2555.
135. Dai, D. and S. He, *Low-index-material-based nano-slot waveguide with quasi-Bragg-reflector buffer*. Electron. Lett., 2008. **44**: p. 1354-1356.
136. Dai, D. and S. He, *Highly-sensitive sensor with large measurement range realized with two cascaded-microring resonators*. Opt. Commun., 2007. **279**: p. 89-93.
137. Vivien, L., D. Marris-Morini, A. Griol, K. B. Gylfason, D. Hill, J. Alvarez, H. Sohlstrom, J. Hurtado, D. Bouville, and E. Cassan, *Vertical multiple-slot waveguide ring resonators in silicon nitride*. Opt. Express, 2008. **16**: p. 17237-17242.
138. Kim, G-D., G-S. Son, H-S. Lee, K-D. Kim, S-S. Lee, *Integrated photonic glucose biosensor using a vertically coupled microring resonator in polymers*. Opt. Commun., 2008. **281**: p. 4644-4647.
139. Scheuer, J., W. M. J. Green, G. A. DeRose, and A. Yariv, *InGaAsP annular Bragg lasers: theory, applications, and modal properties*. IEEE J. Sel. Top. Quant., 2005. **11**: p. 476-484.
140. Scheuer, J. and A. Yariv, *Annular Bragg defect mode resonators*. J. Opt. Soc. Am. B, 2003. **20**: p. 2285-2291.
141. Scheuer, J., W.M.J. Green, and A. Yariv. *Annular Bragg resonators (ABR) - the ideal tool for biochemical sensing, nonlinear optics and cavity QED*. 2006. San Jose, CA: SPIE. p. 61230S.
142. Ilchenko, V.S., M. L. Gorodetsky, X. S. Yao, and L. Maleki, *Microtorus: a high-finesse microcavity with whispering-gallery modes*. Opt. Lett., 2001. **26**: p. 256-

- 258.
143. Kippenberg, T.J., S.M. Spillane, and K.J. Vahala, *Demonstration of ultra-high-Q small mode volume toroid microcavities on a chip*. Appl. Phys. Lett., 2004. **85**: p. 6113-6115.
  144. Armani, A.M., T. J. Kippenberg, S. M. Spillane, and K. J. Vahala, *Ultra-high-Q toroidal microcavity on a chip*. Nature, 2003. **421**: p. 925-928.
  145. Armani, A.M., A. Srinivasan, and K.J. Vahala, *Soft lithographic fabrication of high Q polymer microcavity arrays*. Nano Lett., 2007. **7**: p. 1823-1826.
  146. Armani, A.M., D. K. Armani, B. Min, K. J. Vahala, and S. M. Spillane, *Ultra-high-Q-microcavity operation in H<sub>2</sub>O and D<sub>2</sub>O*. Appl. Phys. Lett., 2005. **87**: p. 151118.
  147. Kippenberg, T.J., S. M. Spillane, D. K. Armani, and K. J. Vahala, *Fabrication and coupling to planar high-Q silica disk microcavities*. Appl. Phys. Lett., 2003. **83**: p. 797-799.
  148. Kulkarni, R.P., S.E. Fraser, and A.M. Armani, *Characterization of high-Q optical microcavities using confocal microscopy*. Opt. Lett., 2008. **33**: p. 2931-2933.
  149. Martin, A.L., D. K. Armani, L. Yang, and K. J. Vahala, *Replica-molded high-Q polymer microresonators*. Opt. Lett., 2004. **29**: p. 533-535.
  150. Tong, L., R. R. Gattass, J. B. Ashcom, S. He, J. Lou, M. Shen, I. Maxwell, and E. Mazur, *Subwavelength-diameter silica wires for low-loss optical wave guiding*. Nature, 2003. **426**: p. 816-819.
  151. Sumetsky, M., *Optical fiber microcoil resonator*. Opt. Express, 2004. **12**: p. 2303-2316.
  152. Xu, F. and G. Brambilla. *Embedded optical microfiber coil resonator*. In *OECC/IOOC*. 2007. Yokohama, Japan.
  153. Xu, F. and G. Brambilla, *Embedding optical microfiber coil resonators in teflon*. Opt. Lett., 2007. **32**: p. 2164-2166.
  154. Xu, F. and G. Brambilla, *Demonstration of a refractometric sensor based on optical microfiber coil resonator*. Appl. Phys. Lett., 2008. **92**: p. 101126.
  155. Xu, F., P. Horak, and G. Brambilla, *Optical microfiber coil resonator refractometric sensor*. Opt. Express, 2007. **15**: p. 7888-7893.

156. Xu, F., V. Pruneri, V. Finazzi, and G. Brambilla, *An embedded optical nanowire loop resonator refractometric sensor*. Opt. Express, 2008. **16**: p. 1062-1067.
157. Vienne, G., P. Grelu, X. Pan, Y. Li, and L. Tong, *Theoretical study of microfiber resonator devices exploiting a phase shift*. J. Opt. A-Pure Appl. Op., 2008. **10**: p. 025303.
158. Vienne, G., Y. Li, and L. Tong, *Effect of host polymer on microfiber resonator*. IEEE Photonic. Tech. L., 2007. **19**: p. 1386-1388.
159. Sumetsky, M., Y. Dulashko, J. M. Fini, A. Hale, and D. J. DiGiovanni, *The microfiber loop resonator: theory, experiment, and application*. J. Lightwave Technol., 2006. **24**: p. 242-250.
160. Jiang, X., Q. Song, L. Xu, J. Fu, and L. Tong, *Microfiber knot dye laser based on the evanescent-wave-coupled gain*. Appl. Phys. Lett., 2007. **90**: p. 233501.
161. Sumetsky, M., Y. Dulashko, J. M. Fini, and A. Hale, *Optical microfiber loop resonator*. Appl. Phys. Lett., 2005. **86**: p. 161108.
162. Stokes, L.F., M. Chodorow, and H.J. Shaw, *All-single-mode fiber resonator*. Opt. Lett., 1982. **7**: p. 288-290.
163. Caspar, C. and E.-J. Bachus, *Fibre-optic micro ring-resonator with 2 mm diameter*. Electron. Lett., 1989. **25**: p. 1506-1508.
164. Jiang, X., L. Tong, G. Vienne, X. Guo, A. Tsao, Q. Yang, and D. Yang, *Demonstration of optical microfiber knot resonators*. Appl. Phys. Lett., 2006. **88**: p. 223501.
165. Vollmer, F. and S. Arnold, *Whispering-gallery-mode biosensing: label-free detection down to single molecules*. Nat. Methods, 2008. **5**: p. 591-596.
166. Cocorullo, G., F. G. Della Corte, I. Rendina, and P. M. Sarro, *Thermo-optic effect exploitation in silicon microstructures*. Sens. Actuat. A, 1998. **71**: p. 19-26.
167. Hohlfeld, D., M. Epmeier, and H. Zappe, *A thermally tunable, silicon based optical filter*. Sens. Actuat. A, 2003. **103**: p. 93-99.
168. Veldhuis, G.J., O. Parriaux, H. J. W. M. Hoekstra, and P. V. Lambeck, *Sensitivity enhancement in evanescent optical waveguide sensors*. J. Lightwave Technol., 2000. **18**: p. 677-682.

169. Okamoto, K., *Fundamentals of Optical Waveguides*. 2000, Academic Press.
170. Michie, A., J. Canning, K. Lyytikainen, M. Aslund, and J. Digweed, *Temperature independent highly birefringent photonic crystal fiber*. *Opt. Express*, 2004. **12**: p. 5160-5165.
171. Ghosh, G., *Temperature dispersion of refractive indexes in some silicate fiber glasses*. *IEEE Photonic. Tech. L.*, 1994. **6**: p. 431-433.
172. Linde, D.R., ed. *The CRC Handbook of Chemistry and Physics*. 2005, CRC.
173. Wray, J.H., *Refractive index of several glasses as a function of wavelength and temperature*. *J. Opt. Soc. Am.*, 1969. **59**: p. 774-776.
174. Jewell, J.M., C. Askins, and I.D. Aggarwal, *Interferometric method for concurrent measurement of thermo-optic and thermal expansion coefficients*. *Appl. Optics*, 1991. **30**: p. 3656-3660.
175. Ghosh, G., M. Endo, and T. Iwasaki, *Temperature-dependent Sellmeier coefficients and chromatic dispersions for some optical fiber glasses*. *J. Lightwave Technol.*, 1994. **12**: p. 1338-1342.
176. Bohren, C.F. and D.R. Huffman, eds. *Absorption and scattering of light by small particles*. 1983, Wiley: New York.
177. Longtin, J.P. and C.-H. Fan, *Precision laser-based concentration and refractive index measurement of liquids*. *Microscale Thermophys. Eng.*, 1998. **2**: p. 261-272.
178. Christopoulos, T.K., *Nucleic acid analysis*. *Anal. Chem.*, 1999. **71**: p. 425R-438R.
179. Fortina, P., S. Surrey, and L.J. Kricka, *Molecular diagnostics: hurdles for clinical implementation*. *Trends Mol. Med.*, 2002. **8**: p. 264-266.
180. Luong, J.H., P. Bouvrett, and K.B. Male, *Developments and applications of biosensors in food analysis*. *Trends Biotechnol.*, 1997. **15**: p. 369-377.
181. Gill, P., A.J. Jeffreys, and D.J. Werrett, *Forensic application of DNA 'fingerprints'*. *Nature*, 1985. **318**: p. 577-579.
182. Guo, Z., R. A. Guilfoyle, A. J. Thiel, R. Wang, and L. M. Smith, *Direct fluorescence analysis of genetic polymorphisms by hybridization with oligonucleotide*. *Nucleic Acids Res.*, 1994. **22**: p. 5456-5465.

183. Charles, P.T., G. J. Vora, J. D. Andreadis, A. J. Fortney, C. E. Meador, C. S. Dulcey, and D. A. Stenger, *Fabrication and surface characterization of DNA microarrays using amine- and thio- terminated oligonucleotide probes*. *Langmuir*, 2003. **19**: p. 1586-1591.
184. Cox, W.G. and V.L. Singer, *Fluorescent DNA hybridization probe preparation using amine modification and reactive dye coupling*. *Biotechniques*, 2004. **36**: p. 114-122.
185. Lin, B., J. Qiu, J. Gerstenmeier, P. Li, H. Pien, J. Pepper, B. Cunningham, *A label-free optical technique for detecting small molecule interactions*. *Biosens. Bioelectron.*, 2002. **17**: p. 827-834.
186. Ramachandran, N., D. N. Larson, P. R. H. Stark, E. Hainsworth, and J. LaBaer, *Emerging tools for real-time label-free detection of interactions on functional protein microarrays*. *FEBS J.*, 2005. **272**: p. 5412-5425.
187. Homola, J., S.S. Yee, and G. Gauglitz, *Surface plasmon resonance sensors: review*. *Sens. Actuat. B*, 1999. **54**: p. 3-15.
188. Chinowsky, T.M., J. G. Quinn, D. U. Bartholomew, R. Kaiser, and J. L. Elkind, *Performance of the Spreeta 2000 integrated surface plasmon resonance affinity sensor*. *Sens. Actuat. B*, 2003. **91**: p. 266-274.
189. Fan, X., I. M. White, H. Zhu, J. D. Suter, and H. Oveys, *Overview of novel integrated optical ring resonator bio/chemical sensors*. 2007: SPIE. p. 64520M.
190. He, L., M. D. Musick, S. R. Nicewarner, F. G. Salinas, S. J. Benkovic, M. J. Natan, and C. D. Keating, *Colloidal Au-enhanced surface plasmon resonance for ultrasensitive detection of DNA hybridization*. *J. Am. Chem. Soc.*, 2000. **122**: p. 9071-9077.
191. Sepulveda, B., J. S. del Rio, M. Moreno, F. J. Blanco, K. Mayora, C. Dominguez, and L. M. Lechuga, *Optical biosensor microsystems based on the integration of highly sensitive Mach-Zehnder interferometer devices*. *J. Opt. A-Pure Appl. Op.*, 2006. **8**: p. S561-S566.
192. Ymeti, A., J. Greve, P. V. Lambeck, T. Wink, S. W. F. M. van Hovell, T. A. M. Beumer, R. R. Wijn, R. G. Heideman, V. Subramaniam, and J. S. K, *Fast, ultrasensitive virus detection using a Young interferometer sensor*. *Nano Lett.*, 2007. **7**: p. 394-397.
193. Zuker, M., *Mfold web server for nucleic acid folding and hybridization prediction*.

- Nucleic Acids Res., 2003. **31**: p. 3406-3415.
194. Jones, P.A. and P.W. Laird, *Cancer epigenetics comes of age*. Nat. Genet., 1999. **21**: p. 163-167.
195. Gitan, R.S., H. Shi, C-M. Chen, P. S. Yan, and T. H-M. Huang, *Methylation-specific oligonucleotide microarray: a new potential for high-throughput methylation analysis*. Genome Res., 2002. **12**: p. 158-164.
196. Halperin, A., A. Buhot, and E.B. Zhulina, *On the hybridization isotherms of DNA microarrays: the Langmuir model and its extensions*. J. Phys. Condens. Matter, 2006. **18**: p. S463-S490.
197. Lehr, H.-P., M. Reimann, A. Brandenburg, G. Sulz, and H. Klapproth, *Real-time detection of nucleic acid interactions by total internal reflection fluorescence*. Anal. Chem., 2003. **75**: p. 2414-2420.
198. Michel, W., T. Mai, T. Naiser, and A. Ott, *Optical study of DNA surface hybridization reveals DNA surface density as a key parameter for microarray hybridization kinetics*. Biophys. J., 2007. **92**: p. 999-1004.
199. Nicolai, T., L. Van Dijk, J. A. P. P. Van Dijk, and J. A. M. Smit, *Molecular mass characterization of DNA fragments by gel permeation chromatography using a low-angle laser light scattering detector*. J. Chromatogr., 1987. **389**: p. 286-292.
200. White, I.M., H. Oveys, X. Fan, T. L. Smith, and J. Zhang, *Integrated multiplexed biosensors based on liquid core optical ring resonators and antiresonant reflecting optical waveguides*. Appl. Phys. Lett., 2006. **89**: p. 191106.
201. Jones, P.A. and S.B. Baylin, *The fundamental role of epigenetic events in cancer*. Nat. Rev. Genet., 2002. **3**: p. 415-428.
202. Egger, G., G. Liang, A. Aparicio, and P. A. Jones, *Epigenetics in human disease and prospects for epigenetic therapy*. Nature, 2004. **429**: p. 457-463.
203. Bird, A., *DNA methylation patterns and epigenetic memory*. Gene Dev., 2002. **16**: p. 6-21.
204. Baylin, S.B. and J.G. Herman, *DNA hypermethylation in tumorigenesis: epigenetics joins genetics*. Trends Genet., 2000. **16**: p. 168-174.
205. Kane, M.F., M. Loda, G. M. Gaida, J. Lipman, R. Mishra, H. Goldman, J. M. Jessup, and R. Kolodner, *Methylation of the hMLH1 promoter correlates with lack of expression of hMLH1 in sporadic colon tumors and mismatch repair-defective human tumor cell lines*. Cancer Res., 1997. **57**: p. 808-811.

206. Herman, J.G., A. Umar, K. Polyak, J. R. Graff, N. Ahuja, J-P. J. Issa, S. Markowitz, J. K. V. Willson, S. R. Hamilton, K. W. Kinzler, M. F. Kane, R. D. Kolodner, B. Vogelstein, T. A. Kunkel, and S. B. Baylin, *Incidence and functional consequences of hMLH1 promoter hypermethylation in colorectal carcinoma*. P. Natl. Acad. Sci. USA, 1998. **95**: p. 6870-6875.
207. Herman, J.G., J. R. Graff, S. Myohanen, B. D. Nelkin, and S. B. Baylin, *Methylation-specific PCR: a novel PCR assay for methylation status of CpG islands*. P. Natl. Acad. Sci. USA, 1996. **93**: p. 9821-9826.
208. Kelsey, G., D. Bodle, H. J. Miller, C. V. Beechey, C. Coombes, J. Peters, and C. M. Williamson, *Identification of imprinted loci by methylation-sensitive representational difference analysis: application to mouse distal chromosome 2*. Genomics, 1999. **62**: p. 129-138.
209. Fraga, M.F. and M. Esteller, *DNA methylation: a profile of methods and applications*. Biotechniques, 2002. **33**: p. 632-649.
210. Nelson, P.S., T.S. Papas, and C.W. Schweinfest, *Restriction endonuclease cleavage of 5-methyl-deoxycytosine hemimethylated DNA at high enzyme-to-substrate ratios*. Nucleic Acids Res., 1993. **21**: p. 681-686.
211. Bruce, S., K. Hannula-Jouppi, C. M. Lindgren, M. Lipsanen-Nyman, and J. Kere, *Restriction site-specific methylation studies of imprinted genes with quantitative real-time PCR*. Clin. Chem., 2008. **54**: p. 491-499.
212. Feng, F., H. Wang, L. Han, and S. Wang, *Fluorescent conjugated polyelectrolyte as an indicator for convenient detection of DNA methylation*. J. Am. Chem. Soc., 2008. **130**: p. 11338-11343.
213. Flusberg, B.A., D. R. Webster, J. H. Lee, K. J. Travers, E. C. Olivares, T. A. Clark, J. Korlach, and S. W. Turner, *Direct detection of DNA methylation during single-molecule, real-time sequencing*. Nat. Methods, 2010. **7**: p. 461-465.
214. Hendrich, B. and A. Bird, *Identification and characterization of a family of mammalian methyl-CpG binding proteins*. Mol. Cell. Biol., 1998. **18**: p. 6538-6547.
215. Wade, P.A., *Methyl CpG-binding proteins and transcriptional repression*. Bioessays, 2001. **23**: p. 1131-1137.

216. Meehan, R.R., J. D. Lewis, S. McKay, E. L. Kleiner, and A. P. Bird, *Identification of a mammalian protein that binds specifically to DNA containing methylated CpGs*. Cell, 1989. **58**: p. 499-507.
217. Rauch, T. and G.P. Pfeifer, *The MIRA method for DNA methylation analysis*, in *DNA methylation: methods and protocols*, J. Tost, Ed. 2009, Humana Press.
218. Jacinto, F.V., E. Ballestar, and M. Esteller, *Methyl-DNA immunoprecipitation (MeDIP): hunting down the DNA methylome*. Biotechniques, 2008. **44**: p. 35-43.
219. Maki, W.C. and N.N. Mishra, *Nanowire-transistor based ultra-sensitive DNA methylation detection*. Biosens. Bioelectron., 2008. **23**: p. 780-787.
220. Yu, Y., S. Blair, D. Gillespie, R. Jensen, D. Myszka, A. H. Badran, I. Ghosh, and A. Chagovetz, *Direct DNA methylation profiling using methyl binding domain proteins*. Anal. Chem., 2010. **82**: p. 5012-5019.
221. Gohring, J., P.S. Dale, and X. Fan, *Detection of HER2 breast cancer biomarker using the opto-fluidic ring resonator biosensor*. Sens. Actuat. B, 2010. **146**: p. 226-230.
222. Zhu, H., P. S. Dale, C. W. Caldwell, and X. Fan, *Rapid and label-free detection of breast cancer biomarker CA15-3 in clinical human serum samples with opto-fluidic ring resonator sensors*. Anal. Chem., 2009. **81**: p. 9858-9865.
223. Valinluck, V., P. Liu, J. I. Kang Jr., A. Burdzy, and L. C. Sowers, *5-halogenated pyrimidine lesions within a CpG sequence context mimic 5-methylcytosine by enhancing the binding of the methyl-CpG-binding domain of methyl-CpG-binding protein 2 (MeCP2)*. Nucleic Acids Res., 2005. **33**: p. 3057-3064.
224. Proll, J., M. Fodermayr, C. Wechselberger, P. Pammer, M. Sonnleitner, O. Zach, and D. Lutz, *Ultra-sensitive immunodetection of 5-methyl cytosine for DNA methylation analysis on oligonucleotide microarrays*. DNA Res., 2006. **13**: p. 37-42.
225. Tatematsu, K., T. Yamazaki, and F. Ishikawa, *MBD2-MBD3 complex binds to hemi-methylated DNA and forms a complex containing DNMT1 at the replication foci in late S phase*. Genes Cells, 2000. **5**: p. 677-688.
226. Garrett, C.G.B., W. Kaiser, and W.L. Bond, *Stimulated emission into optical whispering modes of spheres*. Phys. Rev., 1961. **124**: p. 1807-1809.

227. Sasagawa, K., Z. Yonezawa, J. Ohta, and M. Nunoshita, *Control of microsphere lasing wavelength using  $\lambda/4$ -shifted distributed feedback resonator*. Electron. Lett., 2003. **39**: p. 1817-1819.
228. Sandoghdar, V., F. Treussart, J. Hare, V. Lefevre-Seguin, J-M. Raimond, and S. Haroche, *Very low threshold whispering-gallery-mode microsphere laser*. Phys. Rev. A, 1996. **54**: p. R1777-R1780.
229. Wang, Y.Z., B. L. Lu, Y. Q. Li, and Y. S. Liu, *Observation of cavity quantum-electrodynamic effects in a Nd:glass microsphere*. Opt. Lett., 1995. **20**: p. 770-772.
230. Michler, P., A. Kiraz, L. Zhang, C. Becher, E. Hu, and A. Imamoglu, *Laser emission from quantum dots in microdisk structures*. Appl. Phys. Lett., 2000. **77**: p. 184-186.
231. Moon, H-J., G-W. Park, S-B. Lee, K. An, J-H. Lee, *Laser oscillations of resonance modes in a thin gain-doped ring-type cylindrical microcavity*. Opt. Commun., 2004. **235**: p. 401-407.
232. Kippenberg, T.J., J. Kalkman, A. Polman, and K. J. Vahala, *Demonstration of an erbium-doped microdisk laser on a silicon chip*. Phys. Rev. A, 2006. **74**: p. 051802.
233. Frolov, S.V., M. Shkunov, Z. V. Vardeny, and K. Yoshino, *Ring microlasers from conducting polymers*. Phys. Rev. B, 1997. **56**: p. R4363-R4366.
234. Wu, X., H. Li, L. Liu, and L. Xu, *Unidirectional single-frequency lasing from a ring-spiral coupled microcavity laser*. Appl. Phys. Lett., 2008. **93**: p. 081105.
235. Schafer, J., J. P. Mondia, R. Sharma, Z. H. Lu, A. S. Susha, A. L. Rogach, and L. J. Wang, *Quantum dot microdrop laser*. Nano Lett., 2008. **8**: p. 1709-1712.
236. Cheung, J.L., A. S. Kwok, K. A. Juvan, D. H. Leach, and R. K. Chang, *Stimulated low-frequency emission from anisotropic molecules in microdroplets*. Chem. Phys. Lett., 1993. **213**: p. 309-314.
237. Snow, J.B., S.-X. Qian, and R.K. Chang, *Stimulated Raman scattering from individual water and ethanol droplets at morphology-dependent resonances*. Opt. Lett., 1985. **10**: p. 37-39.
238. An, K. and H.-J. Moon, *Laser oscillations with pumping-independent ultrahigh cavity quality factors in evanescent-wave-coupled-gain microsphere dye lasers*. J. Phys. Soc. Jpn., 2003. **72**: p. 773-776.

239. Lin, H.-B., J. D. Eversole, A. J. Campillo, and J. P. Barton, *Excitation localization principle for spherical microcavities*. Opt. Lett., 1998. **23**: p. 1921-1923.
240. Qian, S.-X., J. B. Snow, H-M. Tzeng, and R. K. Chang, *Lasing droplets: highlighting the liquid-air interface by laser emission*. Science, 1986. **231**: p. 486-488.
241. Kiraz, A., A. Sennaroglu, S. Doganay, M. A. Dundar, A. Kurt, H. Kalaycioglu, and A. L. Demirel, *Lasing from single, stationary, dye-doped glycerol/water microdroplets located on a superhydrophobic surface*. Opt. Commun., 2007. **276**: p. 145-148.
242. Kwok, A.S. and R.K. Chang, *Stimulated resonance Raman scattering of Rhodamine 6G*. Opt. Lett., 1993. **18**: p. 1703-1705.
243. Lin, H.-B. and A.J. Campillo, *Cw nonlinear optics in droplet microcavities displaying enhanced gain*. Phys. Rev. Lett., 2004. **73**: p. 2440-2443.
244. Matsko, A.B., A. A. Savchenkov, R. J. Letargat, V. S. Ilchenko, and L. Maleki, *On cavity modification of stimulated Raman scattering*. J. Opt. B - Quantum S. O., 2003. **5**: p. 272-278.
245. Qian, S.-X. and R.K. Chang, *Multiorder stokes emission from micrometer-size droplets*. Phys. Rev. Lett., 1986. **56**: p. 926-929.
246. Qian, S.-X., J.B. Snow, and R.K. Chang, *Coherent Raman mixing and coherent anti-Stokes Raman scattering from individual micrometer-size droplets*. Opt. Lett., 1985. **10**: p. 499-501.
247. Shopova, S.I., H. Zhu, and X. Fan, *Optofluidic ring resonator based dye laser*. Appl. Phys. Lett., 2007. **90**: p. 221101.
248. Suter, J.D., Y. Sun, D. J. Howard, J. A. Viator, and X. Fan, *PDMS embedded optofluidic microring resonator lasers*. Opt. Express, 2008. **16**: p. 10248-10253.
249. Moon, H.-J., Y.-T. Chough, and K. An, *Cylindrical microcavity laser based on the evanescent-wave coupled gain*. Phys. Rev. Lett., 2000. **85**: p. 3161-3164.
250. Lacey, S., I. M. White, Y. Sun, S. I. Shopova, J. M. Cupps, P. Zhang, and X. Fan, *Versatile opto-fluidic ring resonator lasers with ultra-low threshold*. Opt. Express, 2007. **15**: p. 15523-15530.

251. Knight, J.C., H. S. T. Driver, R. J. Hutcheon, and G. N. Robertson, *Core-resonance capillary-fiber whispering-gallery-mode laser*. Opt. Lett., 1992. **17**: p. 1280-1282.
252. Knight, J.C., H.S.T. Driver, and G.N. Robertson, *Morphology-dependent resonances in a cylindrical dye microlaser: mode assignments, cavity  $Q$  values, and critical dye concentrations*. J. Opt. Soc. Am. B, 1994. **11**: p. 2046-2053.
253. Shopova, S.I., J. M. Cupps, P. Zhang, E. P. Henderson, S. Lacey, and X. Fan, *Opto-fluidic ring resonator lasers based on highly efficient resonant energy transfer*. Opt. Express, 2007. **15**: p. 12735-12742.
254. White, I.M., J. Gohring, Y. Sun, G. Yang, S. Lacey, and X. Fan, *Versatile waveguide-coupled opto-fluidic devices based on liquid core optical ring resonators*. Appl. Phys. Lett., 2007. **91**: p. 241104.
255. Ilchenko, V.S., X.S. Yao, and L. Maleki, *Pigtailing the high- $Q$  microsphere cavity: a simple fiber coupler for optical whispering-gallery modes*. Opt. Lett., 1999. **24**: p. 723-725.
256. Schueller, O.J.A., X-M. Zhao, G. M. Whitesides, S. P. Smith, and M. Prentiss, *Fabrication of liquid-core waveguides by soft lithography*. Adv. Mater., 1999. **11**: p. 37-41.
257. Balslev, S. and A. Kristensen, *Microfluidic single-mode laser using high-order Bragg grating and antiguiding segments*. Opt. Express, 2005. **13**: p. 344-351.
258. <http://omlc.ogi.edu/spectra/PhotochemCAD/html/rhodamine6G.html>.
259. Polynkin, P., A. Polynkin, N. Peyghambarian, and M. Mansuripur, *Evanescent field-based optical fiber sensing device for measuring the refractive index of liquids in microfluidic channels*. Opt. Lett., 2005. **30**: p. 1273-1275.
260. Sumetsky, M., Y. Dulashko, and M. Fishteyn, *Demonstration of a multi-turn microfiber coil resonator*, in *Optical Fiber Communication Conference*. 2007: Anaheim, CA. p. PDP46.
261. Li, Z., Z. Zhang, T. Emery, A. Scherer, and D. Psaltis, *Single mode optofluidic distributed feedback dye laser*. Opt. Express, 2006. **14**: p. 696-701.
262. Suter, J.D., W. Lee, D. J. Howard, E. Hoppmann, I. M. White, X. Fan, *Demonstration of the coupling of optofluidic ring resonator lasers with liquid waveguides*. Opt. Lett., 2010. **35**: p. 2997-2999.

263. Poon, A.W., X. Luo, H. Chen, G. E. Fernandes, and R. K. Chang, *Microspiral resonators for integrated photonics*. Opt. Photonics News, 2008. **19**: p. 48-53.
264. Galas, J.C., J. Torres, M. Belotti, Q. Kou, and Y. Chen, *Microfluidic tunable dye laser with integrated mixer and ring resonator*. Appl. Phys. Lett., 2005. **86**: p. 264101.
265. Manor, R., A. Datta, I. Ahmad, M. Holtz, S. Gangopadhyay, and T. Dallas, *Microfabrication and characterization of liquid core waveguide glass channels coated with teflon AF*. IEEE Sens. J., 2003. **3**: p. 687-692.
266. Memisevic, J., V. Korampally, S. Gangopadhyay, and S. A. Grant, *Characterization of a novel ultra-low refractive index material for biosensor application*. Sensor. Actuat. B-Chem., 2009. **141**: p. 227-232.

## VITA

Jonathan Daniel Suter was born September 11<sup>th</sup>, 1982 in Eugene, Oregon. He graduated from Sheldon High School in Eugene, Oregon in 2001 and was accepted into the Bioengineering program at Oregon State University. Jonathan graduated with a bachelor's degree, with honors, in August 2005 before joining the laboratory of Dr. Xudong Fan at the University of Missouri for his Ph.D. research.

He was awarded the NIH Biodetectives training grant in April 2007, which funded him for three years. He moved to the University of Michigan – Ann Arbor in December 2009 as a visiting researcher, where he continued to work for Dr. Fan until his graduation in December 2010.